Topological aspects of electromagnetic wave propagation in one-dimensional photonic crystal

By

Shailja Sharma

PHYS11201704023

National Institute of Science Education and Research, Bhubaneswar

A thesis submitted to the

Board of Studies in Physical Sciences

In partial fulfillment of requirements

for the Degree of

DOCTOR OF PHILOSOPHY

of

HOMI BHABHA NATIONAL INSTITUTE

December, 2022

Homi Bhaba National Institute

Recommendations of the Viva Voce Committee

As members of the Viva Voce Committee, we certify that we have read the dissertation prepared by Shailja Sharma entitled "Topological aspects of electromagnetic wave propagation in one-dimensional photonic crystal" and recommend that it may be accepted as fulfilling the thesis requirement for the award of Degree of Doctor of Philosophy.

Chairman - Prof. Bedangadas Mohanty   03/07/2023

Guide / Convener - Dr. Ritwick Das   03/07/23

Examiner - Prof. Sushil Mujumdar

Member 1 - Dr. Kartikeswar Senapati   02/07/2022

Member 2 - Dr. Pratap Kumar Sahoo   03/07/2023

Member 3 - Dr. Rajan Jha   03/7/23

Final approval and acceptance of this thesis is contingent upon the candidate's submission of the final copies of the thesis to HBNI.

I/We hereby certify that I/we have read this thesis prepared under my/our direction and recommend that it may be accepted as fulfilling the thesis requirement.

Date : 3/07/23

Place : JATNI

Signature

Co-guide (if any)

Signature

Guide

i

STATEMENT BY AUTHOR

This dissertation has been submitted in partial fulfillment of requirements for an advanced degree at Homi Bhabha National Institute (HBNI) and is deposited in the Library to be made available to borrowers under rules of the HBNI.

Brief quotations from this dissertation are allowable without special permission, provided that accurate acknowledgement of source is made. Requests for permission for extended quotation from or reproduction of this manuscript in whole or in part may be granted by the Competent Authority of HBNI when in his or her judgment the proposed use of the material is in the interests of scholarship. In all other instances, however, permission must be obtained from the author.
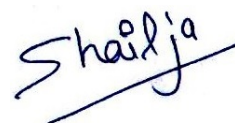
Shailja Sharma

Date: 21/12/2022

DECLARATION

I hereby declare that I am the sole author of this thesis in partial fulfillment of the requirements for a postgraduate degree from National Institute of Science Education and Research (NISER). I authorize NISER to lend this thesis to other institutions or individuals for the purpose of scholarly research.
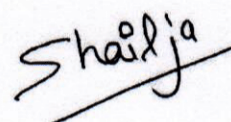
Shailja Sharma

Date: 21/12/2022

The thesis work reported in the thesis entitled "Topological aspects of electromagnetic wave propagation in one-dimensional photonic crystal" was carried out under my supervision, in the School of Physical Sciences at NISER, Bhubaneswar, India.
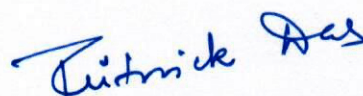
Signature of the thesis supervisor

School: PHYSICAL SCIENCES

Date: 03/07/2023

iii

List of Publications Arising from The Thesis

Journal

1. "Geometric representation of adiabatic distributed-Bragg-reflectors and broadening the photonic bandgap", S. Sharma, A. Mondal and R. Das, Opt. Express, **2021**, vol.29, pp.43303-43315.

2. "Infrared rainbow trapping via optical Tamm modes in an one-dimensional dielectric chirped photonic crystals", S. Sharma, A. Mondal and R. Das, Opt. Letters, **2021**, vol.46, pp.4566-4569.

3. "Geometric manifestation led optical beam shaping in one-dimensional photonic crystals", A. Mondal, S. Sharma and R. Das, JOSAB, **2022**, vol. 39, pp. 2429-2434.

4. "All-dielectric apodized photonic crystals: A non-dissipative pseudo-Hermitian system hosting multiple exceptional points", A. Mondal, S. Sharma and R. Das, Phys. Rev. A, **2023**, vol. 107, pp.053502.

Conferences

1. "Bandgap enhancement using adiabatic photonic crystal", S. Sharma, A. Mondal and R. Das, *XLIV OSI symposium on Frontier in optics and photonics*, IIT Delhi, **2021**.

2. "Rainbow trapping via excitation of optical Tamm modes in one-dimensional chirped photonic crystals", S. Sharma, A. Mondal, and R. Das, Student Conference on Optics and Photonics, PRL Ahmedabad, **2021**.

3. "Experimental observation of multiple Tamm-modes in 1D-chirped photonic crystal", S.Sharma and R.Das, Advanced Photonics Congress, Maastricht, Netherlands **2022**.

4. "Multiple optical Tamm modes in one-dimensional chirped photonic crystal", S. Sharma, A. Mondal, and R. Das, Frontiers in Optics + Laser Science 2022 (FIO, LS), Rochester, New York United States **2022**.

iv
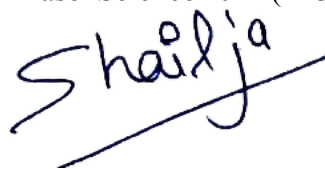
DEDICATION

I whole-heartedly dedicate this thesis to my beloved grand-parents, **Mrs. kamla Devi** and **Mr. Thakur Das Sharma**.

ACKNOWLEDGEMENTS

First of all, I would like to express my profound respect and sincere gratitude to my supervisor **Dr. Ritwick Das**. This thesis would not have been possible without his inspiring guidance, strong motivation, and priceless suggestions during my PhD tenure.

My deepest gratitude goes to my dear parents, and my family members whose countless sacrifices in life for their children allowed me to reach this point. Their unconditional love and support made me achieve many things that otherwise would be impossible.

I would also like to thank all my teachers and my friends who helped me directly or indirectly to come this far.

ABSTRACT

The adiabatic following has been widely employed for achieving near-complete population transfer in a 'two-level' quantum mechanical system. The theoretical basis could be adopted in any equivalent system exhibiting *special unitary (2)* or SU (2) symmetry. We have drawn an analogy of population transfer dynamics of a quantum two-level system with that of light propagation in classical "one-dimensional photonic crystals" (1D-PC), which are commonly known as distributed-Bragg-reflectors (DBRs). We show that there exists a one-to-one correspondence between the coupled wave equations of a 1D PC with the time-dependent Schrodinger equation of a quantum mechanical two-level system of spin-$1/2$ particles in a homogeneous magnetic field. In 1D-PCs, the incident beam state $|i\rangle$ and reflected beam state $|r\rangle$ are equivalent to the ground state $|g\rangle$ and excited state $|e\rangle$ of a two-level system. The propagation length (z) inside the 1D-PC is analogous to the time (t) coordinate while the coupling strength (κ) and the phase-mismatch (ΔK) between the interacting waves represent the parameters equivalent to Rabi frequency and detuning respectively. With this analogy, we employed the idea of rapid adiabatic passage (RAP) which is a well-known technique in a two-level atomic system for realizing 100% power transfer from the incident beam to the reflected beam for a broad spectral band. We designed and explored the propagation of light in a chirped photonic crystal (CPC) in which adiabatic constraints are completely satisfied and we found that the reflection spectrum of the configuration exhibits substantial broadening of the photonic bandgap (PBG) as well as suppression of sharp reflection peaks in the transmission band. When a thin plasmon-active metal is placed adjacent to the CPC configuration, the backscattered phase undergoes multiple π phase jumps which enable the excitation of multiple optical Tamm (OT) modes. All the OT modes are separated in the spectral domain and their strong confinement results in a reduced group velocity up to 0.17 times the velocity of light, thus allowing to trap a broad spectrum with lifetime $\geq 2.8ps$. In a separate study, we have focused on utilizing the topological features of the 1D-PC for carrying out beam wavefront shaping. The light transmitted through 1D-PC acquires a 'quantized' geometric phase (0 or π) which is also known as *Zak phase*. This gives rise to the structuring of optical beams over a broad spectral bandwidth via suitably designing the 1D-PC structure. In the last section of the

work, we explore a 1D PC-based optical system that obeys non-Hermitian dynamics and we show that each photonic bandgap of an all-dielectric 1D-PC hosts at least two exceptional points in its eigenvalue spectrum. By introducing suitable apodization in the PC, the geometry supports multiple exceptional points which distinguishes the PT-symmetric region from the region where PT-symmetry is broken. The interaction of eigenvalues around the exceptional points provides a deeper knowledge of the electromagnetic-wave propagation dynamics.

Contents

Summary

To summarize the work presented in this thesis, we have presented an approach to understanding the propagation characteristics of modes in a 1D photonic crystal using general techniques adopted in various systems that exhibit SU (2) dynamical symmetry. We have utilized the idea of adiabatic following, also known as rapid adiabatic passage (RAP), which is a well-established technique for realizing 100% population transfer in a two-level atomic system. We have shown that in suitably designed photonic crystal configurations the concept of adiabatic following leads to the enhancement of the photonic bandgap. We have also shown that the suitably designed photonic crystal configuration leads to the excitation of multiple optical Tamm-like resonances and these Tamm resonances offer a favorable platform for low-loss trapping of light with lifetimes up to 3ps. We have also presented a simple and flexible route to generate a structured light beam (or the first-order Hermite-Gaussian beam) by utilizing the topological features of the 1D-photonic crystal. Finally, we show the existence of multiple exceptional points in a suitably designed 1D-PC and develop an analytical framework for ascertaining the possibility of exciting topologically-protected optical edge modes.

List of Figures

xiii

List of Tables

Chapter 1

Introduction

1.1 Photonic crystals

Photonic Crystals (PCs) are periodic sub-wavelength architectures that are designed to influence the mobility of electromagnetic waves in a similar manner to how the periodic potential in a semiconductor crystal influences electron motion through defining allowed and forbidden electronic energy bands [1, 2]. PCs typically consist of periodic dielectric or periodic metallo-dielectric sub-wavelength architectures with materials exhibiting alternating low and high dielectric constants in one, two, or three dimensions so as to influence the propagation of electromagnetic (*em*) waves within the geometry. Due to this periodicity, the transmission of light in a certain frequency region is absolutely zero which is called a "Photonic Band Gap" (PBG). By introducing defects in these periodic structures, the PBG's continuity and PC periodicity is destroyed which enables the control and manipulation of light in the spectral domain, as well as spatial domain [1, 2]. These defects may be point defects, line defects, or both. Light is localized in the PBG region due to the presence of these defects, which facilitates the creation of a variety of PC-based optical devices.

James Clark Maxwell in 1864, established a close relationship between optics and electromagnetism by summarizing the theory of *em* waves in a set of differential equations. He explained the mechanism of wave propagation when it traverses through the medium [3]. Later, in 1887, Lord Rayleigh carried out the first analysis of *em* field propagation in a periodic system extending to infinity in one direction and derived a general one-dimensional wave equation in a periodic media[4]. He observed that the plane wave propagating through the structure is considered as the sum of multiple reflections and transmissions that occur

1

at each interface. Such geometries tend to exhibit a range of frequencies that is prohibited to propagate inside the periodic arrangement. The propagation of *em* radiation in periodic structures exhibits many interesting and useful phenomena such as the diffraction of X-rays in crystals, the photonic bandgap of light propagating through periodic layered media, and the light scattering by fiber Bragg gratings. These phenomena are useful in many optoelectronic devices including diffraction gratings, high-reflectance Bragg mirrors, vertical cavity surface emitting lasers, distributed feedback lasers, distributed Bragg reflection lasers, fiber Bragg gratings, and acousto-optic filters.

A century later, in 1987, a more general form of periodic geometries or PCs were introduced independently by two researchers E. Yablonovitch and S. John. Yablonovitch [2] proposed the possibility of prohibiting spontaneous emission of *em* radiation throughout a broad spectrum using a three-dimensional periodic dielectric arrangement and this lattice has regions of forbidden energy states for photons showing photonic band gaps. S. John [1] proposed the concept of strong localization of photons in disordered dielectric superlattices and suggested that the defects in a lattice trap *em* radiations where certain energy states for photons were forbidden. These two pioneering works are considered as the origin of the "*photonic crystals* or *photonic band gap materials*". Over the last four decades, photonic crystals have evolved as the backbone of many technological advancements which essentially hinge upon manipulating the spatial and spectral characteristics of light beam [5]. Nowadays, PCs have sparked a lot of interest and research due to their revolutionizing applications in modern photonic engineering, such as optical communication and optoelectronics. PCs have the ability to control and manipulate light due to this they have been identified as the most promising candidates for the realization of compact all-optical communication and computing systems [6].

The propagation characteristics of em waves in a periodically stratified dielectric medium are strikingly similar to the features exhibited by the matter waves in crystalline solids

[7, 8]. In crystals, the periodic *Coulomb-potential* leads to the formation of continuous energy bands separated by forbidden energy spectrum, also known as bandgaps. In a similar fashion, the periodic variation of dielectric constant in PCs with the periodicity of the order of the wavelength of light led to the formation of transmission (or pass) bands which are separated by forbidden spectral bands known as photonic bandgaps (PBGs) [9, 10]. PCs could be thought of as semiconductors for the light beam. It is made up of a dielectric medium that is arranged in a pattern similar to a periodic array of positive potential scatterers. In a periodic potential of crystals, the energy-momentum relation for electrons modifies, especially they are discernible at the Brillouin zone boundaries. In PCs, the PBG or the forbidden band is centered around the frequency that fulfills the Bragg condition $2\Lambda sin(\theta) = n\lambda$. Here, Λ denotes the period of the index variation in space, θ is the angle of incidence, n is the order of the Bragg reflection and λ denotes the operating wavelength. PCs are classified primarily into three categories: one-dimensional (1D), two-dimensional (2D), and three-dimensional (3D) photonic crystals, depending upon whether the periodicity is in one, two, or three dimensions. Accordingly, the PBGs are direction dependent, meaning that light propagation can only be modulated in the directions of periodically varying dielectric constant. The schematic illustrations of 1D PC, 2D PC and 3D PC are shown in Fig.1.1

1D PC consists of periodic modulation of the refractive index in one direction only, while the structure is homogeneous in the other two directions. Such photonic structures have been fabricated by a variety of methods, such as chemical vapor deposition, magnetron sputtering, etc [11, 12]. For electrically pumped vertical cavity surface emitting lasers (VCSELs), where high mobility defect-free semiconductors ie. GaAs and AlGaAs 1D PCs are required, molecular beam epitaxy method is used [13]. In addition, pure silicon 1D multilayer PCs can be readily obtained via the electrochemical etching of crystalline silicon[14].

For any value of refractive index contrast *i.e.*, the difference between the dielectric constant of the materials, PBG appears in the direction of periodicity. The width of the PBG is
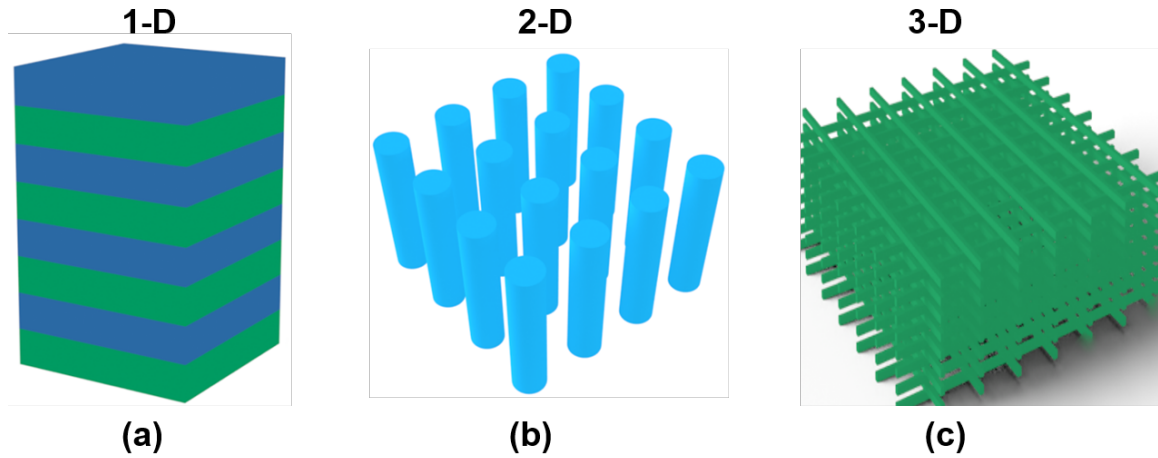
Figure 1.1: Schematic illustrations of photonic crystals (a) 1-D (b) 2-D (c) 3-D

primarily dictated by the refractive index contrast of the constituting materials and the location in the spectral band is governed by the thickness of constituting layers. 1D PCs can act as a *mirror* for light having a frequency within the PBG and are also known as *distributed-Bragg-reflectors (DBRs)* due to their analogy with the Bragg diffraction of X-rays from various atomic planes. This type of PC can localize light modes in the presence of defects in the structure. A defect in a 1D PC can be simply introduced by giving one of the layers a slightly different refractive index or width than the others. The defect mode is then localized in one direction but extends into the other two. These concepts are commonly employed in dielectric mirrors [15, 16], optical filters [17, 18, 19], low-loss waveguides [20], and lasers [21, 22, 23, 24] and also provide an efficient sensing platform for plasmonic-based interactions [25, 26, 27]. Furthermore, such structures are widely used as anti-reflective coatings, which greatly reduce surface reflectance and are used to improve the quality of lenses, prisms, and other optical components [28]. Wave guiding configurations based on the phenomena of Bragg reflection have been employed as polarization selection devices in miniaturized optical sources [29, 30] and also, projected as possible hosts for future optical particle accelerators driven by extremely high-power lasers [31]. On the other hand,

4

the possibility of field confinement and therefore, reducing the *em* interaction volume to sub-wavelength scale has led to the formation of stable spatial-solitons in nonlinear Bragg-reflection-waveguides [32]. Recently, the bulk modes of Bragg-reflection waveguides or optical surface states in DBR have been found to be promising candidates for optical parametric processes and higher harmonic generation [33, 34, 35, 36]. By introducing chirp in a periodic DBR system, broadband distributed-feedback-lasers have been experimentally realized and it finds widespread applicability in modern generation laser technology [37, 38, 39]. Additionally, the chirped-DBR configurations have been explored for devising group-velocity-compensating elements in broadband frequency conversion processes [40]. Optimally-designed chirped-DBR architectures have also been explored from the perspective of the generation of slow-light and realizing light-trapping schemes [41, 42, 43].

2D PC is periodic in two directions and homogeneous along the third direction as shown in Fig.1.1(b). For 2D PCs the PBG appears in the plane of periodicity, inside this gap, no *em* states are permitted and the light is reflected [9]. Light propagating in the plane of periodicity can be decoupled into TE modes (transverse electric, assuming the electric field to be in the plane of periodicity) and TM modes (transverse magnetic, assuming the magnetic field to be in the plane of periodicity). Both TE and TM modes have very different dispersion. We could make the photonic bandgaps overlap by adjusting the lattice geometry, resulting in a "complete band gap" *i.e.* a frequency region where *em* wave propagation is completely prohibited for both TE and TM polarization. Light modes with frequencies within the PBG can be localized by introducing point defects in the structure, but in this case, one can localize light modes in two dimensions, rather than just in one dimension. 2D PCs can also be employed to guide light from one location to another by adding line defects in the structure [44, 45]. Due to the widespread use of very advanced lithographic techniques that have been refined over many years in the microelectronics sector, 2D PCs have advanced the most among all known PC systems. Due to its manufacturing process,

2D PCs are perfectly suited to be coupled with advanced electronic integrated circuitry, enabling the creation of hybrid systems with simultaneous optical and electrical operation [46].

3D PC is a full optical analog of a conventional crystal, which has periodicity along three different axes as shown in Fig.1.1(c). A natural example of 3D PC is a stone known as opal. This stone possesses unique optical properties of showing different colors from different angles by virtue of the opal's distinctive microstructure. A PBG appears in all directions when conditions of sufficiently high dielectric contrast and suitable periodicity are met. Such 3D PBGs can reflect light incident from any arbitrary direction for all the polarizations resulting in the formation of a complete photonic bandgap. Just as in 2D PC, one can localize light at a defect or at a surface but these defect modes are localized in the plane of periodicity and extended in the third direction. 3D PC has the additional capability to localize light to a single point in the crystal. It is trapped in all *three* dimensions. The first realization of a complete PBG crystal operating at microwave frequencies, as confirmed by angle-resolved reflectivity and transmissivity measurements were reported by Yablonovitch [47]. There are various examples of 3D PCs with complete band gaps such as a diamond lattice of air holes, a drilled dielectric known as *Yablonovite*, and a *woodpile* stack of orthogonal dielectric columns [9]. 3D PCs are mainly fabricated via Direct laser writing (DLW) [48] and interference lithography (IL) technique[49]. At present IL certainly stands as the preferred method for preparing periodic and quasi-periodic patterns over large areas. In IL, the interference of four coherent laser beams creates a standing wave pattern in three dimensions, which in turn can be recorded in a photoresist. The spatial period of the grating can be as low as half the wavelength of the interfering light, allowing for structures of the order of 100 nm from UV wavelengths; features as small as 30-40 nm are also possible with a deep ultraviolet ArF laser [50]. The former method, DLW makes use of multiphoton polymerization in a photoresist that is transparent to the wavelength of the laser employed and has emerged

6

as a technique for the rapid, cheap, and versatile fabrication of photonic nanostructures. By scanning and properly modulating the laser, polymerization occurs at the focal spot of the laser and can be controlled to create an arbitrary 3D periodic pattern. Additionally, 3D PCs have also been generated by deep X-ray lithography technique and this method has been successful at replicating the *Yablonovite* structure [51].

1.2   Dissertation organization

The focus of the work presented in this thesis is the theoretical study of the peculiarities of *em* wave propagation in a periodic dielectric medium, mainly focusing on the one-dimensional photonic crystals. The whole work in this thesis has been organized into seven chapters. In Chapter 1, we provide a brief introduction to the concept and principle behind photonic crystals as well as the applications based on photonic crystals. In chapter 2, we discuss the general properties of wave propagation in periodic media which is followed by an explanation of the transfer matrix method (TMM), a broadly used method to study wave propagation in periodic stratified media. In the second part, the coupled-mode formalism is described with an aim to estimate the transmission and reflection spectrum for a one-dimensional photonic crystal (PC). In chapter 3, we present an adiabatic mode-coupling scheme between the forward and backward propagating modes of a photonic crystal and present a chirped photonic crystal configuration in which the adiabatic constraints are satisfied by virtue of optimally chirping the PC. Then, we draw an equivalence of the two-level atomic system and the spin-$1/2$ dynamics of a particle with that of light propagation in a one-dimensional photonic crystal. Further, we discuss that this chirped photonic crystal could be employed for trapping a broadband spectrum through the excitation of optical Tamm modes in chapter 4. In chapter 5, we discuss the possibility of structuring optical beams via tailoring the geometric phase of the photonic crystal. In chapter 6, we explore

the possibility of creating asymmetric losses without adding gain in the system and study a non-Hermitian system that led to the existence of multiple exceptional points. The last chapter will highlight the overall conclusions and future research directions which could be derived from this thesis.

References

[1] Sajeev John. Strong localization of photons in certain disordered dielectric superlattices. *Phys. Rev. Lett.*, 58:2486–2489, Jun 1987.

[2] Eli Yablonovitch. Inhibited spontaneous emission in solid-state physics and electronics. *Phys. Rev. Lett.*, 58:2059–2062, May 1987.

[3] J. C. Maxwell. Viii. a dynamical theory of the electromagnetic field. *Philos.Tran. Royel Society of London*, 155:459–512, 1865.

[4] Lord Rayleigh Sec. R. S. Xvii. on the maintenance of vibrations by forces of double frequency, and on the propagation of waves through a medium endowed with a periodic structure. *The London, Edinburgh, and Dublin Philosophical Magazine and Journal of Science*, 24(147):145–159, 1887.

[5] Amnon Yariv and Pochi Yeh. *Photonics Optical Electronics in Modern Communications*. Oxford University, 6th edition, 2007.

[6] Athira Jayaprakash, Joshua Nigel, and Ishu Sharma. *A Review on the Materials and Applications of Nanophotonics*, pages 116–140. 01 2023.

[7] Eli Yablonovitch. Inhibited spontaneous emission in solid-state physics and electronics. *Phys. Rev. Lett.*, 58:2059–2062, May 1987.

[8] Riccardo Sapienza, Paola Costantino, Diederik Wiersma, Mher Ghulinyan, Claudio Oton, and Lorenzo Pavesi. Optical analogue of electronic Bloch oscillations. *Phys. Rev. Lett.*, 91:263902, 01 2004.

[9] John D Joannopoulos, Steven G Johnson, Joshua N Winn, and Robert D Meade. *Photonic Crystals Molding the Flow of Light*. Princeton University, 2nd edition, 2008.

[10] Pochi Yeh, Amnon Yariv, and Chi-Shain Hong. Electromagnetic propagation in periodic stratified media. i. general theory∗. *J. Opt. Soc. Am.*, 67(4):423–438, Apr 1977.

[11] H. Angus Macleod. Thin-film optical filters. 1969.

[12] V Gottschalch, R Schmidt, B Rheinländer, D Pudis, S Hardt, J Kvietkova, G Wagner, and R Franzheld. Plasma-enhanced chemical vapor deposition of siox/sinx bragg reflectors. *Thin Solid Films*, 416(1):224–232, 2002.

[13] Cheng Zhang, Rami ElAfandy, and Jung Han. Distributed bragg reflectors for gan-based vertical-cavity surface-emitting lasers. *Applied Sciences*, 9(8), 2019.

[14] Herman Lopez and Philippe Fauchet. Erbium emission from porous silicon one-dimensional photonic band gap structures. *Applied Physics Letters*, 77:3704–3706, 12 2000.

[15] M. Deopura, C. K. Ullal, B. Temelkuran, and Y. Fink. Dielectric omnidirectional visible reflector. *Opt. Lett.*, 26(15):1197–1199, Aug 2001.

[16] S. Jena, R.B. Tokas, S. Thakur, and D.V. Udupa. Tunable mirrors and filters in 1d photonic crystals containing polymers. *Physica E: Low-dimensional Systems and Nanostructures*, 114:113627, 2019.

[17] Lina Maigyte and Kestutis Staliunas. Spatial filtering with photonic crystals. *Appl. Phys. Rev.*, 2:011102, 02 2015.

[18] Kimura Mitsuteru, Okahara Kazuaki, and Toshihiko Miyamoto. Tunable multilayer-film distributed-Bragg-reflector filter. *J. Appl. Phys.*, 50:1222, 03 1979.

[19] Kun-yuan Xu, Xiguang Zheng, Cai-lian Li, and Wei-long She. Design of omnidirectional and multiple channeled filters using one-dimensional photonic crystals containing a defect layer with a negative refractive index. *Phys. Rev. E*, 71:066604, Jun 2005.

[20] Attila Mekis, J. C. Chen, I. Kurland, Shanhui Fan, Pierre R. Villeneuve, and J. D. Joannopoulos. High transmission through sharp bends in photonic crystal waveguides. *Phys. Rev. Lett.*, 77:3787–3790, Oct 1996.

[21] Byeong-Hyeon Ahn, Ju-Hyung Kang, Myung-Ki Kim, Jung-Hwan Song, Bumki Min, Ki-Soo Kim, and Yong-Hee Lee. One-dimensional parabolic-beam photonic crystal laser. *Opt. Express*, 18(6):5654–5660, Mar 2010.

[22] Alexander Palatnik, Markas Sudzius, Stefan Meister, and Karl Leo. One-dimensional planar topological laser. *Nanophotonics*, 10(9):2459–2465, 2021.

[23] H. Ishii, Y. Tohmori, Y. Yoshikuni, T. Tamamura, and Y. Kondo. Multiple-phase shift super structure grating dbr lasers for broad wavelength tuning. *IEEE Photonics Technology Letters*, 5(6):613–615, 1993.

[24] Clementine Symonds, Guillaume Lheureux, Jean Paul Hugonin, Jean Jacques Greffet, Julien Laverdant, Giovanni Brucoli, Aristide Lemaître, P. Senellart, and Joel Bellessa. Confined tamm plasmon lasers. *Nano letters*, 13, 06 2013.

[25] M. Kaliteevski, I. Iorsh, S. Brand, R. A. Abram, J. M. Chamberlain, A. V. Kavokin, and I. A. Shelykh. Tamm plasmon-polaritons: Possible electromagnetic states at the interface of a metal and a dielectric Bragg mirror. *Phys. Rev. B*, 76:165415, Oct 2007.

[26] Mukesh Kumar Shukla and Ritwick Das. Tamm-plasmon polaritons in one-dimensional photonic quasi-crystals. *Opt. Lett.*, 43(3):362–365, Feb 2018.

[27] Yun Shen, Jiwu Fu, and Guoping Yu. Rainbow trapping in one-dimensional chirped photonic crystals composed of alternating dielectric slabs. *Phys. Lett. A*, 43:3801 – 3803, 10 2011.

[28] H. Deng, Xianyue Dong, Huanhuan Gao, Xiaodong Yuan, Wanguo Zheng, and Xiaotao Zu. Standing wave field distribution in graded-index antireflection coatings. *Applied Sciences*, 8:65, 01 2018.

[29] Brian West and Amr Helmy. Properties of the quarter-wave Bragg reflection waveguide: Theory. *J. Opt. Soc. Am. B*, 23:1207–1220, 06 2006.

[30] Eli Simova and Ilya Golub. Polarization splitter/combiner in high index contrast Bragg reflector waveguides. *Opt. Express*, 11:3425–3430, 01 2004.

[31] Amit Mizrahi and Levi Schächter. Optical Bragg accelerators. *Phys. Rev. E*, 70:016505, Jul 2004.

[32] C. Wächter, F. Lederer, L. Leine, U. Trutschel, and M. Mann. Nonlinear Bragg reflection waveguide. *J. Appl. Phys.*, 71:3688–3692, 1992.

[33] Ivan V. Iorsh, Pavel A. Belov, Alexander A. Zharov, Ilya V. Shadrivov, and Yuri S. Kivshar. Nonlinear Tamm states in nanostructured plasmonic metamaterials. *Phys. Rev. A*, 86:023819, Aug 2012.

[34] Boris Afinogenov, A. Popkova, V. Bessonov, B. Lukyanchuk, and Andrey Fedyanin. Phase matching with Tamm plasmons for enhanced second- and third-harmonic generation. *Phys. Rev. B*, 97:115438, 03 2018.

[35] Cornelia Denz, Sergej Flach, and Yuri S Kivshar. *Nonlinearities in Periodic Structures and Metamaterials*. Springer, 2008.

[36] B. I. Afinogenov, V. O. Bessonov, and A. A. Fedyanin. Second-harmonic generation enhancement in the presence of tamm plasmon-polaritons. *Opt. Lett.*, 39(24):6895–6898, Dec 2014.

[37] G.P. Agrawal and A.H. Bobeck. Modeling of distributed feedback semiconductor lasers with axially-varying parameters. *IEEE Journal of Quantum Electronics*, 24(12):2407–2414, 1988.

[38] Makoto Yamada and Kyohei Sakuda. Analysis of almost-periodic distributed feedback slab waveguides via a fundamental matrix approach. *Appl. Opt.*, 26(16):3474–3478, Aug 1987.

[39] Herwig Kogelnik. Filter response of nonuniform almost-periodic structures. *The Bell System Technical Journal*, 55:109–126, 1976.

[40] Chao Xu and Dayan Ban. Design of chirped distributed Bragg reflector for octave-spanning frequency group velocity dispersion compensation in terahertz quantum cascade laser. *Opt. Express*, 24(12):13500–13510, Jun 2016.

[41] Peyman Ghaderian and Amir Habibzadeh-Sharif. Rainbow trapping and releasing in graded Bragg grating graphene plasmonic waveguide. *Optics Express*, 29:3996–4009, 01 2021.

[42] Yun Shen, Hailin Liu, Jiwu Fu, and Guoping Yu. Double rainbow trapping of light in one-dimensional chirped metallic–dielectric photonic crystals. *J. Opt. Soc. Am. B*, 28(10):2444–2447, Oct 2011.

[43] Zhixia Xu, Jun Shi, Robert J. Davis, Xiaoxing Yin, and Daniel F. Sievenpiper. Rainbow trapping with long oscillation lifetimes in gradient magnetoinductive metasurfaces. *Phys. Rev. Applied*, 12:024043, Aug 2019.

[44] Enaul haq Shaik and Nakkeeran Rangaswamy. Design of photonic crystal-based all-optical and gate using t-shaped waveguide. *Journal of Modern Optics*, 63(10):941–949, 2016.

[45] T Sridarshini and S Indira Gandhi. Photonic band structure of 2d photonic crystals—a comparative study. *Laser Physics*, 30(2):026205, dec 2019.

[46] Sajeev John and Marian Florescu. Photonic bandgap materials: Towards an all-optical micro-transistor. *Journal of Optics A: Pure and Applied Optics*, 3, 12 2001.

[47] E. Yablonovitch, T. J. Gmitter, and K. M. Leung. Photonic band structure: The face-centered-cubic case employing nonspherical atoms. *Phys. Rev. Lett.*, 67:2295–2298, Oct 1991.

[48] M. Deubel, Georg von Freymann, M. Wegener, S. Peirera, K. Busch, and Costas Soukoulis. Direct laser writing of three-dimensional photonic crystal templates for photonic bandgaps at telecommunication wavelenghts. 05 2004.

[49] D.N. Sharp, A.J. Turberfield, M. Campbell, and R.G. Denning. Photonic crystals for the visible spectrum by holographic lithography. In *Conference Digest. 2000 Conference on Lasers and Electro-Optics Europe (Cat. No.00TH8505)*, pages 1 pp.–, 2000.

[50] Cefe Lopez. Materials aspects of photonic crystals. *Advanced Materials*, 15:1679 – 1704, 10 2003.

[51] C. Cuisin, A. Chelnokov, J.-M. Lourtioz, D. Decanini, and Y. Chen. Fabrication of three-dimensional photonic structures with submicrometer resolution by x-ray lithog-

raphy. *Journal of Vacuum Science & Technology B: Microelectronics and Nanometer Structures Processing, Measurement, and Phenomena*, 18(6):3505–3509, 11 2000.

Chapter 2

Electromagnetic wave propagation in pe-riodic media

In this chapter, we will discuss the *em* wave propagation in a one - dimensional periodic medium. Wave propagation in periodic layered media has been studied by many groups. The exact solution of the wave equation in periodic media can be obtained using the transfer matrix method, a widely used method to study wave propagation in periodically stratified media. However, there are a few geometries for which only approximate solutions of Maxwell's equations can be obtained. With this context in sight, the second part of the chapter discusses the coupled-mode formalism for estimating the transmission, reflection spectrum, and band structure for a one-dimensional photonic crystal.

2.1   The transfer matrix method

The Transfer Matrix Method (TMM) is a well-known method for ascertaining the bandstructure and propagation characteristics of electromagnetic waves in one-dimensional periodic structures [1, 2]. Using layer-by-layer estimation of propagation, it could handle PBG materials of finite thickness. In general, the PC geometries with defects could also be handled using this recipe. The simplest periodically-stratified medium is one that consists of alternating layers of high and low refractive index dielectric materials with an index of refraction n_1 and n_2 respectively. The dielectric layers having thicknesses d_1 and d_2 respectively are arranged periodically along the z-direction with lattice period $\Lambda = d_1 + d_2$ and the structure is homogeneous along the x and y direction as illustrated in Fig.2.1. Also, we assume that the materials are isotropic and non-magnetic. The refractive index profile of the PC is
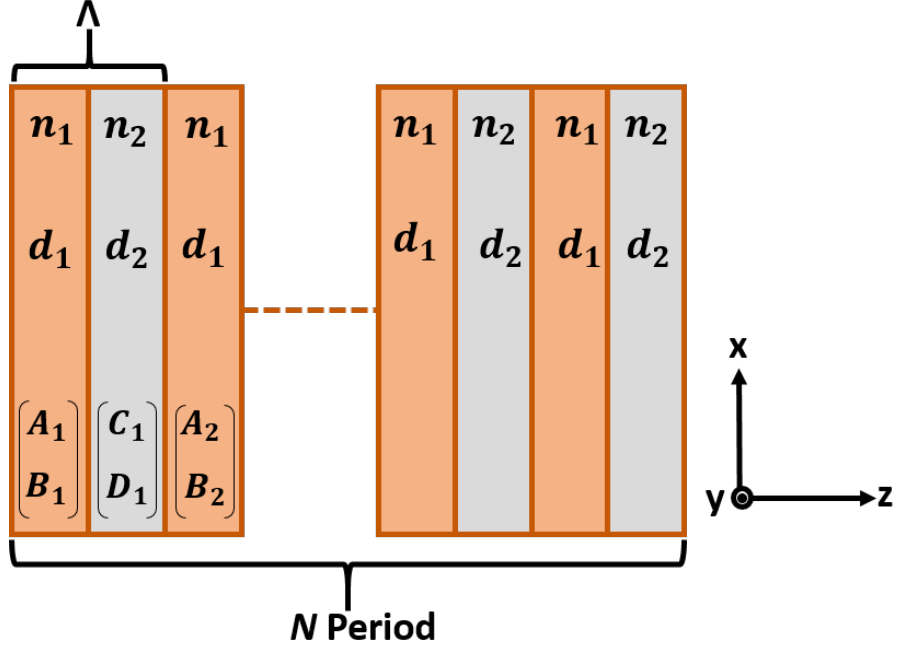
Figure 2.1: Schematic design of 1D multilayer periodic structure

described through [3]

$$n(z) = \begin{cases} n_1, 0 < z < d_1 \\ n_2, d_1 < z < \Lambda \end{cases} \tag{2.1}$$

with

$$n(z) = n(z + \Lambda) \tag{2.2}$$

The propagation of *em* wave in a charge-free and current-free medium is described by Maxwell's equations,

$$\vec{\nabla} \cdot \vec{E} = 0 \tag{2.3}$$

$$\vec{\nabla} \cdot \vec{H} = 0 \tag{2.4}$$

$$\vec{\nabla} \times \vec{E} = -\mu_0 \frac{\partial \vec{H}}{\partial t} \tag{2.5}$$

$$\vec{\nabla} \times \vec{H} = \epsilon \frac{\partial \vec{E}}{\partial t} \tag{2.6}$$

The wave equation for E could be obtained by taking the cross product of Eq.2.5 and using Eq.2.6,

$$\vec{\nabla} \times (\vec{\nabla} \times \vec{E}) = -\mu_0 \epsilon \frac{\partial^2 \vec{E}}{\partial t^2} \tag{2.7}$$

The first term in the above equation could be expanded using vector triple product identity as:

$$\vec{\nabla} \times (\vec{\nabla} \times \vec{E}) = \vec{\nabla}(\vec{\nabla} \cdot \vec{E}) - \vec{\nabla}^2 \vec{E} \tag{2.8}$$

For a charge-free isotropic media, the first term on the right-hand side of Equation2.8 is zero. Thus wave equation for electric field $\vec{E}$ becomes,

$$\nabla^2 \vec{E} - \mu_0 \epsilon \frac{\partial^2 \vec{E}}{\partial t^2} = 0 \tag{2.9}$$

here, $\epsilon = \epsilon_0 \epsilon_r$ and $c^2 = \frac{1}{\epsilon_0 \mu_0}$.

Similarly, the equation for magnetic field $\vec{H}$ can be written as

$$\nabla^2 \vec{H} - \mu_0 \epsilon \frac{\partial^2 \vec{H}}{\partial t^2} = 0 \tag{2.10}$$

Equations2.9 and 2.10 are the standard electromagnetic wave equations. They satisfy the well-known plane wave solution for $\vec{E}$ and $\vec{H}$ *i.e.*

$\vec{E}(\vec{r}, t) = E_0 e^{i(\omega t - \vec{k} \cdot \vec{r})}$ and $\vec{H}(\vec{r}, t) = H_0 e^{i(\omega t - \vec{k} \cdot \vec{r})}$

where, $\vec{k}$ defines the direction of propagation and ω is the angular frequency of the incident light. For TE polarization, the wave equation for $\vec{E}$ in one-dimensional propagation (along the z-direction) could be written as

$$\frac{d^2}{dz^2} E(z) + \frac{\omega^2}{c^2} \epsilon(z) E(z) = 0 \tag{2.11}$$

Similarly, for TM polarization, the wave equation for $\vec{H}$ propagating in a one-dimensional case could be written as

$$\frac{d^2}{dz^2} H(z) + \frac{\omega^2}{c^2} \epsilon(z) H(z) = 0 \tag{2.12}$$

For a 1D-periodic medium, we assume that the refractive index (or the dielectric constant) varies only along the propagation (z) direction as shown in Fig.2.1. The electric field distribution $E(z)$ within each homogeneous layer could be expressed as a sum of an incident plane wave and a reflected plane wave. The complex amplitudes of these two waves constitute the component of a column vector. The electric field in the 1st unit cell could be written as [3]

$$E(z) = \begin{cases} A_1 e^{-ik_{1z}z} + B_1 e^{ik_{1z}z}, 0 < z < d_1 \\ C_1 e^{-ik_{2z}(z-d_1)} + D_1 e^{ik_{2z}(z-d_1)}, d_1 < z < \Lambda; \end{cases} \tag{2.13}$$

where k_{1z} and k_{2z} are the propagation constants in the z-direction in layers of refractive index n_1 and n_2 respectively and they are defined as

$$\begin{aligned} k_{1z} &= \frac{n_1 \omega}{c} cos\theta_1 \\ k_{2z} &= \frac{n_2 \omega}{c} cos\theta_2 \end{aligned} \tag{2.14}$$

where θ_1 and θ_2 are the angle of incidence in layers with refractive indices n_1 and n_2 respectively. By imposing the continuity condition of E_x and H_y (with $H_y \propto \partial E_x / \partial z$) at interfaces $z = d_1$ and $z = d_2$, we obtain

$$A_1 e^{-ik_{1z}d_1} + B_1 e^{ik_{1z}d_1} = C_1 + D_1$$

$$-ik_{1z}A_1 e^{-ik_{1z}d_1} + ik_{1z}B_1 e^{ik_{1z}d_1} = -ik_{2z}C_1 + ik_{2z}D_1$$

$$C_1 e^{-ik_{2z}d_2} + D_1 e^{ik_{2z}d_2} = A_2 + B_2 \tag{2.15}$$

$$-ik_{2z}C_1 e^{-ik_{2z}d_2} + ik_{2z}D_1 e^{ik_{2z}d_2} = -ik_{1z}A_2 + ik_{1z}B_2$$

These four equations could be in matrix form as

$$\begin{pmatrix} e^{-ik_{1z}d_1} & e^{ik_{1z}d_1} \\ -ik_{1z}e^{-ik_{1z}d_1} & ik_{1z}e^{ik_{1z}d_1} \end{pmatrix} \begin{pmatrix} A_1 \\ B_1 \end{pmatrix} = \begin{pmatrix} 1 & 1 \\ -ik_{2z} & ik_{2z} \end{pmatrix} \begin{pmatrix} C_1 \\ D_1 \end{pmatrix} \tag{2.16}$$

$$\begin{pmatrix} e^{-ik_{2z}d_2} & e^{ik_{2z}d_2} \\ -ik_{2z}e^{-ik_{2z}d_2} & ik_{2z}e^{ik_{2z}d_2} \end{pmatrix} \begin{pmatrix} C_1 \\ D_1 \end{pmatrix} = \begin{pmatrix} 1 & 1 \\ -ik_{1z} & ik_{1z} \end{pmatrix} \begin{pmatrix} A_2 \\ B_2 \end{pmatrix} \tag{2.17}$$

In this matrix representation, the complex amplitudes of the two plane waves in each layer constitute the components of a two-component column vector. The electric field in each layer of the unit cell could be represented by a column vector. These column vectors are not independent of each other. They are related through the continuity conditions at the interfaces. As a result, only one column vector could be chosen independently. By eliminating this column vector given by

$$\begin{pmatrix} C_1 \\ D_1 \end{pmatrix}$$

The matrix equation is obtained as

$$\begin{pmatrix} A_1 \\ B_1 \end{pmatrix} = \begin{pmatrix} M_{11} & M_{12} \\ M_{21} & M_{22} \end{pmatrix} \begin{pmatrix} A_2 \\ B_2 \end{pmatrix} = \bar{\bar{M}} \begin{pmatrix} A_2 \\ B_2 \end{pmatrix} \tag{2.18}$$

The matrix $\bar{\bar{M}}$ in this equation is called a *unit cell translation matrix* that relates the complex amplitudes of the incident plane wave A_1 and the reflected plane wave B_1 in one layer of the unit cell to those of the equivalent layer in the next unit cell. As this matrix relates the field amplitudes of two equivalent layers with the same index of refraction, it is unimodular, *i.e.*

$$\begin{vmatrix} M_{11} & M_{12} \\ M_{21} & M_{22} \end{vmatrix} = M_{11}M_{22} - M_{12}M_{21} = 1 \tag{2.19}$$

The form of matrix elements is given by

$$M_{11} = e^{ik_{1z}d_1}\left[cosk_{2z}d_2 + \frac{1}{2}i\left(\gamma + \frac{1}{\gamma} \right)sink_{2z}d_2 \right],$$

$$M_{12} = e^{-ik_{1z}d_1}\left[\frac{1}{2}i\left(\frac{1}{\gamma} - \gamma \right)sink_{2z}d_2 \right],$$

$$M_{21} = e^{ik_{1z}d_1}\left[-\frac{1}{2}i\left(\frac{1}{\gamma} - \gamma \right)sink_{2z}d_2 \right], \tag{2.20}$$

$$M_{22} = e^{-ik_{1z}d_1}\left[cosk_{2z}d_2 - \frac{1}{2}i\left(\gamma + \frac{1}{\gamma} \right)sink_{2z}d_2 \right].$$

where γ is a parameter which is defined as $\gamma = \frac{k_{1z}}{k_{2z}}$ for TE mode and $\gamma = \frac{k_{1z} \times n_2^2}{k_{2z} \times n_1^2}$ for TM mode.

For N unit cells, the column vector of equivalent layers is related to that of the zeroth unit cell by

$$\begin{pmatrix} A_0 \\ B_0 \end{pmatrix} = \begin{pmatrix} M_{11} & M_{12} \\ M_{21} & M_{22} \end{pmatrix}^N \begin{pmatrix} A_N \\ B_N \end{pmatrix} \tag{2.21}$$

The above equation could be inverted to obtain

$$\begin{pmatrix} A_N \\ B_N \end{pmatrix} = \begin{pmatrix} M_{11} & M_{12} \\ M_{21} & M_{22} \end{pmatrix}^{-N} \begin{pmatrix} A_0 \\ B_0 \end{pmatrix} = \begin{pmatrix} M_{22} & -M_{12} \\ -M_{21} & M_{11} \end{pmatrix}^N \begin{pmatrix} A_0 \\ B_0 \end{pmatrix} \tag{2.22}$$

The matrix in this equation 2.22 is a translation or transfer matrix, for a N-period multilayer structure, which relates the complex amplitudes of the plane waves in layer 1 of the zeroth unit cell to those of the equivalent layer in the last unit cell of the PC.

2.1.1 Photonic bandstructure

The propagation of *em* waves in periodic media is similar to the motion of electrons in crystalline solids. Hence, some of the physical concepts such as Bloch waves, Brillouin zones, and energy bands used in solid-state physics could also be employed in this context. A 1D periodic layered medium is equivalent to a 1D crystal, which is invariant under lattice translations. If the translation operator T is defined as $Tz = z + m\Lambda$, where m is an integer, then the field in the layered medium obeys the relation

$$TE(z) = E(T^{-1}z) = E(z - m\Lambda) \tag{2.23}$$

According to the Bloch theorem, the electric field of the eigenwave in the periodic medium is of the form

$$\vec{E}(\vec{r}, t) = \vec{E}_K(z)e^{-iKz}e^{i(\omega t - k_y y)} \tag{2.24}$$

where, $\vec{E}_K(z)$ is a periodic function with periodicity Λ *i.e.*

$$\vec{E}_K(z) = \vec{E}_K(z + \Lambda) \tag{2.25}$$

The subscript K indicates that the function $\vec{E}_K(z)$ depends on K. The constant K is known as the *Bloch wavenumber* and needs to be determined for ascertaining the propagation characteristics within the PC. In terms of column vector representation, Eq. 2.25 for the Bloch wave is simply given by

$$\begin{pmatrix} A_N \\ B_N \end{pmatrix} = e^{-iK\Lambda} \begin{pmatrix} A_{n-1} \\ B_{n-1} \end{pmatrix} \tag{2.26}$$

By using equations 2.18 and 2.26, the column vector depicting the Bloch eigenwave satisfies the following eigenvalue equation

$$\begin{pmatrix} M_{11} & M_{12} \\ M_{21} & M_{22} \end{pmatrix} \begin{pmatrix} A_N \\ B_N \end{pmatrix} = e^{iK\Lambda} \begin{pmatrix} A_n \\ B_n \end{pmatrix} \tag{2.27}$$

The phase factor $e^{iK\Lambda}$ is thus the eigenvalue of unit-cell translation matrix $(M_{11}, M_{12}, M_{21}, M_{22})$ and satisfies the secular equation $\begin{vmatrix} M_{11} - e^{iK\Lambda} & M_{12} \\ M_{21} & M_{22} - e^{iK\Lambda} \end{vmatrix} = 0$

The solutions are given by

$$e^{iK\Lambda} = \frac{1}{2}(M_{11} + M_{22}) \pm \left(\left[\frac{1}{2}(M_{11} + M_{22}) \right]^2 - 1 \right)^{\frac{1}{2}} \tag{2.28}$$

The eigenvectors corresponding to the eigenvalues are obtained from 2.27 and they are expressed as

$$\begin{pmatrix} A_0 \\ B_0 \end{pmatrix} = \begin{pmatrix} M_{12} \\ e^{iK\Lambda} - M_{11} \end{pmatrix} \tag{2.29}$$

For N^{th} unit cell the corresponding column vectors are given according to 2.26, as

$$\begin{pmatrix} A_N \\ B_N \end{pmatrix} = e^{-iNK\Lambda} \begin{pmatrix} M_{12} \\ e^{iK\Lambda} - M_{11} \end{pmatrix} \tag{2.30}$$

According to equations 2.13 and 2.26, the resultant expression representing the Bloch wave in layer 1 for the Nth unit cell is given by

$$E_K(z) = [(A_0 e^{-ik_{1z}(z-N\Lambda)} + b_0 e^{ik_{1z}(z-N\Lambda)}) e^{iK(z-N\Lambda)}] e^{-iKz} \tag{2.31}$$

where amplitudes A_0 and B_0 are given by Eq.2.29. It is important to note that the function inside the square bracket is independent of the number of unit cell (N) and hence, it is periodic with period Λ which is in agreement with the Bloch theorem Eq.2.24. The Bloch waves resulting from Eq. 2.31 could be considered as the eigenvectors of the unit cell translation matrix with eigenvalue $e^{iK\Lambda}$. Since the transfer matrix 2.19 is unimodular, the two eigenvalues are inversely related to each other. Equation 2.28 gives the dispersion relation between frequency (ω), longitudinal component (conserved quantity) of the wavevector (k_y) and the Bloch wave number K and it is expressed in the form

$$K(\omega, k_y) = \frac{1}{\Lambda} cos^{-1} \left[\frac{1}{2}(M_{11} + M_{22}) \right] \tag{2.32}$$

This dispersion relation results in the *photonic bandstructure* for a 1D periodic layered medium or a 1D PC. Now, three cases may arise

Case1: $|(M_{11} + M_{22})/2| < 1$

This corresponds to real Bloch wavenumber K and thus, depict a propagating Bloch wave.

Case2: $|(M_{11} + M_{22})/2| > 1$

The Bloch wave number K becomes complex, *i.e.* $K = m\pi/\Lambda + iK_i$. Due to the non-zero imaginary component (K_i), the Bloch wave has an evanescent envelope which cannot propagate in the medium. These regions are known as *photonic bandgaps* or *forbidden gaps* of the periodic medium.

Case3: $|(M_{11} + M_{22})/2| = 1$

This gives the photonic band edges, defining the band gaps of the periodic medium.

The dispersion relation 2.32 for TE and TM polarization could be written as [1, 2]

$$cosK\Lambda = \begin{cases} cosk_{1z}d_1 cosk_{2z}d_2 - \frac{1}{2}(\frac{k_{2z}}{k_{1z}} + \frac{k_{1z}}{K_{2z}})sink_{1z}d_1 sink_{2z}d_2 & \textbf{(TE)} \\ cosk_{1z}d_1 cosk_{2z}d_2 - \frac{1}{2}(\frac{n_1^2 k_{2z}}{n_2^2 k_{1z}} + \frac{n_2^2 k_{1z}}{n_1^2 K_{2z}})sink_{1z}d_1 sink_{2z}d_2 & \textbf{(TM)} \end{cases} \tag{2.33}$$

An example of the band structure for the special case $k_y = 0$ *i.e.* for normal incidence is shown in Fig.2.2. Case (a) shows the dispersion relation of a homogeneous medium, where
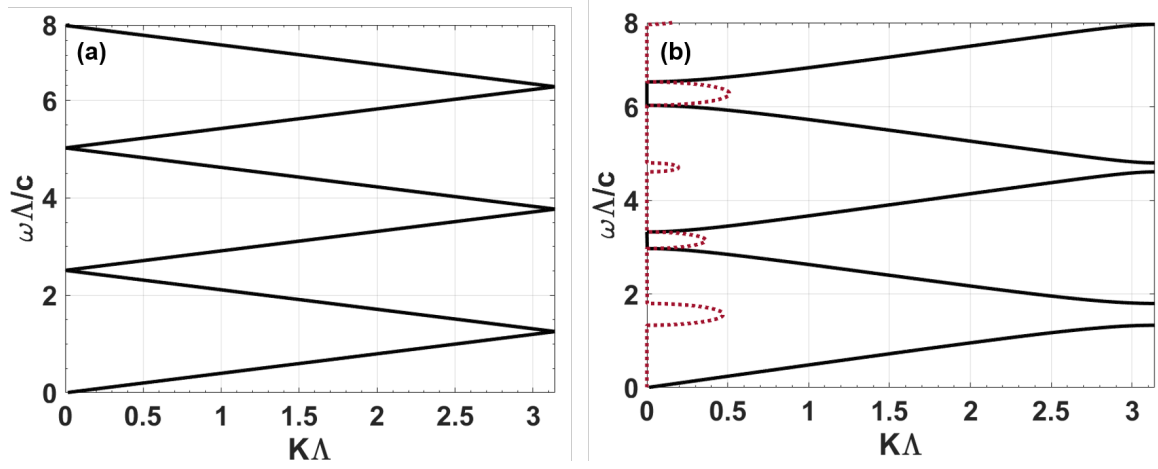
Figure 2.2: Shows the dispersion relation between ω and K for normal incidence *i.e.* for k_y = 0. a) For homogeneous medium with refractive index $n = 2.5$. b) For a periodic medium consisting of alternating layers of materials with refractive indices $n_1 = 2.5$ & $n_2 = 1.5$ and periodicity $\Lambda = 400nm$ $(d_1 = d_2 = 0.5\Lambda)$. The solid black line represents the real part of K and the dotted maroon line represents the imaginary part of K.

the refractive index is considered to be $n = 2.5$. This folding of the dispersion relation is shown only for elucidating a comparison and it does not have any physical significance. Fig.2.2(b) shows the dispersion relation for the periodic layered medium consisting of alternating layers of TiO_2 with refractive index $n_1 = 2.5$ and SiO_2 with refractive index $n_2 = 1.5$. The thicknesses of the layers are chosen to be $d_1 = d_2 = 0.5\Lambda$ and the period of the structure is taken as $\Lambda = 400\ nm$. The bandstructure in Fig.2.2 represents the dependence of the Bloch wave number (K) as a function of frequency (ω). For the periodic multilayered structure, the transmission bands or allowed bands are separated by clearly defined forbidden bands as shown in Fig.2.2(b). The imaginary part of K is shown by a dotted maroon line and the real(K) is shown by the black line.

In this section, we obtained an exact solution for the propagation of *em* wave in a periodic layered medium. The bandstructure, reflection, and transmission coefficients could be calculated easily using TMM. It is important to note that TMM is a purely numerical

technique and as a result, this method has some limitations in terms of computational requirements and its inability to get employed in two or three-dimensional geometries. Also, this method devoid us to gain any physical insight into the *em* coupling taking place amongst various modes (states) in the PC. To this end, a relatively less explored theory, known as the coupled-mode theory may offer some useful and interesting insights into the propagation features of *em* waves in PCs.

2.2   Coupled-mode theory (CMT)

In this section, we will discuss CMT-based formalism in which the periodic variation of the dielectric function is considered through the first-order perturbation technique. This dielectric perturbation gives rise to the *coupling* or *energy exchange* between the modes of the unperturbed (or uniform) medium. A periodic variation (with periodicity Λ) in dielectric constant (ϵ) along z-direction in a medium could be expressed as [3]

$$\epsilon(x, y, z) = \epsilon_0(x, y) + \Delta\epsilon(x, y, z) \tag{2.34}$$

where $\epsilon_0(x, y)$ is the unperturbed part of the dielectric constant, and $\Delta\epsilon(x, y, z)$ defines the periodic dielectric perturbation along the propagation or (z) direction. Since this dielectric perturbation is periodic along z, we can expand it as a Fourier series expansion

$$\Delta\epsilon(x, y, z) = \sum_{m \neq 0} \epsilon_m(x, y) e^{(-im\frac{2\pi}{\Lambda}z)} \tag{2.35}$$

This dielectric (along z) perturbation gives rise to the possibility of intermodal interactions. Let us consider any two modes, namely $|p\rangle$ and $|q\rangle$ propagating through the medium described by the dielectric function in equation (2.34). Assuming the *em* modes are propagating along z-direction, any arbitrary p^{th} and q^{th} mode could be expressed as

$$\begin{aligned} |p\rangle &= E_p(x, y) A_p(z) e^{i(\omega t - \beta_p z)} \\ |q\rangle &= E_q(x, y) A_q(z) e^{i(\omega t - \beta_q z)} \end{aligned} \tag{2.36}$$

24

Under the slowly varying approximation, the evolution of z-dependent mode-amplitude A_p and A_q of pth and q^{th} modes respectively could be expressed as [3]

$$\frac{dA_p}{dz} = -i\frac{\beta_p}{|\beta_p|}\sum_q\sum_m \kappa_{pq}{}^{(m)}A_q(z)e^{-i(\beta_q-\beta_p-m\frac{2\pi}{\Lambda})z}$$

$$\frac{dA_q}{dz} = -i\frac{\beta_q}{|\beta_q|}\sum_p\sum_m \kappa_{pq}^{*}{}^{(m)}A_p(z)e^{-i(\beta_p-\beta_q-m\frac{2\pi}{\Lambda})z} \tag{2.37}$$

where β_p and β_q are the longitudinal components of wavevector k_p and k_q respectively. $\kappa_{pq}{}^{(m)}$ defines the magnitude of the coupling coefficient which couples the modes through the mth Fourier component of dielectric function equation (2.34). The mth coupling coefficient is expressed as

$$\kappa_{pq}{}^{(m)} = \frac{\omega}{4}\int\int E^{*}{}_p(x,y)\epsilon_m(x,y)E_q(x,y)dxdy \tag{2.38}$$

where ϵ_m is the mth component of the Fourier-series expansion of ϵ (see equation (2.35)). The coupling between the interacting modes is maximum when the "longitudinal phase-matching" condition is exactly satisfied *i.e.*

$$\beta_p - \beta_q - m\frac{2\pi}{\Lambda} = 0 \tag{2.39}$$

2.2.1   Coupled-mode theory for photonic crystal

In the case of PC, the coupling between a forward propagating mode ($A_p \equiv A_i$) and a backward propagating mode ($A_q \equiv A_r$) is of interest. In the absence of any other intermodal interactions, the forward-backward mode coupling (assuming $m = 1$) would be governed by [3, 4, 5],

$$\frac{dA_r}{dz} = -i\frac{\beta_r}{|\beta_r|}\kappa A_i e^{i\Delta\beta z}$$

$$\frac{dA_i}{dz} = -i\frac{\beta_i}{|\beta_i|}\kappa^{*}A_r e^{-i\Delta\beta z} \tag{2.40}$$

where we have dropped the indices from κ and $\Delta\beta = \beta_r - \beta_i - \frac{2\pi}{\Lambda}$. In case, the PC constituent materials are isotropic, the dielectric function (equation (2.34)) is a purely scalar
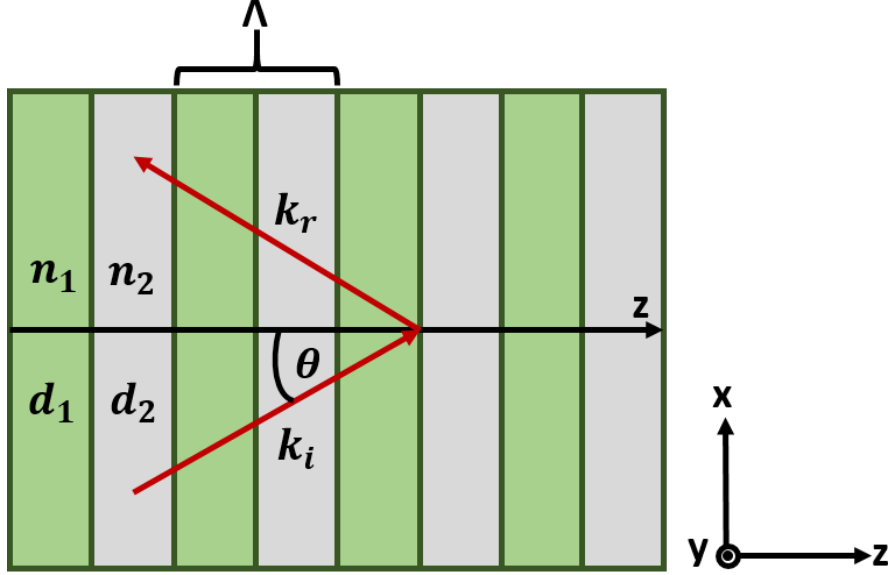
Figure 2.3: Oblique incidence of em-wave on distributed-Bragg-reflector (DBR) or 1D-photonic crystal. z-direction represents the optical axis.

and consequently, TE to TM mode-coupling (and vice-versa) is forbidden. It is worth noting that the phase-matching condition for coupling the forward propagating mode ($|i\rangle$) to a backward propagating mode ($|r\rangle$) or vice-versa is contra-directional in nature and therefore, Eq. (2.39) could be expressed as $\Delta\beta = 2\beta - \frac{2\pi}{\Lambda} = 0$ where $\beta_i = -\beta_r = \beta$ [3, 2]. As shown in Fig. 2.3, the phase-matching condition for the contra-directional coupling process is modified to $\Delta\beta = 2\beta\cos\theta - \frac{2\pi}{\Lambda} = 0$ in case of oblique incidence (θ with respect to z-axis). The coupled-mode equations (2.40) for contra-directional coupling will modify to a new set of equations given by,

$$\frac{dA_r}{dz} = -i\kappa A_i e^{i\Delta\beta z}$$
$$\frac{dA_i}{dz} = i\kappa^* A_r e^{-i\Delta\beta z}$$

(2.41)

For a simple case when the two layers of the DBR (with refractive indices n_1 and n_2) share the same thickness *i.e.* $d_1 = d_2$, the coupling coefficient takes a simplified form given by

[3],

$$\kappa_{TE} = \frac{i}{\lambda \cos \theta} \frac{\sqrt{2}(n_1{}^2 - n_2{}^2)}{\sqrt{(n_2{}^2 + n_1{}^2)}}$$

$$\kappa_{TM} = \frac{i}{\lambda \cos \theta} \frac{\sqrt{2}(n_1{}^2 - n_2{}^2)}{\sqrt{(n_2{}^2 + n_1{}^2)}} \cos 2\theta \tag{2.42}$$

The solution of coupled-mode equations (2.41) for *close-to-perfect* phase-matched $(\Delta\beta \approx 0)$ situation leads to a strong coupling from a forward propagating mode $(|i\rangle)$ to a backward propagating mode $(|r\rangle)$ for a broad range of frequencies. This is realized for all the frequencies within the PBG and consequently, we obtain a strong reflection band. It is apparent from equations (2.42) that the contrast in refractive index (or dielectric constant) is the primary factor determining the strength of coupling and hence, the sharpness of band edges. For a given choice of DBR constituents, $|n_1^2 - n_2^2|$ is fixed and consequently, the width of PBG remains unchanged.

In order to obtain the expression for the reflectivity, let's suppose that the em-wave is incident at $z = 0$ which results in a boundary condition given by

$$A_i(0) = 1,$$

$$A_r(L) = 0, \tag{2.43}$$

where A_i is the amplitude of the forward (or incident) wave and A_r is the amplitude of the backward (or reflected) wave and $z = L$ is the interaction distance when the incident mode is converted into the reflected mode. The solution of the coupled wave equation (2.41), is represented as

$$A_r(z) = e^{i(\Delta\beta/2)z} \frac{s \cosh s(L - z) + i(\Delta\beta/2) \sinh s(L - z)}{s \cosh sL + i(\Delta\beta/2) \sinh sL}$$

$$A_i(z) = e^{-i(\Delta\beta/2)z} \frac{-i\kappa^* \sinh s(L - z)}{s \cosh sL + i(\Delta\beta/2) \sinh sL} \tag{2.44}$$

where s is given by $s = \left[\kappa^*\kappa - (\Delta\beta/2)^2 \right]^{\frac{1}{2}}$. According to Eq. (2.44), reflectivity (R) is defined as

$$R = \left| \frac{A_r(0)}{A_i(0)} \right|^2 = \frac{\kappa^*\kappa \sinh^2 sL}{s^2 \cosh^2 sL + (\Delta\beta/2)^2 \sinh^2 sL} \tag{2.45}$$

27
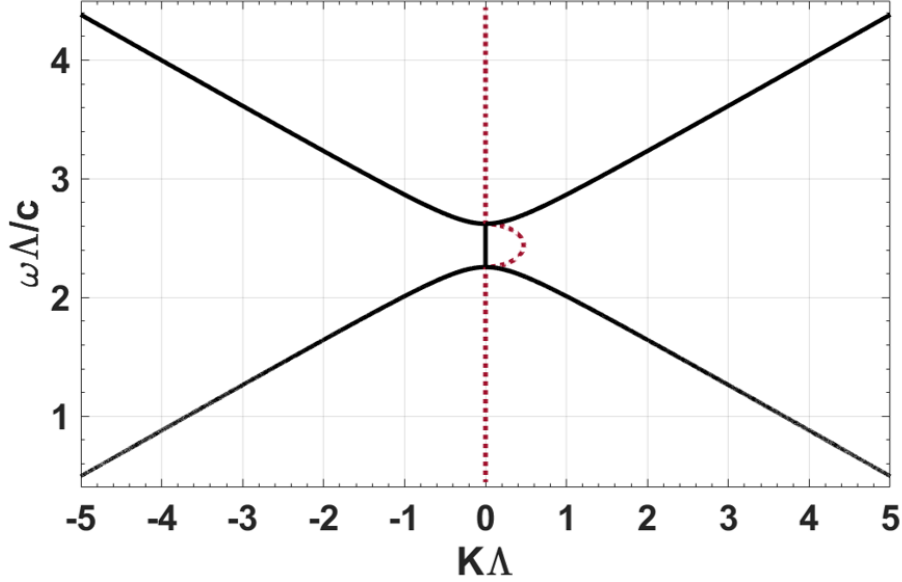
Figure 2.4: Shows the dispersion relation *i.e.* ω versus K relation for 1D-PC using CMT with $n_1 = 2.5$, $n_2 = 1.5$ and $d_1 = d_2 = 0.5\Lambda$. $Re(K)$ and $Im(K)$ are represented by solid black lines and dotted maroon lines, respectively.

As mentioned before, the reflectivity would be maximum when the phase matching condition is satisfied *i.e.* $\Delta\beta \approx 0$:

$$R_{max} = tanh^2|\kappa|L \tag{2.46}$$

Using Eq. (2.44) and $\Delta\beta = 2kcos\theta - m(\frac{2\pi}{\Lambda})$, we found that the z-dependent part of the coupled wave solutions in 1D PC is exponential with the propagation constant and could be written as

$$K = kcos\theta \pm is = \frac{m\pi}{\Lambda} \pm i\sqrt{\kappa^*\kappa - \left(\frac{\Delta\beta}{2}\right)^2} \tag{2.47}$$

Equation(2.47) describes the propagation characteristics of em-modes in the PC. The magnitude and width of PBG are derived by the values of κ and $\Delta\beta$. When $\Delta\beta < 2|\kappa|$, for certain range of frequencies K is complex. This region corresponds to the 'forbidden' region or alternately, the PBG. Using equation (2.47), a plot of real and imaginary K for $m = 1$ and $\theta = 0$ versus ω is shown in Fig.2.4. The structural parameters of the 1D PC in Fig.2.4

are the same as mentioned previously in Fig.2.2 ($n_1 = 2.5, n_2 = 1.5$ and $d_1 = d_2 = 0.5\Lambda$). It is important to note that for each value of m there exists a PBG whose central frequency satisfies $kcos\theta = m\pi/\Lambda, (m = 1, 2, 3...)$ and the results from CMT are consistent with that obtained through the Bloch-wave formalism.

References

[1] Pochi Yeh, Amnon Yariv, and Chi-Shain Hong. Electromagnetic propagation in periodic stratified media. i. general theory∗. *J. Opt. Soc. Am.*, 67(4):423–438, Apr 1977.

[2] Amnon Yariv and Pochi Yeh. *Photonics: Optical Electronics in Modern Communications (The Oxford Series in Electrical and Computer Engineering)*. Oxford University Press, Inc., USA, 2006.

[3] Amnon Yariv and Pochi Yeh. *Optical Waves in Crystals Propagation and Control of Laser Radiation*. New York Wiley, 1984.

[4] Ruchi Garg and K. Thyagarajan. Cascaded coupling: Realization and application to spectral maneuvering. *Opt. Fiber Tech.*, 19(2):148–153, 2013.

[5] K. Thyagarajan and Ruchi Garg Gupta. Coherent tunnelling adiabatic passage in optical fibres using superimposed long-period fiber gratings. *J. Mod. Opt.*, 63:1–9, 02 2016.

Chapter 3

Geometric representation of adiabatic distributed - Bragg - reflectors

3.1   Introduction

Adiabatic following, also known as rapid adiabatic passage (RAP), has been a well-established technique for realizing near 100% population transfer in a *two-level* atomic systems [1]. For example, RAP provides an efficient platform for ultrashort pulse frequency conversion as well as tailoring the spatial characteristics of optical beams in optical nonlinear medium [2, 3, 4, 5]. The theoretical basis, however, could be generalized to a broad class of systems exhibiting SU(2) symmetry.

In this chapter, we present an analogy of population transfer dynamics of a two-level atomic system with that of light propagation in a classical 'one-dimensional' photonic crystal, also known as distributed Bragg-reflector (DBR). This formalism facilitates adapting the idea of adiabatic following, more precisely RAP which is frequently encountered in a broad class of quantum-mechanical systems. A PC is primarily characterized by PBG whose magnitude is primarily dictated by the refractive index contrast of the PC constituents and the location in a spectral band is governed by the thickness of constituent layers [6]. Therefore, for a given pair of materials forming the PC, the magnitude of PBG is unique and fixed. Within the limit of optical transparency for the constituent PC materials, we present a formalism to broaden the PBG (and suppress the transmission band) by utilizing the concept of adiabatic coupling to a backward propagating mode from a forward propagating mode. Therefore, we draw an equivalence of the coupled-wave equations in a PC

with that encountered while describing the dynamics of quantum *two-level* atomic systems. Subsequently, we propose a plausible PC configuration for adopting the adiabatic following in such systems which leads to the broadening of the PBG spectrum. The formalism could be translated to any spectral band and the PBG broadening is limited by the restriction imposed by material transparency only. Interestingly, this idea provides a viable platform to tailor the backscattered phase from such systems as well. The intermodal coupling between counter-propagating modes as well as their phase-mismatch, for the photonic crystal configuration, exhibits a longitudinal variation which is usually observed in 'Allen-Eberly' scheme of adiabatic population transfer in *two-level* atomic systems [1].

3.2   Adiabatic phase-matching in photonic crystal

The coupled-mode equations for 1D PC (described in *section 2.2* of chapter 2) could be transformed into a rotating frame through the following substitution:

$$A_r = \tilde{a}_r e^{i/2[\Delta\beta(0)z - \int_0^z q(\tilde{z})d\tilde{z}]}$$

$$A_i = \tilde{a}_i e^{-i/2[\Delta\beta(0)z - \int_0^z q(\tilde{z})d\tilde{z}]}$$

$$(3.1)$$

where

$$\Delta\beta(z)z = \Delta\beta(0)z - \int_0^z q(\tilde{z})d\tilde{z}$$

Here, $\Delta\beta(0)$ is the phase-mismatch at $z = 0$ and $q(z)$ could be expressed as

$$\langle q(z) \rangle = \frac{1}{z}\int_0^z q(\tilde{z})d\tilde{z} = \Delta\beta(0) - \Delta\beta(z) = \frac{4\pi\bar{n}(z=0)}{\lambda} - \frac{4\pi\bar{n}(z)}{\lambda} \qquad (3.2)$$

where $\bar{n}$ is the average refractive index defined by $\bar{n} = \sqrt{\frac{d_{1M}n_1{}^2 + d_{2M}n_2{}^2}{\Lambda}}$ (for the Mth unit cell). The complex amplitudes $\tilde{a}_i$ and $\tilde{a}_r$ represent the power contained in the forward and backward propagating modes in the rotated frame of reference. It is worthwhile to note that $|\tilde{a}_i|^2 = |A_i|^2$ and $|\tilde{a}_r|^2 = |A_r|^2$. The transformed coupled-mode equations (2.41)

appear like

$$\frac{d\tilde{a}_i}{dz} - i\Delta k \tilde{a}_i = i\kappa^* \tilde{a}_r$$
$$\frac{d\tilde{a}_r}{dz} + i\Delta k \tilde{a}_r = -i\kappa \tilde{a}_i$$

(3.3)

where $\Delta k = \frac{\Delta\beta(0) - q(z)}{2}$. Equations (3.3) could be expressed through a single matrix equation given by,

$$i\frac{d}{dz}\begin{pmatrix} \tilde{a}_i \\ \tilde{a}_r \end{pmatrix} = \begin{pmatrix} -\Delta k & -\kappa^* \\ \kappa & \Delta k \end{pmatrix}\begin{pmatrix} \tilde{a}_i \\ \tilde{a}_r \end{pmatrix}$$

(3.4)

which is an equivalent representation of the time-dependent Schrödinger equation in quantum mechanics *i.e.*

$$i\bar{h}\frac{\partial}{\partial t}\Psi = \hat{H}(t)\Psi$$

(3.5)

If we define a state $|\Psi\rangle = \begin{pmatrix} \tilde{a}_r \\ \tilde{a}_i \end{pmatrix}$ then,

$$i\frac{d}{dz}|\Psi\rangle = \hat{H}|\Psi\rangle$$

(3.6)

We could observe that Eq. (3.6) is similar to the equation (3.5), where time-dependence is replaced by the z-dependence and the Hamiltonian can be represented as $\hat{H} = -\vec{\sigma}.\vec{B}$. Here, $\vec{\sigma} = (\sigma_x, \sigma_y, \sigma_z)$ is the triad comprising the Pauli-spin matrices and $\vec{B} = (Re(\kappa), Im(\kappa), \Delta k)$ represents a physical quantity equivalent to a source-driven magnetic field. Such symmetry considerations allow us to draw a one-to-one correspondence of the propagation dynamics of the photonic crystal with that of an interaction between spin-$\frac{1}{2}$ particle in a magnetic field. Specifically, in the case of PC, the Eqs. (2.42) results in $\vec{B} = (0, Im(\kappa), \Delta k)$ due to a vanishing real component of κ. The representation in Eq. (2.42) also depicts that $\kappa^* = -\kappa$. The isotropy of parameter space leads to rotational invariance and therefore, a $90°$ rotation of the state vector (defined below) around the z-axis would transform the magnetic field analog to $\vec{B} = (\tilde{\kappa}, 0, \Delta k)$, where $\tilde{\kappa}$ is the imaginary part of κ. The eigenvectors of the Hamiltonian ($\hat{H}$) are a linear combination of $|i\rangle$ and $|r\rangle$ with a suitable phase difference. The $|i\rangle$ and $|r\rangle$ are themselves eigenvectors of σ_z operator and are equivalent to the spin-up ($|\uparrow\rangle$) and spin-down ($|\downarrow\rangle$) states in the spin-$\frac{1}{2}$ particle in a magnetic field case [7].

3.3 Geometric representation

It is worth noting that $\langle q(z) \rangle$ given by equation (3.2) is zero for a conventional PC where the duty cycle is identical for each unit cell and consequently, the average refractive index ($\bar{n}$) is same for each unit cell. When the phase-mismatch and coupling coefficient change along the propagation direction z, the exact solution of the coupled-wave equations is not obvious. In order to study the dynamics of such a system, we could adopt a geometric approach prescribed by Bloch [8] and Feynman *et al.* [9]. The geometric representation of the transformed coupled-wave equation (3.4) could provide us with interesting physical insight into the propagation dynamics of em-waves in a PC which would enable us to understand the impact of spatially varying phase-mismatch and strength of coupling. It is worth noting that the complex eigenvalues and eigenvectors of Hamiltonian $\hat{H}$ are abstract quantities that are physically observable. In order to visualize the physical process, we define components of a vector also known as the state vector, which are functions of the complex eigenvectors. The state vectors provide us with a representational basis to describe the evolution of the generated fields. These state vectors are also known as Stokes vector and it is represented as $\vec{S} = (S_x, S_y, S_z)$ and are given by

$$S_x = \langle \sigma_x \rangle = \tilde{a}_i \tilde{a}_r{}^* + \tilde{a}_r \tilde{a}_i{}^*$$

$$S_y = \langle \sigma_y \rangle = -i[\tilde{a}_i \tilde{a}_r{}^* - \tilde{a}_r \tilde{a}_i{}^*] \tag{3.7}$$

$$S_z = \langle \sigma_z \rangle = |\tilde{a}_r|^2 - |\tilde{a}_i|^2$$

The z-dependent evolution of the state vector is dictated by the commutation relation of the state vector components with the Hamiltonian ($\hat{H}$) *i.e.*

$$\frac{\partial S_x}{\partial z} = -i\langle [\sigma_x, \hat{H}] \rangle$$
$$\frac{\partial S_y}{\partial z} = -i\langle [\sigma_y, \hat{H}] \rangle \tag{3.8}$$
$$\frac{\partial S_z}{\partial z} = -i\langle [\sigma_z, \hat{H}] \rangle$$

The above three equations could be written as a single vector precession equation of the form

$$\dot{\vec{S}} = \frac{\partial \vec{S}}{\partial z} = \vec{B} \times \vec{S} \tag{3.9}$$

Equation (3.9) represents that the $\vec{B}$-field exerts a *torque* on the system which leads to the precession of the state vector $(\vec{S})$ about $\vec{B}$ with a frequency $|\vec{B}| = \sqrt{\tilde{\kappa}^2 + \Delta k^2}$. It is important to mention that the quantity $(\tilde{a}_i \tilde{a}_i{}^* + \tilde{a}_r \tilde{a}_r{}^*)$ is the squared amplitude of the vector $\vec{S}$ which is given by

$$|\vec{S}| = (S_x^2 + S_y^2 + S_z^2)^{1/2} \tag{3.10}$$

$|\vec{S}|$ is a unimodular constant of motion when the components of the state vector are normalized. Equation (3.10) represents a sphere of the unit radius with a center at the origin and this sphere is known as the *Bloch Sphere*. The states and their evolution described by equations (3.7) and (3.9) determine the evolution dynamics of the forward and backward propagating modes. In other words, equations (3.7) and (3.9) could be mapped onto an equivalent Bloch-sphere where $|i\rangle$ (spin-up) and $|r\rangle$ (spin-down) states are located the *south*-pole and *north*-pole respectively. Any point of the PC Bloch-sphere represents a particular superposition of eigenstates $|i\rangle$ and $|r\rangle$. *Section 3.6* discusses the geometric representation in detail for specific cases of the evolution of these states.

It is worthwhile to point out that the value S_z (equation (3.7)) determines the mode-conversion efficiency. The state $\vec{S} = [0, 0, -1]$ represents a situation where the incident beam contains all the optical power *i.e.* $\tilde{a}_i = 1$ and the state $\vec{S} = [0, 0, 1]$ represents the case when all the optical power is present in the reflected beam ($\tilde{a}_r = 1$). Therefore, the conversion efficiency for the process of reflection is expressed as $\eta = \frac{S_z + 1}{2}$. Here, the dynamics is primarily controlled by the parameters Δk and κ which are essentially equivalent to factors *detuning* (Δ) and *Rabi-frequency* (Ω) respectively which are commonly encountered in the determining the population dynamics for a *two-level* atomic system.

3.4   Adiabatic following in a PC

It is apparent that $\Delta k = 0$ along the entire PC length for the central PBG frequency and $\Delta k \neq 0$ for all other frequencies. In a system where both the phase-mismatch (Δk) and the coupling coefficient (κ) are changing *slowly* along the propagation direction (z) is of immense interest. As a consequence of this z-varying phase-mismatch (Δk) and coupling coefficient (κ), the angle (ϕ) made by $\vec{B}$ with the z-axis also changes. As the state vector $\vec{S}$ precesses about $\vec{B}$, at every instant when $\vec{B}$ changes its direction, there is a corresponding change in the trajectory of $\vec{S}$ as depicted by Eq. (3.9). If we consider a situation where phase-mismatch (Δk) and coupling coefficient (κ) are changing slowly enough so as to bring about an adiabatic change in angle ϕ as a function of z then $\vec{S}$ will follow the path of the $\vec{B}$ throughout its evolution. This phenomenon is known as the *'adiabatic following'*. Under these conditions, $\vec{B}$ changes its direction very slowly as compared to the rotation frequency ($|\vec{B}| = \sqrt{\tilde{\kappa}^2 + \Delta k^2}$) with which the $\vec{S}$ is precessing around $\vec{B}$. The aforementioned condition is known as the *'rapid adiabatic passage' (RAP)* condition which ensures the adiabatic following and it is given by [1, 10]

$$\frac{d\phi}{dz} << |\vec{B}| \tag{3.11}$$

where $\Phi = tan^{-1}(\frac{\kappa}{\Delta k})$. When the adiabatic following is ensured by satisfying the RAP condition, an additional condition needs to be satisfied *i.e.* the phase-mismatch (Δk) should exhibit a large negative value at the entry face of the structure and must be a large positive value at the exit face of the structure.

In order to satisfy these conditions, we propose a PC configuration namely *chirped photonic crystal configuration* that leads to *slow* variation in Δk from a large negative to a large positive value along the PC length such that the sweep always remains much

smaller than the coupling (κ). This would ensure a nearly complete transfer of optical power from a forward propagating mode to a backward propagating mode across a frequency band extending much beyond the conventional PBG of a PC. Since both Δk and κ are changing as a function of z in the chirped photonic crystal, the RAP condition is expressed as [1, 11]

$$|\tilde{\kappa}\dot{\Delta k} - \Delta k\dot{\tilde{\kappa}}| << (\tilde{\kappa}^2 + \Delta k^2)^{3/2} \tag{3.12}$$

If $|\kappa|$ is assumed to be constant (along z), the adiabaticity condition appears as $\left|\frac{d\Delta k}{dz}\right| << \frac{(\tilde{\kappa}^2 + \Delta k^2)^{3/2}}{|\kappa|}$. In order to achieve complete optical power transfer, it is essential that the two states (modes) $|i\rangle$ and $|r\rangle$ are decoupled at the entry ($z = 0$) and exit ($z = L$) faces of the PC. Alternately, this is mathematically expressed as

$$\left|\frac{\Delta\beta}{\tilde{\kappa}}\right| >> 2 \ at \ z = 0, L \tag{3.13}$$

which is equivalent to satisfying the condition of *autoresonance* in 'two-wave' interaction system [12, 13]. In this case, *autoresonance* essentially ensures that the counter-propagating modes remain in phase even when the parameters of the Hamiltonian undergo an adiabatic change. This manifests into a complete transfer of optical power from the forward to the backward propagating mode, resulting in $\eta = 1$.

3.4.1 Chirped photonic crystal configuration for adiabatic mode - conversion

In order to adopt an adiabatic coupling scheme, we consider a PC configuration with a linear variation (or chirp in phase-mismatch Δk) in the duty cycle of each unit cell *i.e.* thickness $d_{1M} = d_1 + M\delta$ and $d_{2M} = \Lambda - d_1 - M\delta$ define the thickness of layers A and B respectively in M^{th} unit cell as shown in Fig. 3.1. The unit cell period (Λ), however, remains unchanged. Here, $M = 0, 1, 2, 3, ..., (N-1)$ where N is the total number of unit cells in the chirped-PC (CPC). The monotonic change in Δk is expressed through the average refractive index
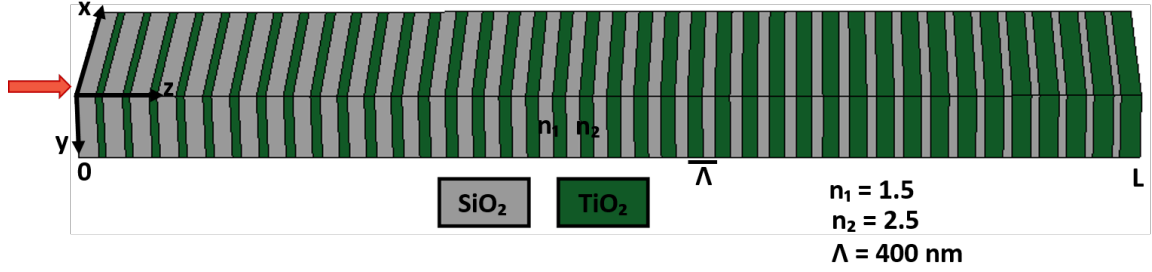
Figure 3.1: A schematic to describe the geometry of a chirped-DBR

change for an *unit cell* for which $\bar{n} = \sqrt{\frac{d_{1M}n_1{}^2 + d_{2M}n_2{}^2}{\Lambda}}$. It is worthwhile to note that the variation of $\bar{n}$ also manifests in the form z-dependence of κ. Using Eqs. (2.39) and (2.42), the variation in Δk and κ for normal incidence ($\theta = 0$) would be expressed as [14]

$$\Delta k \approx \frac{\Delta\beta}{2} = \frac{2\pi\bar{n}}{\lambda} - \frac{\pi}{\Lambda} \tag{3.14}$$

$$\kappa = \frac{i(1 - \cos\left(\frac{2\pi d_{1M}}{\Lambda}\right))}{2\lambda}\frac{(n_1{}^2 - n_2{}^2)}{\bar{n}} \tag{3.15}$$

For an arbitrarily chosen chirp-length of $\delta = 10\ nm$, $d_1 = 10\ nm$ and $N = 39$, the
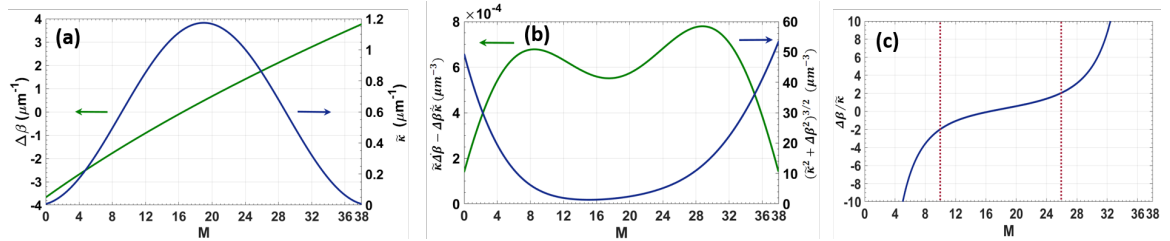
Figure 3.2: a) shows the variation of $\Delta\beta$ and $\tilde{\kappa}$ in M^{th} unit cell. b) shows the variation of LHS and RHS of the inequality given in Eq. (3.12) in M^{th} unit cell. c) shows the variation of $\frac{\Delta\beta}{\tilde{\kappa}}$ as a function of unit cell no. (M) for depicting a significant fraction of PC length satisfies the *(condition for auto-resonance)*.

variation in Δk and κ for the CPC is shown in Fig. 3.2(a). It is apparent that $\Delta\beta$ ($\approx 2\Delta k$) varies symmetrically from a large negative (at $z = 0$ or $M = 0$) to a large positive value (at $z = L$ or $M = 38$). The coupling coefficient (κ), on the other hand, reaches a maximum at

the center of CPC geometry ($M = 19$) and is negligibly small at $z = 0, L$. Figure 3.2(b) shows the variation of $|\tilde{\kappa}\frac{d\Delta\beta}{dz} - \Delta\beta\frac{d\tilde{\kappa}}{dz}|$ in M^{th} unit cell of CPC. It is apparent that this is much smaller than $(\tilde{\kappa}^2 + \Delta\beta^2)^{3/2}$ at any point within the CPC. Therefore, the adiabaticity condition described by equation (3.12) is completely satisfied in the case of CPC. It is interesting to note that the auto-resonant condition *i.e.* $\left|\frac{\Delta\beta}{\tilde{\kappa}}\right| < 2$ is satisfied in a significant fraction of the CPC ($M \approx 10$ to $M \approx 26$) as shown in Fig. 3.2(c) [13].
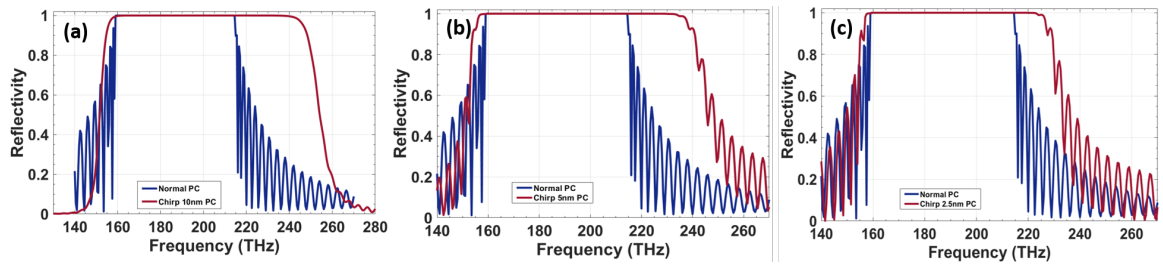
Figure 3.3: a), b) and c) show a comparison between the reflection spectrum of a normal-PC (blue line) of $d_1 = d_2 = 200\ nm$ with that for CPC (maroon line) having $\delta = 10\ nm$, $\delta = 5\ nm$ & $\delta = 2.5\ nm$ respectively.

The impact of closely satisfying the adiabatic constraints has a profound impact on the reflection spectrum shown in Fig. 3.3(a). In order to obtain the reflection spectrum, we consider a cross-section as shown in Fig. 3.1 where $N = 39$ is considered. A broadband plane wave is incident on the CPC from $z = 0$. The reflection spectrum was obtained using the finite element method (FEM) (wave-optics module, COMSOL Multiphysics). The periodic boundary condition is imposed along the transverse direction and a mesh size of $5\ nm$ is considered for the simulation. Also, we ignore the material dispersion in the present case and assumed $n_1 = 1.5$ ($A \equiv SiO_2$) and $n_2 = 2.5$ ($B \equiv TiO_2$) across the entire spectrum. In order to compare, the reflection spectrum for a normal PC (no-chirping and $\Lambda = 400\ nm$) is also shown in 3.3(a). It is evident that there is a $\approx 40\ THz$ increase in PBG for CPC as compared to the normal PC. Also, the reflectivity drop at the band edges is relatively smooth with complete suppression of small reflection resonances outside the

PBG.

In fact, any alteration in structural parameters has an impact on $\Delta\beta$ and κ and consequently, the adiabatic constraints are not satisfied closely. This is expected to reduce the PBG in the reflection spectrum along with the appearance of sharp transmission resonance (outside PBG). For example, when the chirp-length changes to $\delta = 5\,nm$ with $d_1 = 100\,nm$ and $N = 39$, the reflection spectrum is shown in Fig. 3.3(b) where the PBG shrinks to $\approx 30\,THz$. It is also worth noting that the reflection spectrum is accompanied by oscillating side bands with sharp transmission resonances on both sides of the PBG. On reducing the factor determining the duty cycle *i.e.* $\delta = 2.5\,nm$ ($d_1 = 150\,nm$ and $N = 39$), the PBG for CPC shrinks to $15\,THz$ and discernibly sharper and intense transmission resonances on both sides of the PBG which is similar to that exhibited by normal PC. The underlying cause behind this observation could be traced to the variation of κ (see equation (3.15)). By reducing the chirp length δ (without changing the PC length L), the minimum value of $\tilde{\kappa}$ (at $z = 0$) and $z = L$) increases. Therefore, the forward and backward propagating modes are not completely decoupled at the ends of C-DBR when $\delta = 5\,nm$ and $\delta = 2.5\,nm$. However, the reduction of the chirp length δ has a weak impact on $\frac{d\Delta\beta}{dz}$. Overall, the adiabaticity conditions are partially satisfied for smaller chirp lengths and consequently, we obtain a smaller PBG. The CPC, in general, could be viewed as a geometry comprised of a stacked group of normal PCs with varying duty cycles. Accordingly, the PBG due to neighboring unit cells in the CPC overlaps partially with each other. From this perspective, a random variation in d_{1M} and d_{2M}, say up to 10% results in a negligible change in the overall PBG of CPC.

3.5 Equivalence with a two-level system

The analogy between a dynamical evolution of the population in a two-level atomic system and the propagation dynamics in a DBR is apparent from Eqs. (3.7) and (3.9) where the time-evolution has been replaced by evolution along z-axis. The ground-state and excited-state populations are analogues to complex amplitudes $\tilde{a}_i$ and $\tilde{a}_r$ respectively. The parameters determining the geometrical path Δ (frequency detuning) and Ω (Rabi frequency) are replaced by Δk (phase-mismatch) and κ (coupling coefficient). Table 3.1 presents the equivalent quantities for these two systems.

Parameters	Population dynamics in two-level atomic system	Wave propagation in photonic crystal
Evolution parameter	t	z
States	$\lvert g \rangle$, $\lvert e \rangle$	$\lvert a_i \rangle$, $\lvert a_r \rangle$
Detuning/phase-mismatch	Δ	Δk
Rabi frequency/coupling strength	Ω	κ
Torque creating field ($\vec{B}$)	$(Re(\Omega),\ Im(\Omega),\ \Delta)$	$(Re(\kappa),\ Im(\kappa),\ \tilde{\Delta k})$

Table 3.1: Shows an equivalence between the parameters determining the population dynamics of a two-level atomic system and a photonic crystal

3.6 Geometric representation of propagation characteristics in PC

3.6.1 On-resonance

The dynamical trajectory on the Bloch-sphere for a perfectly phase-matched ($\Delta k = 0$) interaction in the PC should resemble an on-resonance interaction in a two-level atomic system. Due to the fact that we have a one-to-one mapping between the respective parameters in a *two-level atomic system* with that for a PC, we expect identical solutions for Eq. (3.9) in the context of resonant interaction as well as interaction under adiabatic constraints

in a PC [1]. Therefore, the dynamics exhibited by the state vector $(\vec{S})$ corresponding to the central PBG frequency ($\Delta\beta = 0$ and κ is a constant) for a normal PC is given by [1]

$$
\begin{aligned}
S_x &= 0 \\
S_y &= sin(\tilde{\kappa}z) \\
S_z &= -cos(\tilde{\kappa}z)
\end{aligned}
\tag{3.16}
$$

It is apparent from Eq. (3.16) that if the PC is truncated at a length ($z = L$) such that
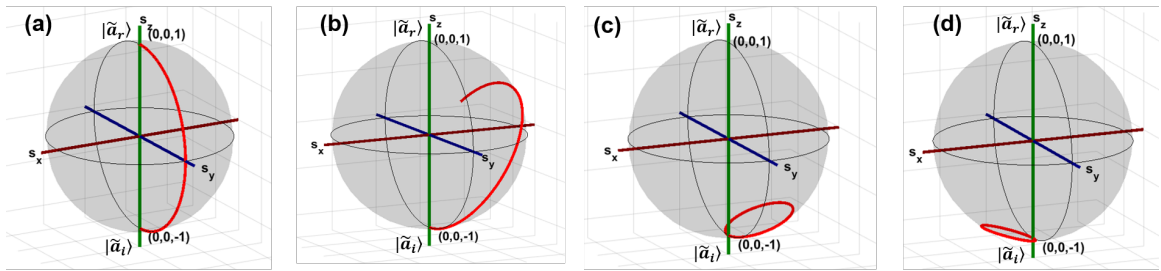
Figure 3.4: Shows the evolution of state vector $\vec{S}$ on the Bloch sphere for the normal PC at frequencies a) $\nu_c = 181.8\,THz$ (central frequency) b) $\nu = 200\,THz$ c) $\nu = 300\,THz$ d) $\nu = 120\,THz$.

($\tilde{\kappa}.L = \pi$), there will be a complete conversion of $|\tilde{a}_i\rangle$ to $|\tilde{a}_r\rangle$ at that point. However, $R = 1$ is not a completely correct assertion as the reflectivity is defined at $z = 0$. In the resonant ($\Delta k = \Delta\beta = 0$) interaction case for a normal PC, a complex κ (see Eqs. (2.42)) ensures a finite return of power to the forward propagating mode ($|\tilde{a}_i\rangle$) whenever $|\tilde{a}_r| > |\tilde{a}_i|$. Consequently, the reflectivity (R) or the conversion efficiency (η) of a conventional PC with finite length will always be less than unity (< 1). Fig. 3.4(a) represents such an evolution where the state vector ($\vec{S}$) traverses from the south pole to the north pole along the great circle (red-curve). This pertains to a complete transfer of optical power from the incident beam to the reflected beam in the PC. Here, the PC has periodicity $\Lambda = 400\,nm$, $d_1 = d_2 = \frac{\Lambda}{2}$ with $n_1 = 2.5$ & $n_2 = 1.5$ and the PBG central frequency is $\nu_c = 181.8\,THz$ (where $\Delta k = 0$).

3.6.2 Off-resonance

Any non-zero Δk (analogous to detuned interaction in a two-level system) would essentially imply a smaller mode conversion. We again assume that the coupling coefficient κ is constant in this case. The solutions for the different components of the state vector are given by [1]

$$S_x = \frac{\Delta k \kappa}{|\vec{B}|^2}[1 - cos(|\vec{B}|z)]$$
$$S_y = -\frac{\kappa}{|\vec{B}|}sin(|\vec{B}|z)) \quad\quad (3.17)$$
$$S_z = -\frac{\Delta k^2 + \kappa^2 cos(|\vec{B}|z))}{|\vec{B}|^2}$$

The trajectory described by equation (3.17) makes an angle $\phi = tan^{-1}(\tilde{\kappa}/\Delta k)$ with respect to the z axis. Consequently, the trajectory will not follow a semicircular rotation on the Bloch sphere. As a result the state vector never reaches the north pole of the Bloch sphere. This implies that a complete transfer of power from the incident mode ($|i\rangle$) to the reflected mode ($|r\rangle$) is not possible for an off-resonant case. For the frequencies within the PBG (say $\nu = \frac{c}{\lambda} = 200\,THz$), the dynamical trajectory would result in termination of the state-vector ($\vec{S}$) at some point on the surface of northern-hemisphere of the PC Bloch sphere as shown in Fig. 3.4(b). Interestingly, for frequencies outside the PBG ($|\Delta k| >> 0$) or in the transmission band (say $\nu = 300\,THz$ or $\nu = 120\,THz$), the dynamical trajectory traced by $\vec{S}$ terminates within the southern hemisphere which could be observed in Figs. 3.4(c) and (d) respectively.

3.6.3 Adiabatic coupling

In order to represent the mode-coupling dynamics in a CPC, we seek the solutions to Eq. (3.9) under the constraints imposed by the adiabatic following. When the angle (Γ) between
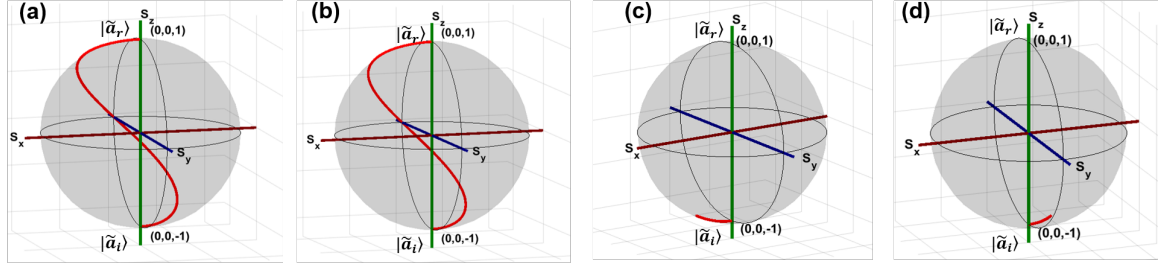
Figure 3.5: Shows the evolution of state vector $\vec{S}$ on the Bloch sphere for the CPC at frequencies (a) $\nu_c = 181.8\ THz$ (b) $\nu = 200\ THz$ (c) $\nu = 300\ THz$ and (d) $\nu = 120\ THz$ respectively.

.

$\vec{B}$ field and the state vector $\vec{S}$ is very small, the exact solutions could be expressed as [1],

$$
\begin{aligned}
S_x &= \frac{-\tilde{\kappa}cos(\Gamma)}{\sqrt{\tilde{\kappa}^2+\Delta k^2}} \\
S_y &= \frac{\tilde{\kappa}sin(\Gamma)}{\sqrt{\tilde{\kappa}^2+\Delta k^2}} \\
S_z &= \frac{\Delta k}{\sqrt{\tilde{\kappa}^2+\Delta k^2}}
\end{aligned}
\tag{3.18}
$$

Therefore, R (or η) could be exactly *unity* if $\tilde{\kappa} = 0$ or $\Delta k \rightarrow \infty$ at $z = L$. From Fig. 3.2(a), it is apparent that the former condition is exactly satisfied in the case of the designed CPC and consequently, we would have $R = 1$. Due to the fact that $\tilde{\kappa} = \tilde{\kappa}(z)$ and $\Delta\beta = \Delta\beta(z)$ (see Fig. 3.2(a)), $\vec{S}$ follows a spiraling trajectory from the south-pole to the north-pole. The geometric representation for a CPC is shown in Fig. 3.5 for frequencies within the PBG (Fig. 3.5a,b) as well as outside the PBG (Fig. 3.5c,d). Since, the parameters Δk and κ exhibit a *slow* longitudinal variation, $\vec{S}$ always remain perpendicular to $\vec{B}$ at each z. Figure 3.5(a) represents a dynamical trajectory of $\vec{S}$ (at $\nu_c = 181.8\ THz$) for the variation in Δk (or $\Delta\beta$) shown in Fig. 3.2(a). In this case, $\vec{S}$ traverses from the south pole to the north pole through a spiraling trajectory and this results in the complete conversion of $|i\rangle$ to $|r\rangle$ as shown in Fig. 3.6(b).
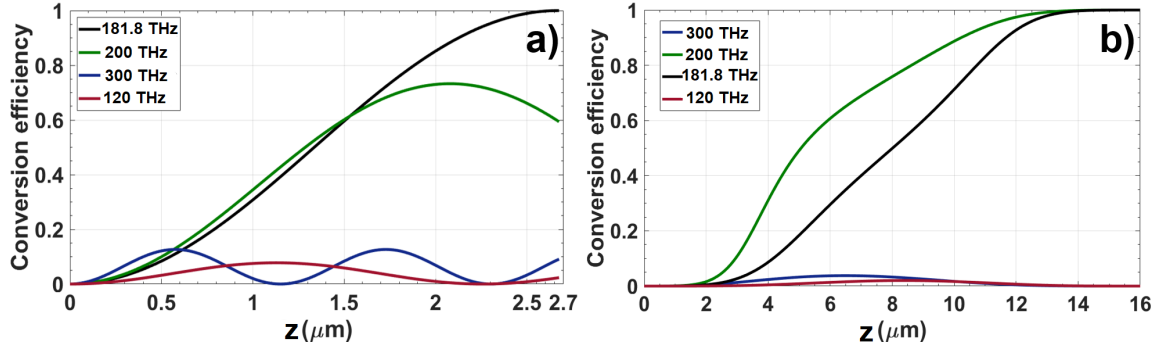
Figure 3.6: a) and b) shows the variation of conversion efficiency as a function of propagation distance for normal PC and CPC at frequencies used in Fig. 3.4 and 3.5. The black solid line represents the evolution of the central frequency of the PBG and the green solid lines for the frequency that lies closer to the band edges. The blue/purple solid lines correspond to frequencies that lie outside the PBG.

3.6.4 Conversion efficiency

The conversion efficiency or the reflectivity ($\eta = \frac{S_z + 1}{2}$) as a function of propagating distance (z) for all the aforementioned frequencies in normal PC is shown in Fig.3.6(a). It could be noted that $\eta < 1$ for all the frequencies except central PBG frequency ($\nu_c = 181.8\,THz$) which is consistent with the description in Fig. 3.4. In the case of CPC, the conversion efficiency reaches unity through a different path as shown in Fig. 3.5(b).

3.6.5 Oblique incidence and angular dispersion

A detailed comparison of the reflection spectrum and the dispersion for a normal PC and a CPC (with $\delta = 10\,nm$) is elucidated in Fig. 3.7(a)-(d). The dependence of the reflection spectrum on angle-of-incidence (AOI) for TE and TM polarization in a normal PC is shown in Fig. 3.7(a) and (b) respectively. The oblique incidence essentially leads to a smaller value of projection of the normal component of the wavevector. Consequently, the PBGs shift to higher frequencies at higher AOIs. As expected, the PBGs tend to broaden for the TE polarization on oblique incidence. On the other hand, the low-frequency PBGs for TM polarization tend to reduce up to an AOI $\approx 60°$ and increase thereafter. The drop

in PBG for TM polarization is essentially due to Brewster's angle effect at the interface of high and low-index layers. Figure 3.7(c) and (d) represent the reflection spectrum for the TE and TM polarization respectively for the CPC. A comparison between Fig. 3.7(a) and (c) reveals that the CPC exhibits appreciably broad PBGs with appreciably narrow transmission bands separating them. At oblique incidence, the PBG in CPC broadens further and
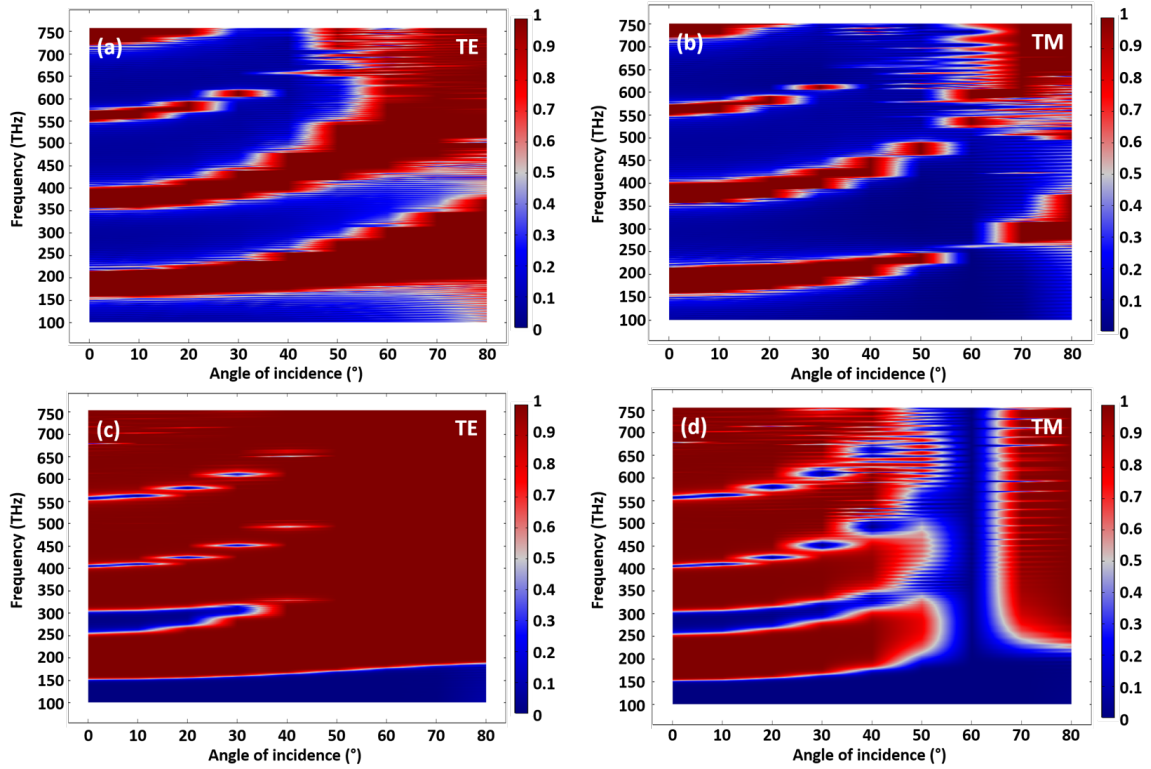
Figure 3.7: a) and b) shows the variation reflection spectrum for TE and TM polarization respectively in a normal PC ($Lambda = 400\ nm$ and $d_1 = d_2$) as a function of angle of incidence. c) and d) shows the reflection spectrum for TE and TM polarization respectively in CPC as a function of the angle of incidence. The CPC parameters are $\delta = 10\ nm$ and $d_1 = 10\ nm$. In all the cases, the total number of units is $N = 39$.

shifts to higher frequencies. This is accompanied by the shrinking of transmission bands. In fact, the PBGs tend to overlap for AOI $\geq 50°$, thereby leading to a high-reflection band extending from $150\ THz$ to $750\ THz$ ($1600\ nm$ band). Such broad PBGs are usually not found in normal PC, even with very wide refractive index contrast. It is also interesting to

note that the reflection spectrum (in Fig. 3.7(c)) exhibits three omnidirectional PBGs which are located in $200 - 250\,THz$, $310 - 400\,THz$ and $490 - 550\,THz$ frequency range. The PBG, in this case (for normal as well as oblique incidence), is limited by the material transparency window and could be extended further (on both spectral ends) through a suitable choice of materials. A similar comparison between Fig. 3.7(b) and (d) depicts broadened PBG in the case of TM polarization in CPC and narrow transmission bands. However, Fig. 3.7(d) exhibits a sharp transmission resonance at Brewster's angle ($\approx 60°$). By taking material dispersion into consideration, we expect a small change ($\pm 1°$) in Brewster's angle and hence, an insignificant change in the transmission spectrum. The PBGs tend to merge thereafter ($\geq 65°$) giving rise to a broad high reflection band. A comparison between Fig. 3.7(c) and (d)reveals that the CPC could be employed as a broadband ($\approx 150 - 750\,THz$) polarization filter for $\approx 60°$ AOI.

3.7   Conclusions

In conclusion, we present an approach to understand the propagation characteristics of modes in a PC using general techniques adopted in a wide variety of systems exhibiting *SU(2)* dynamical symmetry. The coupled-mode equations describing the forward and backward propagating modes in a PC could be represented in the form of a single *optical* Bloch-equation where the evolution of the state vector depicts the dynamical behavior of the wave propagation. This provides a platform to draw an analogy with a *two-level* atomic system and consequently, adopt a formalism for adiabatic evolution in PC-based configurations. In order to realize conditions imposed by adiabatic constraints, CPC configurations have been investigated in detail. This PC variant exhibit enhancement of PBG along with varying degrees of suppression of sharp transmission resonances in the reflection spectrum. The impact of alteration of the physical parameters for the PC is explored in detail. It is

worth pointing out that the CPC configuration involves a discernible longitudinal variation in mode-coupling coefficient κ in addition to the sweep in Δk (or $\Delta\beta$).

References

[1] L. Allen and J. H. Eberly. *Optical Resonance and Two-Level Atoms*. Dover Publications, 1987.

[2] Haim Suchowski, Dan Oron, Ady Arie, and Yaron Silberberg. Geometrical representation of sum frequency generation and adiabatic frequency conversion. *Phys. Rev. A*, 78:063821, 07 2008.

[3] Aviv Karnieli and Ady Arie. Fully controllable adiabatic geometric phase in nonlinear optics. *Opt. Express*, 26(4):4920–4932, Feb 2018.

[4] Aviv Karnieli and Ady Arie. All-optical Stern-Gerlach effect. *Phys. Rev. Lett.*, 120:053901, 01 2018.

[5] Yongyao Li, Ofir Yesharim, Inbar Hurvitz, Aviv Karnieli, Shenhe Fu, Gil Porat, and Ady Arie. Adiabatic geometric phase in fully nonlinear three-wave mixing. *Phys. Rev. A*, 101:033807, Mar 2020.

[6] Amnon Yariv and Pochi Yeh. *Photonics Optical Electronics in Modern Communications*. Oxford University, 6th edition, 2007.

[7] R. Feynman, F. Vernon, and R. Hellwarth. Geometrical representation of the Schrödinger equation for solving maser problems. *J. Appl. Phys.*, 28:49–52, 1957.

[8] F. Bloch. Nuclear induction. *Phys. Rev.*, 70:460–474, Oct 1946.

[9] Richard P. Feynman, Jr. Vernon, Frank L., and Robert W. Hellwarth. Geometrical Representation of the Schrödinger Equation for Solving Maser Problems. *Journal of Applied Physics*, 28(1):49–52, January 1957.

[10] Yongyao Li, Ofir Yesharim, Inbar Hurvitz, Aviv Karnieli, Shenhe Fu, Gil Porat, and Ady Arie. Adiabatic geometric phase in fully nonlinear three-wave mixing. *Phys. Rev. A*, 101:033807, Mar 2020.

[11] Eyal Bahar, Xiaoyue Ding, Asaf Dahan, Haim Suchowski, and Jeffrey Moses. Adiabatic four-wave mixing frequency conversion. *Opt. Express*, 26(20):25582–25601, Oct 2018.

[12] Andrey Markov, Anna Mazhorova, Holger Breitenborn, Andrew Bruhacs, Matteo Clerici, Daniele Modotto, Ottavia Jedrkiewicz, Paolo di Trapani, Arkady Major, François Vidal, and Roberto Morandotti. Broadband and efficient adiabatic three-wave-mixing in a temperature-controlled bulk crystal. *Opt. Express*, 26(4):4448–4458, Feb 2018.

[13] O. Yaakobi, L. Caspani, M. Clerici, F. Vidal, and R. Morandotti. Complete energy conversion by autoresonant three-wave mixing in nonuniform media. *Opt. Express*, 21(2):1623–1632, Jan 2013.

[14] Amnon Yariv and Pochi Yeh. *Optical Waves in Crystals Propagation and Control of Laser Radiation*. New York Wiley, 1984.

Chapter 4

Infrared rainbow trapping via optical Tamm modes

4.1 Introduction

Rainbow trapping is a phenomenon of slowing down (in principle stopping) a broadband optical radiation in one- or two-dimensional stratified photonic systems [1, 2, 3]. The excitation of surface-plasmon (SP) modes in a PC provides a plausible mechanism for trapping electromagnetic (em) radiation. Consequently, the configurations deployed for rainbow trapping are predominantly metallo-dielectric or all-metallic [4, 5, 6, 7]. Although a significant reduction in group velocity ($v_g \leq 0.1c$) is achieved in such configurations, the absorption losses (α) in plasmon-active metals limit the trapped-mode lifetime (T_r) in the visible spectral band [1, 5, 8, 9]. The impact turns more significant in the infrared (IR) band ($\geq 1\,\mu m$ wavelength) where the absorption losses (by metals) are very high. Therefore, the recurring challenge is to develop plausible strategies which offer appreciably low loss along with small v_g over broad bandwidth in metallo-dielectric configurations. All-dielectric PCs have been proposed for trapping light in the visible and IR band but they exhibit maximum $T_r \sim 0.2 - 0.3\,ps$ which limits their applicability in a variety of settings [1, 10]. The graded-Si based composite gratings with SiO_2 spacer-layers offer a reliable platform for slowing down wavelengths $\geq 2\,\mu m$ in the IR band [11]. Recently, through graphene-incorporated graded-Si gratings, the phenomenon of rainbow trapping in the $10 - 50\,THz$ range is realized with slowdown factors $\sim 0.001c$ [11]. However, the trapped plasmon modes still exhibit a sub-picosecond lifetime essentially due to higher losses. The all-dielectric PCs of-

fer a low-loss flexible platform for light-trapping through the excitation of optical surface states. Such states could be excited at the interface of two different topologically non-trivial PCs or at the interface of a topologically non-trivial PC and homogeneous medium [12, 13]. Optical Tamm (OT) states, which exist at the interface between a plasmon-active metal and a 1D PC, could be classified in the second category [12]. The OT states are strongly confined near the PC-metal interface and exhibit a parabolic dispersion curve. Importantly, their dispersion lies within the light cone given by $k_{||} = \frac{\omega}{c}$, where $k_{||}$ is the in-plane wavevector component and ω is the angular frequency of light. Consequently, TE, as well as TM polarization, could be excited through free-space coupling at normal incidence [14, 12]. Due to the possibility of free-space coupling to OT modes, the coupling efficiencies are very high ($\geq 90\%$) which allows efficient device realization [15]. In the last decade, OT states/modes have attracted a wide range of applications which include high-sensitivity optical sensing devices, narrowband tunable filters, optical switches, harmonic generators, slow-light devices, etc. [16, 17, 18, 19, 20]. The nature of OT resonance in a 1D PC yield localization of em-field at one resonant frequency only and therefore, any light trapping mechanism using OT states would be narrow band [20]. Many processes such as rainbow trapping or non-degenerate frequency conversion essentially require multiple non-degenerate OT states in the same PC for broadband applications.

4.2 Theoretical framework

Here, we considered a 1D linearly chirped all-dielectric PC, described in *section3.4.1* of chapter 3 which supports multiple optical Tamm-like modes. The OT modes are spatially separated within the PC and facilitate a broad spectrum to be trapped. As we have discussed in Chapter 3, this system is equivalent to a 'two-level' quantum system, the propagation characteristics of a PC with well-defined periodicity could be described using the Bloch-
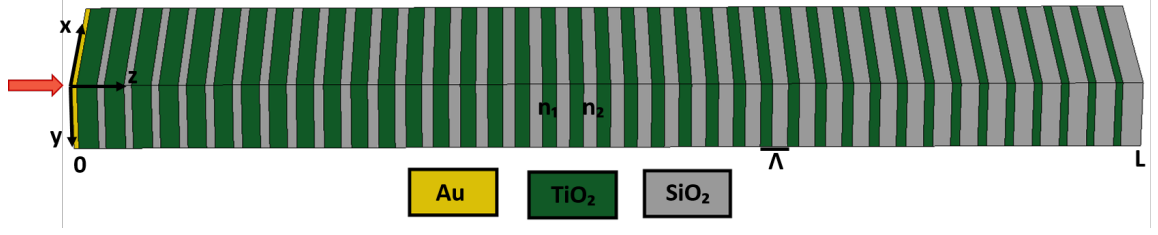
Figure 4.1: a) A schematic of the chirped-PC geometry with a fixed periodicity (Λ) but a variable duty cycle.

wavevector given by $K = \frac{m\pi}{\Lambda} \pm i\sqrt{\kappa^*\kappa - \left(\frac{\Delta\beta}{2}\right)^2}$ [21]. Consequently, the width of PBG as well as the reflected beam amplitude is governed by the values of κ and $\Delta k (\approx \Delta\beta/2)$. Since K is complex within the PBG, then $|\kappa|^2 \geq (\frac{\Delta\beta}{2})^2$) defines the edges of PBG for the PC. In analogy with adiabatic population transfer in *two-level* atomic system, a plausible route for maximizing η is to vary Δk such that the adiabatic constraint given by $\frac{d\Delta k}{dz} << |\kappa|^2$ is obeyed at each z. The longitudinal variation in Δk is brought about by a linear chirp in the thickness of layers A and B described before in *section 3.4.1* of chapter 3. The CPC configuration which ensures adiabatic following has two distinct features. (a) PBG for an optimally CPC increases (b) CPC exhibits *multiple* phase-jumps ($[0 \to \pi]$ or $[0 \to -\pi]$) within the PBG. These points will be apparent in the example considered below.

4.3 Photonic bandgap computation and results

Let us consider layer $A \equiv TiO_2$ and layer $B \equiv SiO_2$. The linear chirp leads to a longitudinally varying *average* refractive index ($\bar{n} = \sqrt{\frac{d_{1m}n_1^2 + d_{2m}n_2^2}{\Lambda}}$). We assume $\Lambda = 400\ nm$, $\delta = 10\ nm$, $N = 39$ and $m = 1, 2, 3, ...(N-1)$ and subsequently, we simulate the reflection spectrum using finite element technique (COMSOL Multiphysics). In the simulations, the periodic boundary condition is imposed in the transverse direction and a mapped mesh is used with a maximum element size of $30\ nm$. The material dispersion

for TiO_2 and SiO_2 is obtained from [22]. The blue-solid curve in Fig. 4.2(a) represents the broadband ($\approx 80\,THz$ broad) reflection spectrum for the CPC. The reflection spectrum is marked by discernible suppression of sharp reflectivity peaks outside the PBG. The peaks are distinct features of finite periodic PCs. In fact, the transmission band (characterized by $\nu \leq 150\,THz$ or $\nu \geq 260\,THz$) is reasonably flat, and the transmission $T \geq 95\%$. A comparison of the reflection spectrum (not shown here) for a periodic 1D PC ($d_1 = d_2 = 200\,nm$) shows that the PBG for CPC is approximately $\approx 40\,THz$ broader than that for a periodic PC. In order to appreciate this point, we represent the spectral variation
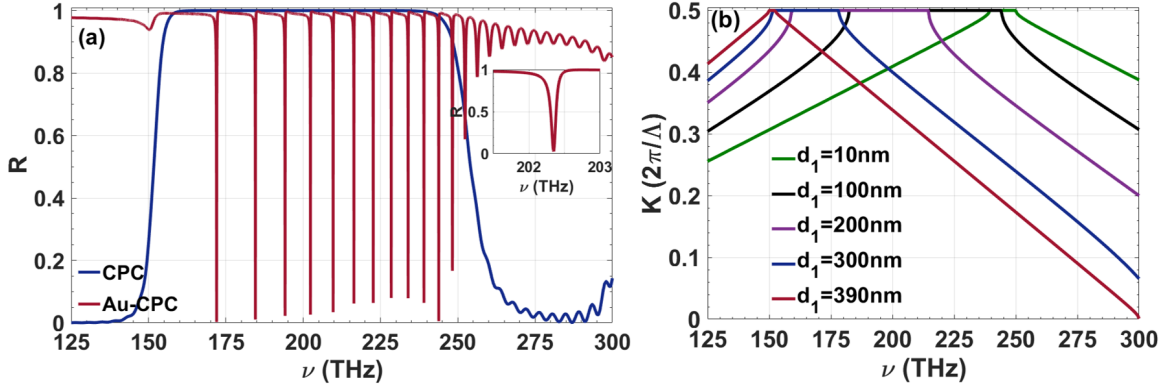
Figure 4.2: a) The reflection spectrum of CPC (solid blue line) for $N = 39$ unit cells and Au-CPC (red line) and the inset shows the zoomed figure of one of the OT modes. b) Represents dispersion relation *i.e.* Bloch-wavevector (K) versus frequency (ν) for periodic TiO_2/SiO_2 based PC geometries when $d_1 = 10\,nm$ (green curve), $d_1 = 100\,nm$ (black curve), $d_1 = 200\,nm$ (purple curve), $d_1 = 300\,nm$ (blue curve) and $d_1 = 390\,nm$ (maroon line). All the PCs (with different d_1) have identical periodicity ($\Lambda = 400\,nm$).

in the real part of the Bloch-wavevector (K) of periodic 1D PCs with different values of d_1 such that $d_1 + d_2 = \Lambda = 400\,nm$ for all the PCs in Fig. 4.2(b). The flat region (for each d_1) depicts the PBG (where K is complex and its real part is constant $= \frac{2\pi}{\Lambda}$) for each PC. It is apparent that the PBGs for each PC (having different d_1 and d_2) approximately span the wide spectral band from $150\,THz$ to $250\,THz$. This explains the origin of broad PBG as well as the suppression of reflectivity peaks outside the PBG in CPC. It is worthwhile to point out that the linear-chirp in PC ensures a symmetric variation of Δk from a negative

to a positive value and $\frac{d\Delta k}{dz} << |\kappa_s|^2$ at any z (as shown in figure 3.2(a)).

In order to excite OT-like states/modes in the CPC, we place a thin Au-layer ($d_m = 30\ nm$) adjacent to the first TiO_2 layer (A) as shown in Fig. 4.1(a). The simulated reflection spectrum using COMSOL Multiphysics is represented by the red curve in Fig. 4.2(a) which is characterized by a sharp drop in reflectivity within the PBG of CPC. Such sharp resonances are a signature of OT modes in metallo-dielectric geometries and usually, the OT mode-field decays away from the metal-dielectric interface [23]. The mode-field distribution at a few OT resonant frequencies is shown in Fig. 4.3 which depicts that the field localization at different resonant frequencies is spatially separated. The mode-field at the smallest resonant frequency $\nu_{r1} = 172\ THz$ resembles a conventional OT mode whereas the higher frequency modes (such as the ones at $\nu_{r2} = 194.1\ THz$, $\nu_{r3} = 202.3\ THz$, $\nu_{r4} = 222.6\ THz$, etc.) are localized progressively away from the Au-TiO_2 interface (along $+z$ direction).
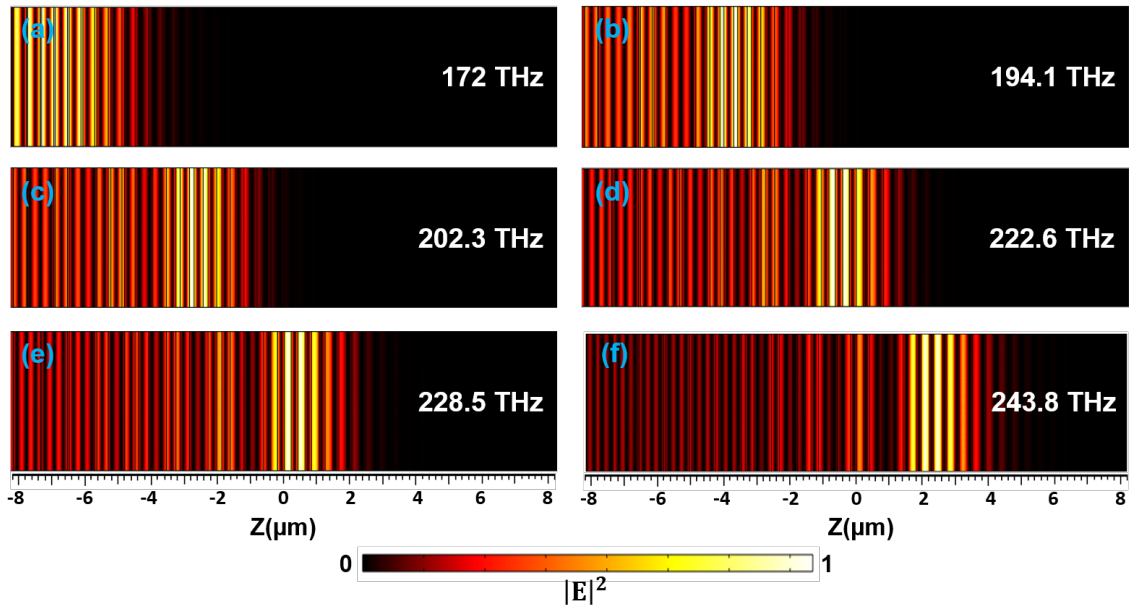
Figure 4.3: Normalized mode-field intensity distribution ($\propto |E|^2$) for different OT modes (see Fig. 4.2a) in Au-CPC geometry.

For the geometry under investigation, we obtain 11 sharp OT resonances within the
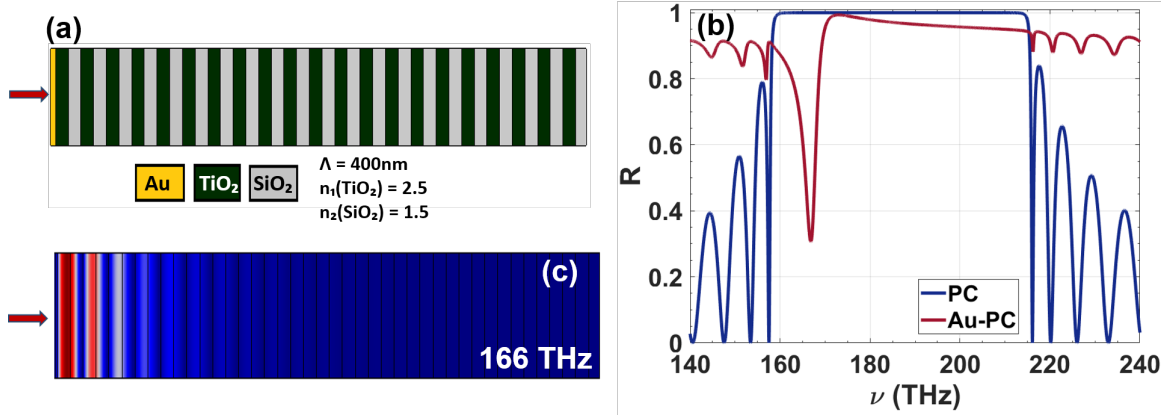
Figure 4.4: a) A schematic of the normal PC. b) The reflection spectrum of normal PC (solid blue line) and Au-PC (red line). c) Normalized mode-field intensity distribution ($\propto |E|^2$) for OT mode resonance in normal PC.

PBG. In order to make a comparison of OT mode excitation in CPC and normal PC, we have considered a normal PC with periodicity $\Lambda = 400nm$ and placed a thin gold layer ($\approx 30nm$) adjacent to the high index layer (TiO_2) as shown in Fig.4.4(a). The resulting reflection spectrum of the PC without metal and with metal is shown by blue and red lines respectively (Fig.4.4(b)). So, the conventional PC leads to the excitation of only one OT mode, the mode field intensity is strongly localized at the metal-dielectric interface and decays away from the interface as shown in Fig.4.4(c).

The origin of OT resonance is governed by the condition that $\phi_{PC} + \phi_M = 2m\pi$ for $m = 0, 1, 2, 3, ...$ where ϕ_{PC} and ϕ_M are the phase acquired by the reflected beam from a semi-infinite PC and metal respectively [22]. It is worth noting that ϕ_M, in general, is negative for visible to the mid-IR spectral band. On the other hand, the sign of ϕ_{PC} (in the PBG) exhibits a *topological* connection [22]. In fact, the sign of ϕ_{PC} (for a certain PBG) is dictated by the algebraic sum of the topological (*Zak*) phase for all the pass (transmission) bands below that PBG. Only those PBGs for which ϕ_{PC} is positive could support OT modes. In Fig. 4.2(b), we observed that the CPC could be decomposed into multiple periodic PCs (with different d_1, d_2) and their overlapping PBGs result in a broader PBG for

the CPC. Within the PBGs of these PCs, ϕ_{PC} traverses from $[0 \rightarrow \pi]$ (anti-clockwise) or $[0 \rightarrow -\pi]$ (clockwise). From a topological perspective, PBGs in the former category only could support OT modes. Periodic PCs constituted using such d_1 and d_2 values could only support OT modes. Consequently, we obtain field localization due to OT mode formation in CPC near certain values of d_1, d_2. The field localization in Fig. 4.3 is in agreement with this argument and the OT mode-field amplitudes exhibit maxima in different unit cells (characterized by different d_1 and d_2).

For the case of CPC, $\phi_{PC} = \gamma + \alpha$, where γ and α are the geometric and dynamic phases acquired by the reflected beam respectively. For a conventional 1D PC, the geometric phase of a transmission band is quantized *i.e.* it can take value either *0* or π and is known as the 'Zak' phase. In this context, the geometric interpretation of the reflection phase is trivial. In the case of CPC, different spectral components within the PBG reflects from different unit cells along the propagation direction as shown in Fig.4.3. Also, the state-vector $\vec{S}$ goes from [0,0,-1] to [0,0,1] for all the frequencies within the PBG by virtue of satisfying the adiabatic-following constraints or we can say that the $\vec{B}$ goes from $[0, 0, -\Delta k]$ to $[0, 0, \Delta k]$ in the parameter space as discussed in *section3.6.3* of *chapter 3*. As the $\vec{S}$ adiabatically follows the path of $\vec{B}$, the initial and final values of $\vec{B}$ in parameter space could also yield the geometric phase. It is known that γ is estimated from angle ϕ (subtended by $\vec{B}$ at the origin $\Delta k = \kappa = 0$) through the relation $\gamma = \frac{\phi}{2}$. In that case, the geometric phase for each spectral component within the PBG is $\frac{\pi}{2}$. In order to elucidate this point, we plot $\vec{B}$ at different z in the parameter space for $\nu = 220 THz$ as shown in Fig.4.5. The evolution of $\vec{B}$ in Fig. 4.5(a) yields $\phi = \pi$ and consequently, $\gamma = \frac{\pi}{2}$. In a similar manner, γ for all the frequencies within the PBG would be $\frac{\pi}{2}$ by virtue of adhering to the constraints imposed by adiabatic following. On the contrary, the variation in $\vec{B}$ is plotted as a function of z for $\nu = 280 THz$ which is outside the PBG of CPC (see Fig. 4.5(b)). $\vec{B}(z = 0)$ (black arrow)
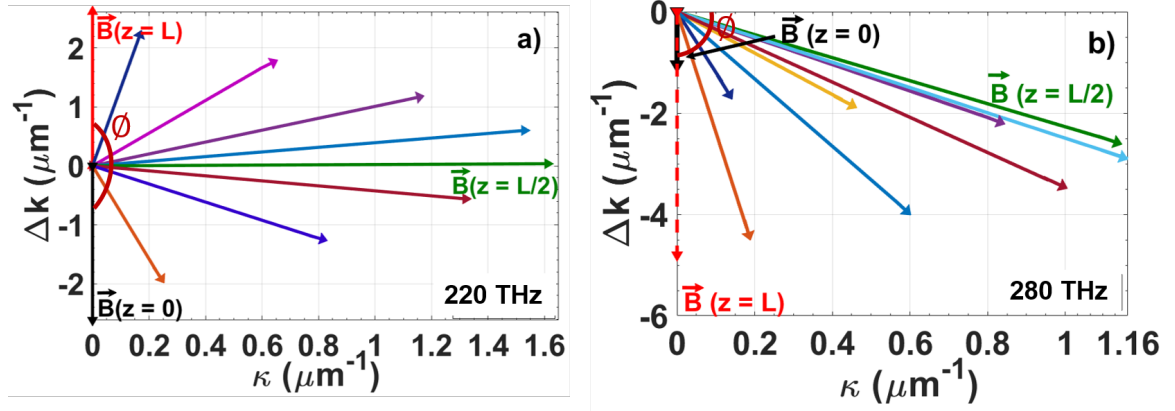
Figure 4.5: Represents the evolution of $\vec{B}$ as a function of length (L) of CPC in parameter ($\Delta k - \kappa$) space for a) $\nu = 220\,THz$ and b) $\nu = 280\,THz$. ϕ represents the angle subtended by curve $\vec{B}$ at the origin.

and $\vec{B}(z = L)$ (red dashed arrow) are co-parallel in this case. Consequently, the geometric phase $\gamma = \frac{\phi}{2} = 0$ for frequencies lying in the pass band. However, the dynamic phase of the reflected beam is estimated through the relation

$$\alpha = \frac{2\pi\nu}{c} \sum_{M=0}^{T} [n_1 d_{1M} + n_2 d_{2M}] \tag{4.1}$$

The knowledge of field localization in the Tth unit cell of CPC would accurately yield the dynamic phase for any frequency (ν). In conjunction with the estimate of γ, this information would allow us to determine the OT mode resonance frequencies.

The em-field localization implies a drop in group velocity (v_g) of OT modes. In order to ascertain v_g, we allow a $100\,fs$ Gaussian pulse centered at different OT resonant frequencies (ν_r in Fig. 4.2(a)) to be incident on the thin Au-layer and perform a finite-difference time-domain (FDTD) simulation to obtain the evolution of the pulse. We used a spatial resolution of $\Delta x = 5nm$, $\Delta y = \Delta z = 10nm$ and a temporal resolution of $\Delta t = 1.34815e^{-5}ps$ in our FDTD simulations. Figure 4.6 shows the result for such a simulation where a comparison is made between a bare CPC and CPC with Au-film (Au-CPC) at two different ν_r. The time (in ps) on the y-axis represents the time of arrival of pulse-peak at the respective locations.
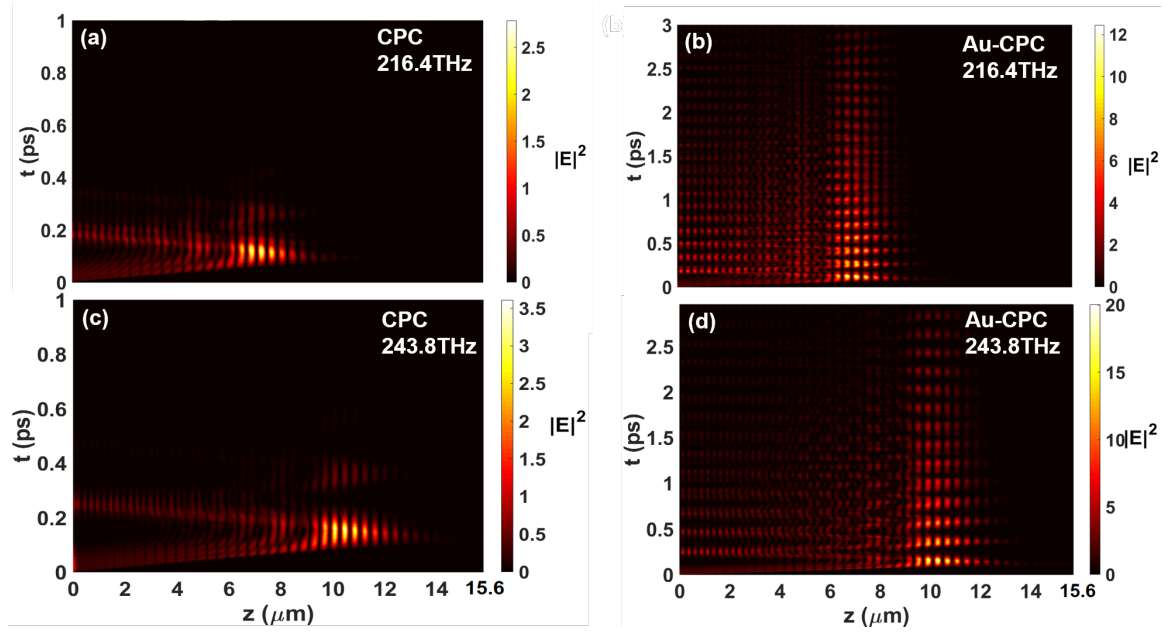
Figure 4.6: a) Shows the simulated mode-field intensity ($\propto |E|^2$) distribution in the time-position plane along propagation (z) direction for a Gaussian pulse with width $100\,fs$ centered at $\nu_r = 216.4\,THz$ propagating through (a) CPC (b) Au-CPC geometry. Similar mode-field intensity distribution at $\nu_r = 243.8\,THz$ in (c) CPC and (b) Au-CPC.

Figures 4.6(a) and (c) show that the electric field intensity of pulses at $\nu_r = 216.4\,THz$ and $\nu_r = 243.8\,THz$ in the bare CPC exhibit short-lived ($\approx\ 0.1 - 0.2\,ps$) localization. This implies, in absence of terminating Au-layer, the frequencies within the PBG reach a certain unit cell of CPC and instantaneously reflect [10]. Identical pulses at the same OT resonant frequencies (in Au-CPC) exhibit localization over a prolonged period ($\geq\ 2\,ps$) as shown in Figs. 4.6(b) and (d). The Au-film creates a resonant cavity for the OT modes and consequently, they exhibit longer lifetimes. The time-domain simulations allow us to directly obtain v_g for each OT mode by noting the time (t) taken by the pulse (peak) to arrive at any point (z) in the CPC (Fig. 4.7(a)). By using this, the variation in v_g for $\nu_r = 243.8\,THz$ along the propagation direction is shown in Fig. 4.7(a). From this figure, it could be ascertained that v_g minimizes near the unit cell with $d_1 = 140\,nm$ and $d_2 = 260\,nm$ which is consistent with the field localization observed in Fig. 4.3 for the same OT resonant fre-
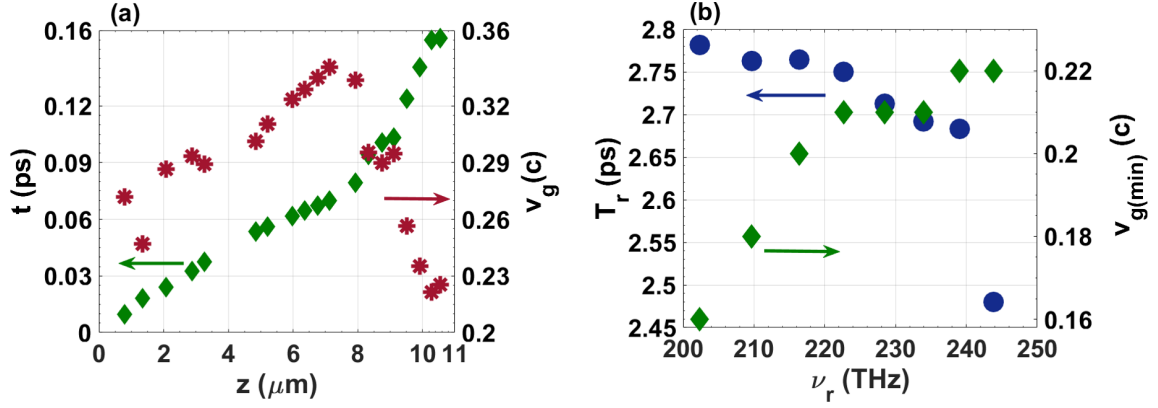
Figure 4.7: shows the time of arrival (green square dots) at any z-coordinate in Au-CPC geometry for a $100\,fs$ Gaussian pulse-peak and variation in v_g (red asterisk-like dots) as a function of z when the pulse central frequency is $\nu_r = 243.8\,THz$. b) shows the trapped-mode lifetime (green square dots) and minimum group velocity $v_{g(min)}$ (blue circular dots) attained by different OT modes in Au-CPC.

quency. The minimum group velocity $(v_{g(min)})$ attained by different OT modes (in Au-CPC) is shown in Fig. 4.7(b). The $v_{g(min)}$ attained by OT mode at $\nu_r = 243.8\,THz$ is $\approx 0.22c$. Figure 4.7(b) shows that $v_{g(min)}$ varies over a range of $\approx 0.05c$ amongst all the OT resonant frequencies with the smallest value of $\approx 0.17c$ at $\nu_r = 202.3\,THz$. The exact values of ν_r, $v_{g(min)}$, and T_r for each OT mode are listed below in the table. The conventional rain-

OT resonant Frequency ν_r (THz)	Minimum group velocity $(v_{g(min)})$ (in units of c)	Trapping time (T_r) (ps)
202.3	0.16	2.782
209.7	0.18	2.763
216.4	0.20	2.764
222.6	0.21	2.750
228.5	0.21	2.713
233.9	0.21	2.692
239.1	0.22	2.683
243.8	0.22	2.480

Table 4.1: Shows the minimum group velocity and trapping time attained by different OT resonances.

bow trapping techniques utilize graded-indexed plasmonic gratings or waveguides which

comprise ingrained absorptive metallic components. Although they dictate the drop in v_g through surface-plasmon excitation, they introduce unavoidable *absorption* loss (α) which puts a restriction on the time for which an optical pulse could be stored. Typically, the trapped-mode lifetime $T_r = \frac{1}{\alpha v_g} \leq 1 \ ps$ for plasmon-based metallo-dielectric architectures. In our case, the Au-layer (plasmon-active metal film) at the terminating CPC layer leads to the excitation of several OT modes. As shown in Fig. 4.3, such modes are primarily localized within the all-dielectric CPC architecture and have a very small presence in the metal layer. Therefore, the dominant source of *loss* in such OT modes (in Au-CPC) is the transmission loss due to the finite length of the photonic crystal. Since different OT modes are spatially separated, they exhibit different transmission losses which could be estimated from the throughput modal power for a particular OT resonant frequency. Alternately, this
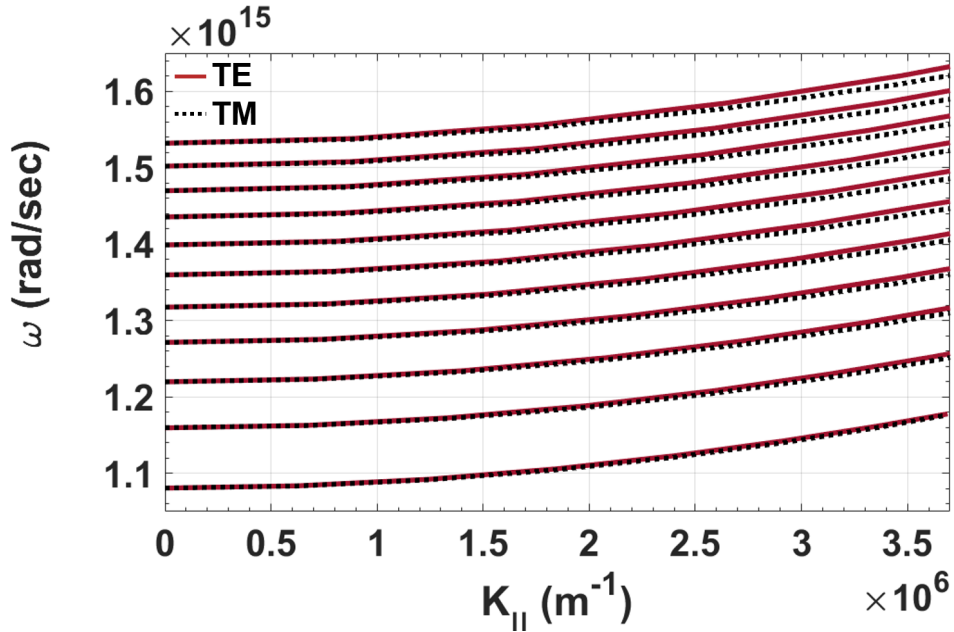
Figure 4.8: Shows the variation of angular frequency as a function of in-plane wavevector ($K_{\parallel}$) for the TE (solid red curve) and TM (dashed black curve) polarized OT modes in Au-CPC.

also provides an estimate of the trapped-mode lifetime (T_r) for different OT modes. From the time-domain simulations in Figs. 4.6(b) and (d), T_r could be determined by monitor-

59

ing the fall in pulse-peak to $1/e^2$-*th* of its maximum value. For example, the OT mode at $\nu_r = 243.8\ THz$ has a trapped lifetime $T_r \approx 2.48\ ps$. Due to different $v_{g(min)}$ for different OT modes, the trapped lifetime for OT modes varies which is shown in Fig.4.7(b). T_r maximizes to $2.78\ ps$ at $\nu_r = 202.3\ THz$ and varies by about $0.35\ ps$ across the frequency tunable range. It is also apparent that the OT modes localized closer to the Au layer exhibit longer trapped lifetimes which is essentially a consequence of smaller transmission losses.

The dispersion characteristics of such resonant frequencies are shown in Fig. 4.8 where $K_{\parallel}$ represents the in-plane (or tangential) component of the wavevector. All the OT modes exhibit a parabolic dispersion curve and the polarization degeneracy is lifted for higher values of the in-plane component of the wavevector. This behavior is similar to conventional OT modes localized at the metal-dielectric interface. The low energy OT modes exhibit a small splitting between TE and TM polarizations at higher $K_{\parallel}$ values. The splitting tends to increase for high-frequency OT modes due to appreciable redistribution of the TE/TM polarized mode fields.

4.4   Experimental results

In order to realize the existence of multiple optical Tamm-like modes, we have fabricated two CPC with different numbers of unit cells *i.e.* for N=22 and for N=31. The CPC consists of alternating layers of TiO_2 and SiO_2 with refractive index n_1 and n_2 respectively with a constant period of $\Lambda = 400\ nm$ (see Fig. 4.1). However, the duty cycle of each unit cell varies by $\delta = 10\ nm$. The CPC terminates with the TiO_2 (high index). In order to excite OT modes, we have deposited a thin Au layer of thickness $d_{Au} = 10\ nm$ adjacent to the TiO_2 layer as shown in Fig. 4.1. In order to obtain the reflection spectrum, we used a supercontinuum source generating coherent broadband spectrum from $\approx 400\ nm$ to $\approx 2200\ nm$ and the broadband beam is incident normally on the fabricated multilayer
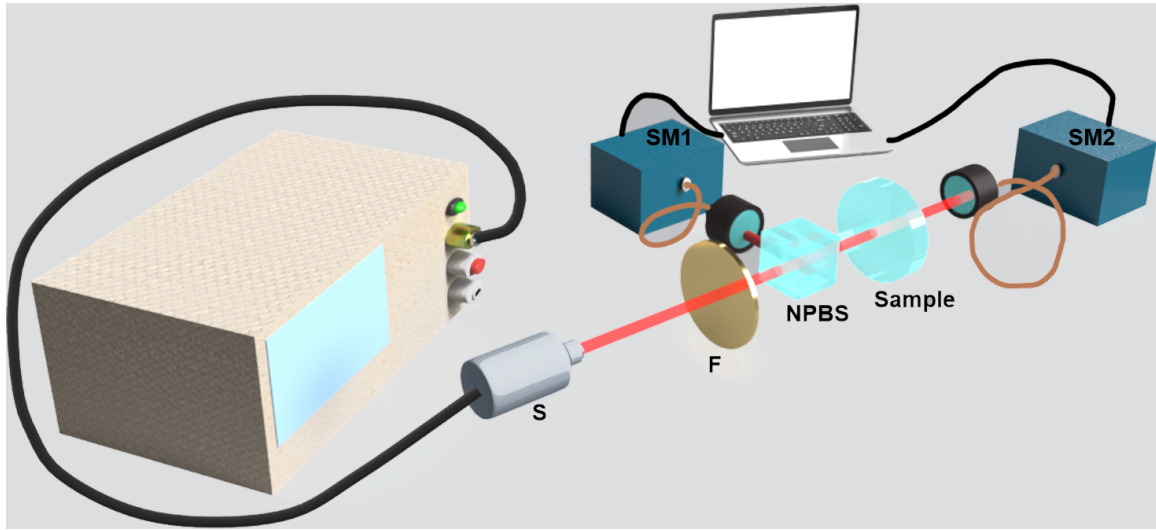
Figure 4.9: Shows the experimental setup for measuring the reflection and transmission spectrum; s: source; F: Filter; NPBS:non-polarizing beam splitter; SM1, SM2:spectrometers.

geometry. The reflection as well as the transmission spectrum was measured using an experimental setup presented in Fig. 4.9. A neutral-density (ND) filter was employed for controlling the light being incident on the CPC as well as Au-CPC geometry. Two spectrometers SM1 and SM2 were used to collect the reflected and transmitted light from the multilayer films respectively. The reflected beam was delivered to the spectrometer (SM1) using a $50 : 50$ beam splitter. The diameter of the light beam incident on the sample is $\approx 3mm$ and CPC cross-sectional area is $\approx 12\ mm$. The measured reflection spectrum was normalized with a reflection standard (RS-2, M/S Avantes Inc., Netherlands) in order to account for the non-uniform spectrum of the supercontinuum source. Figures 4.10 (a) and (b) show the measured reflection and transmission spectrum for CPC with $N = 31$ and $N = 22$ respectively. The black curve shows the reflection spectrum for bare CPC and the reflection spectrum for Au-CPC is presented by the maroon curve, which exhibits multiple sharp reflectivity minima within the PBG of CPC. The PBG of CPC extends from $\approx 1150 - 1600\ nm$ which is obtained from the transmission spectrum (represented by green
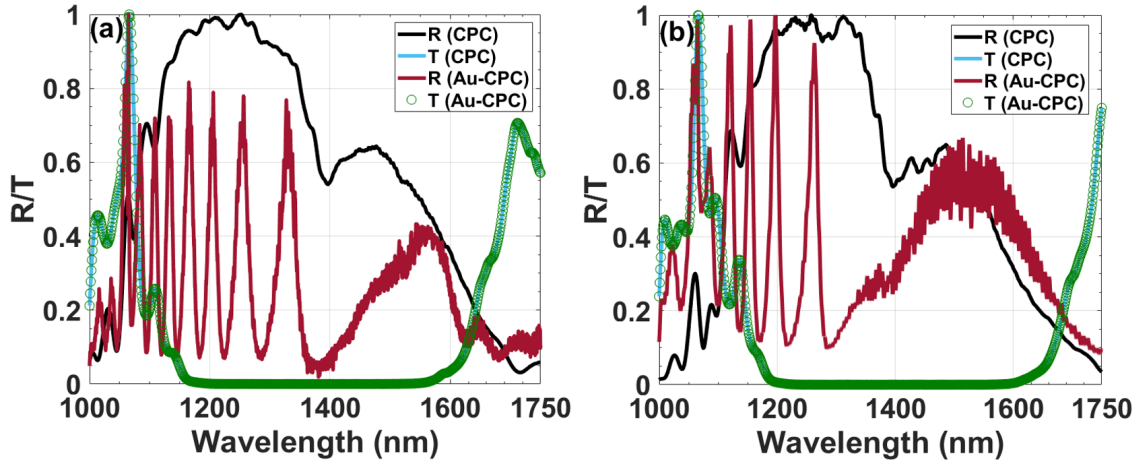
Figure 4.10: Reflection spectrum for CPC (AU-CPC) is shown by the black (maroon) line. Green circles show the transmission spectrum for CPC and Au-CPC (a) for N = 31 unit cells and (b) for N = 22 unit cells.

circles).

Such sharp resonances within the PBG corresponds to the OT modes in metallo-dielectric geometries. For $N = 31$ unit cells, the AU-CPC exhibits 5 distinct OT resonances within the PBG of CPC (see Fig. 4.10(a)). Multiple excitations of OT modes are essentially a consequence of multiple phase jumps ($= \pi$) within the PBG suffered by the backscattered beam. This allows for satisfying the OT resonance condition at multiple frequencies within the PBG. It is worth noting that the OT resonances reduce to 3 for CPC with unit cells $N = 22$ (see Fig. 4.10). This drop is essentially brought about by a smaller PBG in the case of CPC with $N = 22$ unit cells.

4.5 Conclusion

In conclusion, we presented an optimally-designed CPC which closely follows the adiabatic constraints and consequently, manifests into PBG broadening and multiple π-jumps in the backscattered phase. This allows the excitation of multiple sharp OT mode resonances in the case of Au-CPC configuration. All the OT modes are spatially separated in the CPC and

exhibit a topological connection. These OT mode resonances provide a favorable platform for low-loss trapping of light with lifetimes as large as $\geq 2.8\ ps$. In addition to this, we have also verified experimentally that the Au-CPC-like architectures support multiple optical Tamm-like modes.

References

[1] Yun Shen, Hailin Liu, Jiwu Fu, and Guoping Yu. Double rainbow trapping of light in one-dimensional chirped metallic–dielectric photonic crystals. *J. Opt. Soc. Am. B*, 28(10):2444–2447, Oct 2011.

[2] Zhixia Xu, Jun Shi, Robert J. Davis, Xiaoxing Yin, and Daniel F. Sievenpiper. Rainbow trapping with long oscillation lifetimes in gradient magnetoinductive metasurfaces. *Phys. Rev. Applied*, 12:024043, Aug 2019.

[3] Toshihiko Baba. Slow light in photonic crystals. *Nature Photonics*, 2:465–473, 08 2008.

[4] Qiaoqiang Gan, Yujie J. Ding, and Filbert J. Bartoli. "rainbow" trapping and releasing at telecommunication wavelengths. *Phys. Rev. Lett.*, 102:056801, Feb 2009.

[5] Lin Chen, Guo Ping Wang, Qiaoqiang Gan, and Filbert J. Bartoli. Trapping of surface-plasmon polaritons in a graded bragg structure: Frequency-dependent spatially separated localization of the visible spectrum modes. *Phys. Rev. B*, 80:161106, Oct 2009.

[6] L. Chen, G. P. Wang, X. Li, W. Li, Y. Shen, and S. Lai, J.and Chen. Broadband slow-light in graded-grating-loaded plasmonic waveguides at telecom frequencies. *Applied Physics B*, 104(3):653–657, Sep 2011.

[7] Qiaoqiang Gan, Yongkang Gao, Kyle Wagner, Dmitri Vezenov, Yujie J. Ding, and

Filbert J. Bartoli. Experimental verification of the rainbow trapping effect in adiabatic plasmonic gratings. *Proceedings of the National Academy of Sciences*, 108(13):5169–5173, 2011.

[8] Jie Xu, Qian Shen, Kai Yuan, Xiaohua Deng, Yun Shen, Hang Zhang, Chiaho Wu, Sanshui Xiao, and Linfang Shen. Trapping and releasing bidirectional rainbow at terahertz frequencies. *Optics Communications*, 473:125999, 04 2020.

[9] Sayed Elshahat and Cuicui Lu. Bidirectional rainbow trapping in 1-d chirped topological photonic crystal. *Frontiers in Physics*, 10:Article 831203, 02 2022.

[10] Yun Shen, Jiwu Fu, and Guoping Yu. Rainbow trapping in one-dimensional chirped photonic crystals composed of alternating dielectric slabs. *Physics Letters A*, 375(43):3801–3803, 2011.

[11] Peyman Ghaderian and Amir Habibzadeh-Sharif. Rainbow trapping and releasing in graded Bragg grating graphene plasmonic waveguide. *Optics Express*, 29:3996–4009, 01 2021.

[12] M. Kaliteevski, I. Iorsh, S. Brand, R. A. Abram, J. M. Chamberlain, A. V. Kavokin, and I. A. Shelykh. Tamm plasmon-polaritons: Possible electromagnetic states at the interface of a metal and a dielectric Bragg mirror. *Phys. Rev. B*, 76:165415, Oct 2007.

[13] A. P. Vinogradov, A. V. Dorofeenko, S. G. Erokhin, M. Inoue, A. A. Lisyansky, A. M. Merzlikin, and A. B. Granovsky. Surface state peculiarities in one-dimensional photonic crystal interfaces. *Phys. Rev. B*, 74:045128, Jul 2006.

[14] Yikai Chen, Douguo Zhang, Liangfu Zhu, Ruxue Wang, Pei Wang, Hai Ming, Ramachandram Badugu, and Joseph R. Lakowicz. Tamm plasmon- and surface plasmon-

coupled emission from hybrid plasmonic-photonic structures. *Optica*, 1(6):407–413, Dec 2014.

[15] Baptiste Auguie and Alejandro Fainstein. Critical coupling to tamm plasmons. *Journal of Optics*, 17, 11 2014.

[16] Lina Maigyte and Kestutis Staliunas. Spatial filtering with photonic crystals. *Appl. Phys. Rev.*, 2:011102, 02 2015.

[17] Kimura Mitsuteru, Okahara Kazuaki, and Toshihiko Miyamoto. Tunable multilayer-film distributed-Bragg-reflector filter. *J. Appl. Phys.*, 50:1222, 03 1979.

[18] Samir Kumar, Mukesh Shukla, Partha Maji, and Ritwick Das. Self-referenced refractive index sensing with hybrid-tamm-plasmon-polariton modes in sub-wavelength analyte layers. *Journal of Physics D: Applied Physics*, 50, 07 2017.

[19] Boris Afinogenov, A. Popkova, V. Bessonov, B. Lukyanchuk, and Andrey Fedyanin. Phase matching with Tamm plasmons for enhanced second- and third-harmonic generation. *Phys. Rev. B*, 97:115438, 03 2018.

[20] Clementine Symonds, Guillaume Lheureux, Jean Paul Hugonin, Jean Jacques Greffet, Julien Laverdant, Giovanni Brucoli, Aristide Lemaître, P. Senellart, and Joel Bellessa. Confined tamm plasmon lasers. *Nano letters*, 13, 06 2013.

[21] Amnon Yariv and Pochi Yeh. *Optical Waves in Crystals Propagation and Control of Laser Radiation*. New York Wiley, 1984.

[22] Wen Sheng Gao, Meng Xiao, C. T. Chan, and Wing Yim Tam. Determination of zak phase by reflection phase in 1d photonic crystals. *Opt. Lett.*, 40(22):5259–5262, Nov 2015.

[23] Mukesh Kumar Shukla and Ritwick Das. Tamm-plasmon polaritons in one-dimensional photonic quasi-crystals. *Opt. Lett.*, 43(3):362–365, Feb 2018.

Chapter 5

Optical beam shaping using one-dimensional photonic crystals

5.1   Introduction

Electromagnetic waves essentially possess multiple degrees of freedom namely frequency or wavelength, polarization, amplitude, and spatial extent. Through a strong interaction between polarization and spatial degrees of freedom, unique spatial configurations have been generated which represent different forms of singularities. Over a period of last two decades, such spatially structured beams have attracted significant attention owing to their wide spectrum of applications in particle trapping, particle guiding [1], free-space optical communication[2, 3], optical tweezers[4, 5], super-resolution imaging[6, 7], quantum information processing [8]. In order to generate beams with unique spatial variations, orthogonally polarized laser beams interact with each other's spatial counterparts through an artificially structured medium which could be liquid crystal-based phase-retarders/modulators or optimally-designed metasurface gratings [9, 10]. This could also be achieved by sharply focusing a beam with an inhomogeneous wavefront [11, 12]. In structured light beams, the phase varies across the spatial extent of the wavefront and an interesting situation appears when the phase exhibits a singularity at $r = 0$ in cylindrical and spherical coordinates. Such beams are characterized by a spiraling wavefront and are termed as optical vortex beams. A simpler form of the structured optical beam is a Hermite-Gaussian (HG_{mn}) beam where m and n represent the *zeroes* in beam-wavefront along x-direction and y-direction respectively. Alternately, the spatial variation of an HG_{mn} beam follows a variation resembling

a *Hermite*-polynomial of mth-order in x-direction and n^{th}-order in the y-direction. Conventionally, the generation of structured Gaussian beams such as HG beams of any order (any m or n) is carried out by interference of different Gaussian beams with optimum phase differences on the observation plane. In order to create an optimum phase difference, a straightforward route is to manipulate the *dynamic phase* for the interfering beams through propagation in a high-index dispersive medium or in an optimally designed cavity that scales up the optical path length or a hybrid strategy involving the aforementioned possibilities [1, 13]. A plausible alternative route is to manipulate the *geometric phase* acquired by the interfering beams through an optimally designed interferometric configuration. The *geometric phase*, alternately known as *Pancharatnam-Berry (PB) phase* is acquired by a light beam when one or more dynamic variables change during the propagation of light through the medium. In the optical domain, such dynamic variables include propagation constant and coupling strength between the associated degrees of freedom. The spiral phase-plates (or q-plates), holograms, and liquid crystal-based spatial light modulators, etc. are examples of such devices [14, 9, 15]. By exploiting the winding topology in the bandstructure for a two-dimensional photonic crystal slab, the geometric-phase assisted beam restructuring has been recently demonstrated [16]. Interestingly, the geometric phase (ϕ_g) acquired by a propagating mode in a 1D PC is *quantized i.e.* $\phi_g = 0$ or $\phi_g = \pi$). This quantized geometric phase is also termed as the *topological phase* or *Zak* phase [17, 18]. It is important to note that the *Zak* phase (ZP), through the bulk-boundary correspondence, determines the reflection phase for a forbidden band of a photonic crystal [19, 20]. This relationship has been employed for exciting the topologically-protected optical edge modes which facilitate the development of robust disorder-resistant optical configurations such as optical sensors, frequency converters, slow-light devices, spontaneous emission inhibitors, and photovoltaic devices [21, 22, 23]. The strong field localization at a PC-plasmonic material interface facilitates coherent and directional emission from quantum emitters in TE

as well as TM polarizations [24]. Such schemes have been extensively employed using 1D PC for a broad range of applications involving wavelength-selective filters, bandpass filters, and optical waveguides [25, 26]. It is worth noting that the primary focus of all such investigations in 1D PCs involves tailoring the spectral characteristics of the propagating or localized (surface) modes existing at the metal-dielectric interface. In a recent investigation, A. Karnieli *et al.* showed that the geometric phase acquired by a conjugate pair of nonlinear frequency-converted beams could be employed for generating HG beams located in a widely separated spectral band [27]. In the present work, we show that the topological phase associated with a photonic pass (transmission) band of 1D PC has the potential to generate spatially structured beams such as the HG beam in the reflection as well as transmission geometry.

5.2   Analytical framework and Design principle

We consider a 1D PC (PC) with periodically-stacked alternating layers of two different dielectric materials having refractive indices n_a and n_b with thicknesses d_a and d_b as shown in Fig. 5.1(a). The unit cell length is given by $\Lambda = d_a + d_b$. A measure of the bandstructure could be ascertained from the simulated reflection spectrum for the PC depicted by the maroon-colored curve in Fig. 5.2(a) which is characterized by 4 high-reflectivity spectral bands, namely BG_n ($n = 1, 2, 3, 4$) are separated from each other by '$max(n) + 1$' (or 5) high-transmission bands. The simulation considers $N = 20$ unit cells of periodic multilayers of SiO_2 (n_a) and TiO_2 (n_b) with arbitrarily chosen thicknesses $d_a = 420 \ nm$ and $d_b = 190 \ nm$ respectively. The sign of the phase acquired by the reflected beam (for frequencies within BG_1, BG_2, BG_3 or BG_4) is dictated by the topological phase or ZP (θ_n^{Zak}) of the transmission band(s) situated at wavelengths longer than the corresponding

PBG [19]. In accordance with the above description, the PC contains '$max(n) + 1$' high-transmission bands and the reflection phase for frequencies within the nth bandgap BG_n (*i.e.* Φ_n) is the sum of *ZP* for all the transmission bands from 0 to $(n-1)$. Quantitatively this is expressed as,

$$sgn(\Phi_n) = (-1)^n exp(i\sum_{m=0}^{n-1} \theta_m^{Zak}) \tag{5.1}$$

where Φ_n is the phase of the reflected wave (beam) from the nth PBG. It is important to note that the *ZP* for a band n (θ_m^{Zak}) is obtained by integrating the Berry's connection over the entire Brillouin-zone *i.e.*

$$\theta_m^{Zak} = \int_{-\pi/\Lambda}^{\pi/\Lambda}[i \int_{unit\ cell} n_r^2(z)\psi_{m,K}^*(z)\frac{\partial}{\partial K}\psi_{m,K}(z)dz]dK$$

where $\psi_{m,K}$ is the Bloch eigenfunction for the Bloch wavevector K and n_r is the refractive index function varying along z [19]. Due to the cyclic nature of Bloch eigenfunctions, θ_m^{Zak} takes binary values *i.e.* 0 or π. In order to derive (5.1), we assume that (a) the origin is located at the center of layer a in a unit cell (b) PBG does not close at Brillouin zone boundary [19]. In absence of any permeability in the dielectric medium *i.e.* $\mu = \mu_0$, the ZP of lowest transmission band ($n = 0$) is given by [19],

$$exp(i\theta_0^{Zak}) = sgn\left[1 - \frac{n_a^2}{n_b^2}\right] \tag{5.2}$$

A simpler route to obtain the ZP for $n > 0$ transmission bands is to ascertain the wavelength (λ) within the transmission band which satisfies the condition

$$\sin\left(\frac{2\pi n_b d_b}{\lambda}\right) = 0 \tag{5.3}$$

If a wavelength (or frequency) within a transmission band (n) satisfies (5.3), $\theta_n^{Zak} = \pi$, otherwise $\theta_n^{Zak} = 0$ [19]. Using (5.1), (5.2) and (5.3), the phase acquired by the reflected beam, as well as the geometric phase acquired by the transmitted beam in a 1D PC, could be ascertained. With respect to Fig. 5.1(a), the $\theta_0^{Zak} = \pi$, $\theta_1^{Zak} = \pi$, $\theta_2^{Zak} = 0$ and $\theta_3^{Zak} = \pi$.
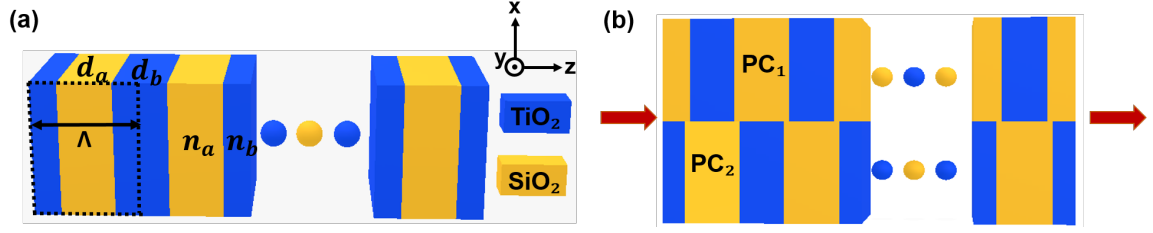
Figure 5.1: a) Shows a schematic of 1D PC (b) shows a schematic of the composite PC with PC_1 and PC_2 being placed adjacent to each other.

It is worth reiterating the point that the aforementioned inferences are true only if any unit cell of the 1D PC exhibits mirror reflection symmetry about the center of layer a. In other words, if the choice of origin is such that the 1D PC exhibits a mirror reflection symmetry about the center of layer b then θ_n^{Zak} would change without affecting the spectral positions of bandgaps and transmission bands.

5.3 Computational Results

The aforementioned observation motivates us to investigate the transmission (and reflection) properties of two 1D PCs placed adjacent to each other (along x-direction) as shown in Fig. 5.1(b). The PC_1 is identical to that shown in Fig. 5.1(a) and PC_2 has identical values of d_a and d_b (as well as $n_a = 2.5$ and $n_b = 1.5$) but translated by a factor of $\frac{\Lambda}{2}$ along the propagation (z) direction. Both PC_1 and PC_2 contain an identical number of unit cells as well. This essentially results in identical PBGs for PC_1 and PC_2 but the Zak phase of transmission bands are interchanged. In other words, $\theta_0^{Zak} = 0$ for PC_1 and $\theta_0^{Zak} = \pi$ for PC_2. Consequent upon this, two beams (at the same wavelength) propagating separately through PC_1 and PC_2 would acquire a phase difference of π which is essentially the difference of Zak phase for the respective transmission band in that 1D PC. The ZP for all the transmission bands is mentioned in Table 5.1. This arrangement also ensures that the difference between the reflection phase for any wavelength (or frequency) situated in BG_1 or BG_3 of
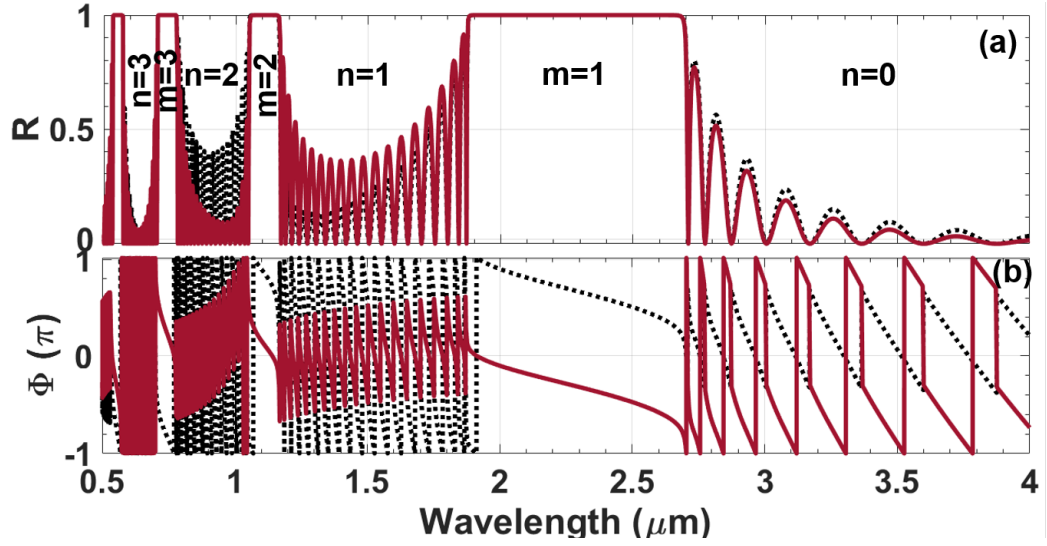
Figure 5.2: (a) Reflection spectrum and (b) reflection phase for PC_1 (solid curve) and PC_2 (dashed curve).

PC_1 **(maroon line)**	PC_2 **(black line)**
$\theta_0^{Zak} = 0$	$\theta_0^{Zak} = \pi$
$\theta_1^{Zak} = 0$	$\theta_1^{Zak} = \pi$
$\theta_2^{Zak} = \pi$	$\theta_2^{Zak} = 0$
$\theta_3^{Zak} = 0$	$\theta_3^{Zak} = \pi$

Table 5.1: Shows the zak phase (θ^{Zak}) of the transmission bands for PC_1 and PC_2.
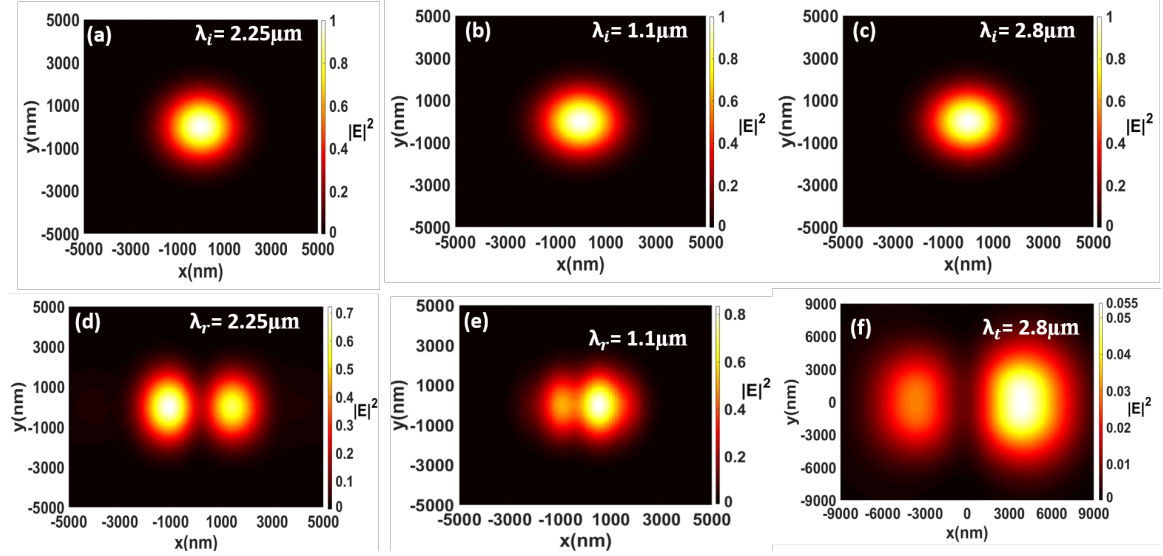
Figure 5.3: Shows the simulated mode-field intensity ($\propto |E|^2$) distribution (or beam profile) for incident Gaussian beam at wavelengths (a) $\lambda = 2.25\ \mu m$, (b) $\lambda = 1.1\ \mu m$ and (c) $\lambda = 2.8\ \mu m$ (d) and (e) represent the intensity distribution for the reflected beam at $\lambda = 2.25\ \mu m$ and $\lambda = 1.1\ \mu m$ respectively (f) mode-field intensity distribution for the transmitted beam at wavelength $\lambda = 2.8\ \mu m$.

PC_1 and PC_2 would be π. This point is elucidated in Fig.5.2(b) where the reflection phase in BG_1 and BG_3 exhibit a similar spectral variation but differ by a factor of π with respect to each other. In general terms, it could be inferred that all the PBG with odd m (order) would exhibit this feature for any two 1D PCs described in Fig. 5.1(b). With regard to this observation, the incidence of Gaussian wavefront which is symmetric about $x = 0$ in the $x-y$ plane (see Fig. 5.1(b)) at any frequency within the BG_1 or BG_3 (in Fig. 5.2(a)) would lead to a symmetric *two-lobed* beam. This would be essentially due to interference of reflected wavefronts from PC_1 and PC_2 that have a phase difference of π. On the other hand, the phase-difference between reflected beams for wavelengths in BG_2 and BG_4 would be $< \pi$, and consequently, the interference between two reflected beams would result in an asymmetric *two-lobed* beam. In order to illustrate this point, we have performed FDTD simulations in 3D using commercial Ansys Lumerical software. The FDTD modeling considers a composite geometry shown in Fig. 5.1(b) with 20 unit cells in PC_1 as well as in

73

PC_2. The simulation domain is a $20 \times 20 \times 20 \ \mu m^3$ volume which contains discreet grids of dimension $\leq 50 \ nm$ for achieving desirable convergence. A Gaussian pulsed beam with a pulse-width of $0.1 \ ns$ is incident on the composite geometry in Fig. 5.1(b). In order to obtain the mode-field intensity distribution, perfectly-matched layer (PML) boundary conditions are imposed along x, y, and z directions. The incident and simulated mode-field distributions at three different wavelengths are shown in Fig. 5.3. Figs. 5.3(a-c) represent the incident symmetric Gaussian beam on the geometry shown in Fig. 5.1(b) at wavelengths $\lambda = 2.25 \ \mu m$ (within BG_1), $\lambda = 1.1 \ \mu m$ (within BG_2) and $\lambda = 2.80 \ \mu m$ (in the transmission band $n = 0$). Figures 5.3(d) and (e) show the mode-field distribution of the reflected beam which distinctly shows the appearance of a zero (minima) between two bright lobes. The conversion to HG_{10} mode is brought about by the phase difference accumulated by the beams reflected from PC_1 and PC_2. As discussed before, there exists an asymmetry in the field distribution in Fig. 5.3(e) which is mainly due to the fact that the phase-difference is $< \pi$ between the reflected beams situated in BG_2 of the reflection spectrum (see Fig. 5.2(a)). Figure 5.3(f) shows the transmitted beam at $\lambda = 2.80 \ \mu m$ which also exhibits an asymmetric two-lobed HG_{10}-like field distribution. This essentially happens due to the difference of π between the 'Zak'-phases ($\theta_0^Z ak$) of PC_1 and PC_2 for $n = 0$ transmission band. The asymmetry, in this case, is essentially due to the small difference in the absolute value of transmittance in PC_1 and PC_2 at $\lambda = 2.80 \ \mu m$. In the next case, we consider a

PC_1 **(maroon line)**	PC_2 **(black line)**
$\theta_0^{Zak} = \pi$	$\theta_0^{Zak} = \pi$
$\theta_1^{Zak} = \pi$	$\theta_1^{Zak} = \pi$
$\theta_2^{Zak} = 0$	$\theta_2^{Zak} = 0$
$\theta_3^{Zak} = \pi$	$\theta_3^{Zak} = \pi$

Table 5.2: Shows the zak phase (θ^{Zak}) of the transmission bands for PC_1 with $n_a = 2.5$ and $n_b = 1.5$ and PC_2 with $n_a = 2.6$ and $n_b = 1.4$.

situation where the Zak-phase for the corresponding transmission (or pass) bands in PC_1
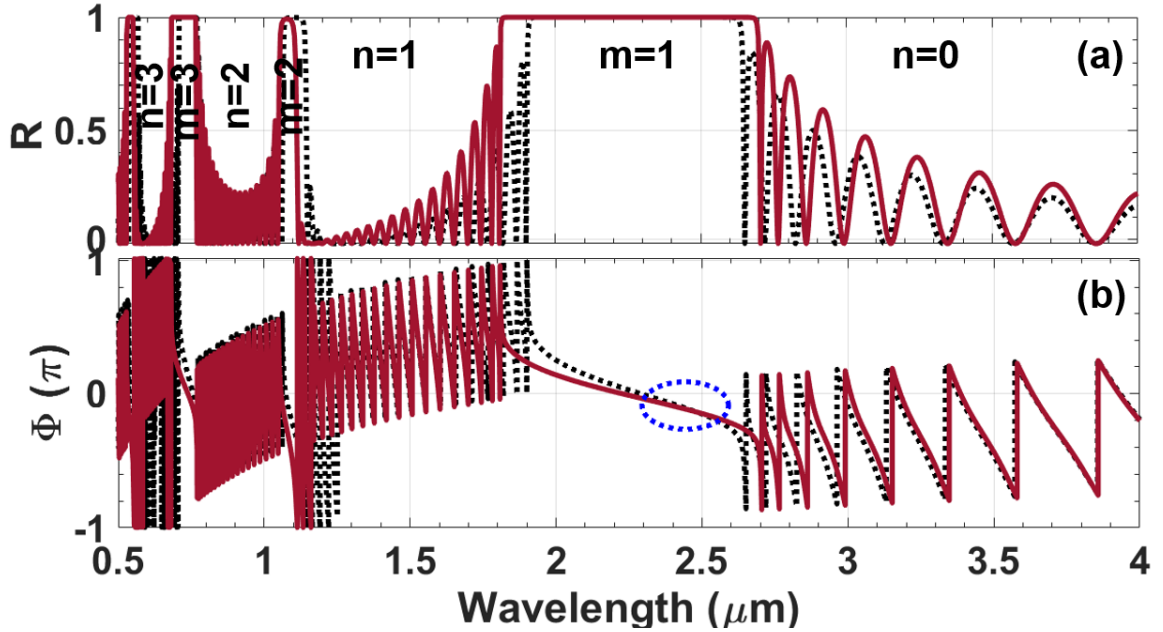
Figure 5.4: (a) Shows the simulated reflection spectrum and (b) phase of the reflected beam from PC_1 having $n_a = 2.5$, $n_b = 1.5$ (dashed line) and PC_2 with $n_a = 2.6$, $n_b = 1.4$ (solid line) respectively.

and PC_2 are identical as given in Table 5.2. This could be achieved by considering PC_1 with $n_a = 2.5$ and $n_b = 1.5$ and that for PC_2 being $n_a = 2.6$ and $n_b = 1.4$. The layer thicknesses d_a and d_b are the same for PC_1 as well as PC_2. Due to this, the reflection spectrum for PC_1 (dashed line) and PC_2 (solid line) are slightly different which is shown in Fig. 5.4(a). However, they exhibit a significant overlap of PBGs. As a consequence of PC design, the phase (Φ) of the reflected beam (from corresponding PBGs) are very close to each other as shown in Fig. 5.4(b). In a few PBGs, Φ could be the same at one wavelength as shown in Fig. 5.4(b) (encircled region). We consider an arrangement identical to that shown in Fig. 5.1(a) and a Gaussian beam (dimensions same as before) is incident on the configuration. At a wavelength of $\lambda = 3.1\ \mu m$ (in the transmission band $n = 0$), the incident and transmitted mode-field pattern is shown in Fig. 5.5(a) and (b) respectively. Due to identical Zak-phase of lowest ($n = 0$) transmission band for both PC_1 and PC_2, the mode-field profiles corresponding to the incident or the transmitted beam remain the same.

75
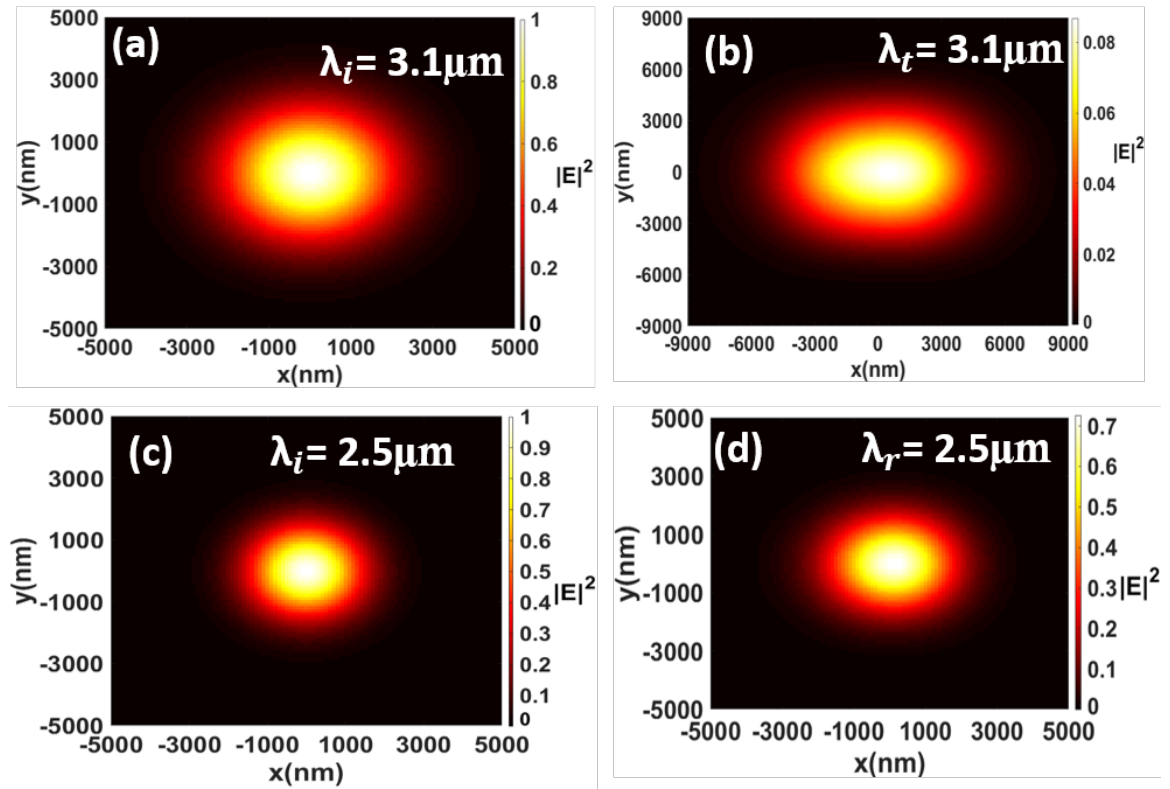
Figure 5.5: Shows the simulated mode-field intensity distribution for the composite PC geometry presented in Fig. 5.1(b) for (a) incident beam at $\lambda = 3.1~\mu m$ (b) transmitted beam at $\lambda = 3.1~\mu m$ (c) incident beam $\lambda = 2.5~\mu m$ and (d) reflected beam respectively at $\lambda = 2.5~\mu m$.
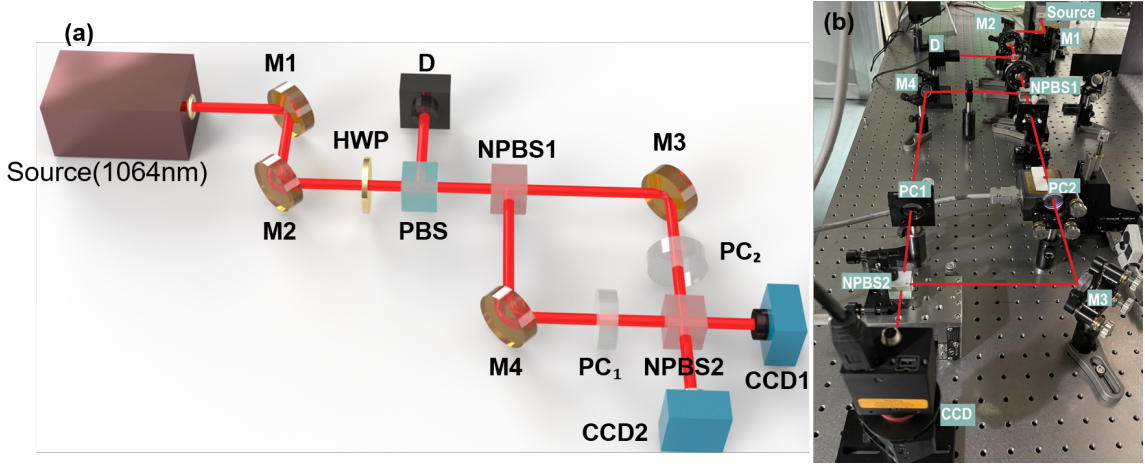
Figure 5.6: (a) Schematic of the experimental set-up for Machzehnder interferometer; M1,M2: alignment mirrors, M3,M4:steering mirrors; HWP: half-wave-plate; PBS: polarizing beam splitter; NPBS1,NPBS2: non-polarizing beam splitter; CCD1, CCD2: camera;D: photodetector. (b) Image of the experimental arrangement in the laboratory.

Further, for the reflected beam at $\lambda = 2.5\ \mu m$ (where the reflection phases intersect in Fig. 4(b)), the beam profile mimics the incident beam as shown in 5.5(c) and (d). The observations made in Figs. 5.3 and 5.5 elucidate the role played by the topological (Zak) phase towards altering the spatial beam profile for propagation in composite PC geometries such as that shown in Fig. 5.1(b).

5.4 Experimental set-up and observations

In order to experimentally realize the aforementioned idea, we set up a Mach-Zehnder interferometer (MZI) shown in Fig.5.6(a) and (b) and carry out the measurements in the visible spectral band. This essentially allows us to employ commercially available and economical dielectric-coated mirrors for the experiment. The optical source (for MZI) is a $1064\ nm\ Nd : YVO_4$ Q-switched diode-pumped-solid-state (DPSS) laser emitting linearly-polarized beam with pulse-width $\Delta\tau \sim 1\ ns$. A combination of a half-wave plate (HWP) and a polarizing beam splitter (PBS) is used for controlling the optical power inci-

dent on MZI. The MZI consists of two $50 : 50$ non-polarizing beam splitters (NPBS1 and NPBS2) and two steering mirrors (M_3 and M_4) as shown in Fig. 5.6. We choose two commercially available mirrors as PC_1 (Laseroptik, Model: 06105UR1) and PC_2(Laseroptik, Model: 13083ke2) on CaF_2 substrates which transmits $\geq 95\%$ of light at $1064\ nm$. PC_1 and PC_2 are of equal thickness and are positioned normally (angle of incidence $= 0°$) in the two arms of MZI (see Fig. 5.6). The CCD cameras (CCD1 and CCD2) record the beams emerging out of NPBS2. Both the mirrors (PC_1 and PC_2) have identical material constituents with different thicknesses of layers. It is worthwhile to mention that the mirror PC_1 exhibits two PBGs ($1350 - 1650\ nm$ and $580 - 660\ nm$) and PC_2 exhibits only one PBG which spans from $700 - 850\ nm$. In order to determine the Zak-phase for the transmission band around $1064\ nm$ wavelength in PC_1, we deposited a thin ($\approx 20\ nm$) silver (Ag) film on the last layer of PC_1 and recorded the reflection spectrum using incoherent broadband optical sources in the visible ($400 - 1000\ nm$) as well as in the infrared ($1250 - 1800\ nm$) spectral band. The recorded reflection spectrum exhibits one reflectivity minimum within each PBG depicting the excitation of a Tamm-plasmon-polariton (TPP) mode. From this, it could be inferred that the phase of the reflected beam (Φ) from both the PBGs (of PC_1) bears a positive sign. Consequently, the ZP for the transmission band around $1064\ nm$ situated in between the two PBGs is π by virtue of the relation $exp(i\theta_n^{Zak}) = -sgn\left(\frac{\Phi_{m-1}}{\Phi_m}\right)$ [19]. The Zak-phase for the transmission band around $1064\ nm$ wavelength in PC_2 is determined through (5.2) and it is estimated to be 0. In this calculation, it is assumed that PC_2 is composed of periodic multilayers of CaF_2/TiO_2 and CaF_2 is the terminating layer. In the absence of PC_1 and PC_2, the recorded beams in CCD1 and CCD2 (using a suitable beam expander) are shown in Fig. 5.7(a) and (b). The complimentary fringe pattern, which is a signature of π phase difference between the interfering beams, ensures a perfect alignment for the configuration. The insertion of PC_1 and PC_2 (as per Fig. 5.6) results in a fringe pattern shown in Fig. 5.7(c) and (d). A comparison between Fig. 5.7(a) and
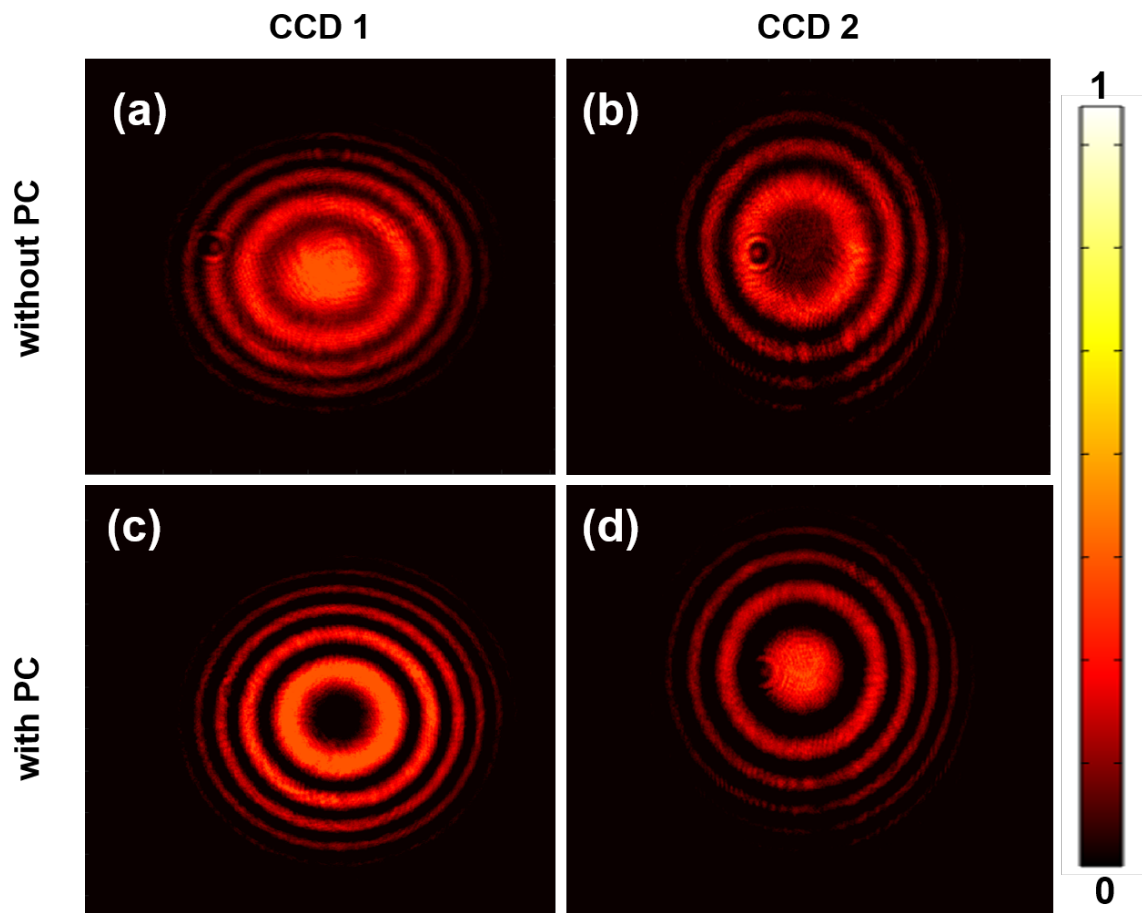
Figure 5.7: (a) and (b) Shows the interference fringe pattern recorded by CCD1 and CCD2 respectively (as per Fig. 5.6) when PC_1 and PC_2 are not present. (c) and (d) represents the interference fringe pattern in the presence of PC_1 and PC_2 as per the description in Fig. 5.6.
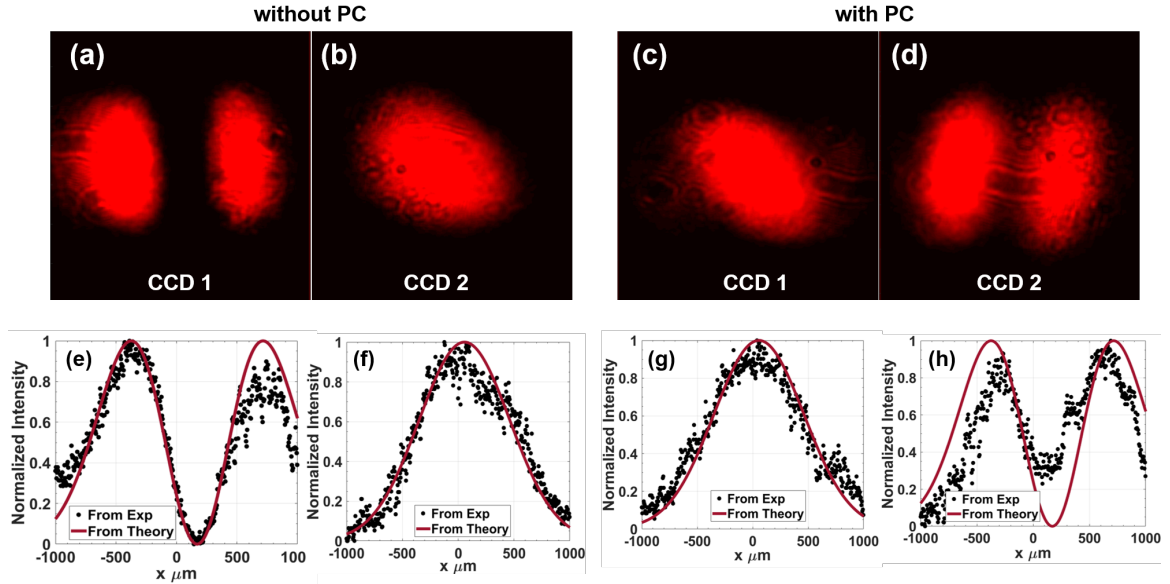
Figure 5.8: Shows the far-field intensity distribution recorded by CCD1 and CCD2 (without beam expander) when a small shear exists between the two interfering beams (a) and (b) represents without PC and c) & d) with PC. e)-h) shows the measured beam profile along x-direction. The solid curves represent the theoretical fitting of a Gaussian and HG_{10} beam

Table 5.3: Shows a comparison between the important features for widely-used techniques (q-plate-based and liquid-crystal based) used for shaping wavefronts and that for the 1D-PC presented here

q-plate	liquid-crystal	1D-Photonic crystal
Polarization-dependent	Polarization-dependent	Polarization-independent
Utilizes anisotropic properties of medium	Could be fabricated using isotropic medium	Could be fabricated using isotropic medium
Vortex beam order depends on the constituent medium	Vortex beam order depends on the constituent medium	Vortex beam order does not depends on the constituent medium
Highly frequency-selective	Works over the moderately narrow spectral band	Works over broad spectral range
Operates at low optical power level (a few mW)	Operates at low to moderate optical power levels (a few tens of mW)	Could be designed for operation at high (Watt-level) optical power
Works in transmission mode	Works in transmission mode	Works in reflection as well as transmission mode

Fig. 5.7(c) shows that the fringe pattern undergoes a phase-shift of π which is essentially brought about by the (geometric) phase difference between the beams propagating in two arms of the MZI. A similar observation could also be made with respect to Fig. 5.7(b) and Fig. 5.7(d). It is worth noting that a $0.5\ mm$ thick etalon (on a rotating stage) is used for compensating the additional dynamic phase and subsequently, improving the contrast between the central ($x = y = 0$) fringe in Figs. 5.7(c) and (d). In the absence of the beam expander, we misalign the interfering beams marginally (in NPBS2) for generating a small *shear*. This would essentially result in a drop in intensity (to 0) in the region where the two beams overlap if the two wavefronts have a π phase difference. On the other hand, the overlapping region would brighten if the interfering wavefronts have a phase difference of 0 or 2π. Figures 5.8(a) and (b) show the recorded beam profiles (without the beam expander) in the absence of PC_1 and PC_2. The observation depicts that the two interfering beams have a phase difference of π which is consistent with the observations in Fig. 5.7(a) and (b). When PC_1 and PC_2 are inserted in the two arms of MZI, the beam profiles are modified which are shown in Fig. 5.8(c) and (d). It is apparent that the beam traveling through the arm containing PC_1 acquires an additional phase of π (equal to the Zak-phase) that leads to a change in the beam-profile *i.e.* CCD2 records a double-lobed beam which resembles an HG_{10} (or HG_{01}) mode and CCD1 records a Gaussian-like beam profile. The ellipticity in the spatial beam profile is due to the small misalignment between the interfering beams. With respect to the center ($x = y = 0$) of the incident Gaussian beam, the recorded beam profile along x-direction (only) is shown in Fig. 5.8(e)-(h) (black dots). A Gaussian function for the Fig. 5.8(f) and (g)) and a *first-order* Hermite polynomial function for Fig. 5.8(e) and (h)) is theoretically fitted to elucidate the beam shaping mechanism using the PC configuration. As predicted in Fig. 5.3(f), there exists a small but discernible asymmetry (with respect to the intensity distribution) in the measured beam profile in Fig. 5.8(d). This is accompanied by a significant (non-zero) value at $x = 0$ which appears as

a consequence of 'non-exact' destructive interference of partially overlapping wavefronts within the NPBS2. The experimental evidence elucidated here provides a basis for generating more complex wavefronts by manipulating the *Zak*-phase via an appropriate 1D-PC design. For example, a PC design with a suitable radial (r) dependence of *Zak*-phase could allow us to generate a vortex beam of a particular order. In Table-5.3, we tabulate the established wavefront-shaping techniques and their important features. The comparison in table-5.3 facilitates the inference that the proposed 1D PC-based beam-shaping technique provides greater flexibility in terms of broader spectral coverage. This method could be employed in high optical-power applications and additionally removes the polarization dependency for the process. In addition, table-5.3 also suggests that the 1D PC-based method partially eases the constraints on the optical medium.

5.5   Conclusions

We presented a plausible route for carrying out beam wavefront-shaping using the topological features of a 1D photonic crystal. The PC design is based on the possibility of acquiring a topological phase (*Zak*-phase) by a transmitted beam through a PC and this allows the wavefront shaping along the transverse ($x - y$) plane. We experimentally observe the generation of HG_{01} (HG_{10}) beams in the reflection as well as transmission mode. The HG_{10} beam exhibit one zero across the transverse plane. The experimental results are consistent with the wavefront shapes obtained using FDTD-based simulations for beam propagation through the designed PC. Within the constraints imposed by material transparency, the scalability of PC geometries to a desirable spectral band provides sufficient flexibility for reshaping optical beams in any desirable wavelength region. Further, this wavefront-shaping scheme is quite robust and disorder-resistant owing to the fact that it is achieved through employing the topological invariants associated with the photonic crystal architecture.

References

[1] Shota Mochizuki, Xiaodong Gu, Kenji Tanabe, Akihiro Matsutani, Moustafa Ahmed, Ahmed H. Bakry, and Fumio Koyama. Generation of vortex beam using bragg reflector waveguide. *Applied Physics Express*, 7:022502, 2014.

[2] A. E. Willner, H. Huang, Y. Yan, Y. Ren, N. Ahmed, G. Xie, C. Bao, L. Li, Y. Cao, Z. Zhao, J. Wang, M. P. J. Lavery, M. Tur, S. Ramachandran, A. F. Molisch, N. Ashrafi, and S. Ashrafi. Optical communications using orbital angular momentum beams. *Adv. Opt. Photon.*, 7(1):66–106, Mar 2015.

[3] Graham Gibson, Johannes Courtial, Miles J. Padgett, Mikhail Vasnetsov, Valeriy Pas'ko, Stephen M. Barnett, and Sonja Franke-Arnold. Free-space information transfer using light beams carrying orbital angular momentum. *Opt. Express*, 12(22):5448–5456, Nov 2004.

[4] L. Paterson, M. P. MacDonald, J. Arlt, W. Sibbett, P. E. Bryant, and K. Dholakia. Controlled rotation of optically trapped microscopic particles. *Science*, 292(5518):912–914, 2001.

[5] Miles Padgett and Richard Bowman. Tweezers with a twist. *Nature Photonics*, 5:343–348, 08 2011.

[6] Mio Yoshida, Yuichi Kozawa, and Shunichi Sato. Subtraction imaging by the combination of higher-order vector beams for enhanced spatial resolution. *Opt. Lett.*, 44(4):883–886, Feb 2019.

[7] Yuichi Kozawa, Daichi Matsunaga, and Shunichi Sato. Superresolution imaging via superoscillation focusing of a radially polarized beam. *Optica*, 5(2):86–92, Feb 2018.

[8] A Mair, A Vaziri, G Weihs, and A Zeilinger. Entanglement of the orbital angular momentum states of photons. *Nature*, 412(6844):313–316, 2001.

[9] Haotong Ma, Haojun Hu, Wenke Xie, and Xiaojun Xu. Study on the generation of a vortex laser beam by using phase-only liquid crystal spatial light modulator. *Optical Engineering*, 52(9):1 – 10, 2013.

[10] Mikhail Shalaev, Jingbo Sun, Alexander Tsukernik, Apra Pandey, Kirill Nikolskiy, and Natalia Litchinitser. High-efficiency all-dielectric metasurfaces for ultra-compact beam manipulation in transmission mode. *Nano letters*, 15, 08 2015.

[11] Shuang-Yin Huang, Guan-Lin Zhang, Qiang Wang, Min Wang, Chenghou Tu, Yong-nan Li, and Hui-Tian Wang. Spin-to-orbital angular momentum conversion via light intensity gradient. *Optica*, 8(9):1231–1236, Sep 2021.

[12] Yiqiong Zhao, J. Scott Edgar, Gavin D. M. Jeffries, David McGloin, and Daniel T. Chiu. Spin-to-orbital angular momentum conversion in a strongly focused optical beam. *Phys. Rev. Lett.*, 99:073901, Aug 2007.

[13] Naresh Sharma, Govind Kumar, Vivek Garg, Rakesh Mote, Vijaya Ramarao, and Shilpi Gupta. Translationally invariant generation of annular beams using thin films. *IEEE Photonics Technology Letters*, PP:1–1, 08 2020.

[14] Pravin Vaity, A. Aadhi, and R. P. Singh. Formation of optical vortices through superposition of two gaussian beams. *Appl. Opt.*, 52(27):6652–6656, Sep 2013.

[15] Victor V. Kotlyar, Anton A. Almazov, Svetlana N. Khonina, Victor A. Soifer, Henna Elfstrom, and Jari Turunen. Generation of phase singularity through diffracting a

plane or gaussian beam by a spiral phase plate. *J. Opt. Soc. Am. A*, 22(5):849–861, May 2005.

[16] Bo Wang, Wenzhe Liu, Maoxiong Zhao, Jiajun Wang, Yiwen Zhang, Ang Chen, Fang Guan, Xiaohan Liu, Lei Shi, and Jian Zi. Generating optical vortex beams by momentum-space polarization vortices centred at bound states in the continuum. *Nature Photonics*, 14:1–6, 10 2020.

[17] J. Zak. Berry's phase for energy bands in solids. *Phys. Rev. Lett.*, 62:2747–2750, Jun 1989.

[18] J. Arkinstall, M. H. Teimourpour, L. Feng, R. El-Ganainy, and H. Schomerus. Topological tight-binding models from nontrivial square roots. *Phys. Rev. B*, 95:165109, Apr 2017.

[19] Meng Xiao, Z. Q. Zhang, and C. T. Chan. Surface impedance and bulk band geometric phases in one-dimensional systems. *Phys. Rev. X*, 4:021017, Apr 2014.

[20] Wensheng Gao, Meng Xiao, Baojie Chen, Edwin Y. B. Pun, C. T. Chan, and Wing Yim Tam. Controlling interface states in 1d photonic crystals by tuning bulk geometric phases. *Opt. Lett.*, 42(8):1500–1503, Apr 2017.

[21] Samir Kumar, Mukesh Shukla, Partha Maji, and Ritwick Das. Self-referenced refractive index sensing with hybrid-tamm-plasmon-polariton modes in sub-wavelength analyte layers. *Journal of Physics D: Applied Physics*, 50, 07 2017.

[22] Boris Afinogenov, A. Popkova, V. Bessonov, B. Lukyanchuk, and Andrey Fedyanin. Phase matching with Tamm plasmons for enhanced second- and third-harmonic generation. *Phys. Rev. B*, 97:115438, 03 2018.

[23] Shailja Sharma, Abhishek Mondal, and Ritwick Das. Infrared rainbow trapping via optical Tamm modes in an one-dimensional dielectric chirped photonic crystals. *Opt. Lett.*, 46(18):4566–4569, Sep 2021.

[24] B. J. Lee, C. J. Fu, and Z. M. Zhang. Coherent thermal emission from one-dimensional photonic crystals. *Applied Physics Letters*, 87(7):071904, 2005.

[25] S. Hadi Badri, M. M. Gilarlue, Saeid Gholami Farkoush, and Sang-Bong Rhee. Reconfigurable bandpass optical filters based on subwavelength grating waveguides with a ge2sb2 te5 cavity. *J. Opt. Soc. Am. B*, 38(4):1283–1289, Apr 2021.

[26] C. M. Fabre, P. Cheiney, G. L. Gattobigio, F. Vermersch, S. Faure, R. Mathevet, T. Lahaye, and D. Guéry-Odelin. Realization of a distributed bragg reflector for propagating guided matter waves. *Phys. Rev. Lett.*, 107:230401, Nov 2011.

[27] Aviv Karnieli, Sivan Trajtenberg-Mills, Giuseppe Di Domenico, and Ady Arie. Experimental observation of the geometric phase in nonlinear frequency conversion. *Optica*, 6(11):1401–1405, Nov 2019.

Chapter 6

Exceptional points in 1D-photonic crystal

6.1 Introduction

The optical systems obeying non-Hermitian dynamics have been the subject of intense and concerted investigation over the last two decades owing to their broad implications in photonics, acoustics, electronics as well as atomic physics. Optical systems which are governed by non-Hermitian Hamiltonian dynamics through an engineered gain and dissipation mechanism, provide a route to overcome the limitations imposed by closed optical systems that obey the Hermitian-Hamiltonian led dynamics. The eigenvalues of the Hamiltonian for the Hermitian system are real, while they are generally complex for non-hermitian systems. However, when the Hamiltonian in optical systems commutes with the parity-time ($\mathcal{PT}$) operator, then the non-Hermitian systems give rise to a real eigenvalue spectrum. A continuous change in the parameter governing the Hermiticity (of the Hamiltonian) breaks the $\mathcal{PT}$ symmetry which manifests in the form of complex eigenvalues for the system. In the phase space, such points where the real and complex eigenvalues coalesce are termed exceptional points (EPs) also known as "branch point singularities" [1, 2]. Interestingly not only eigenvalues but also their corresponding eigenvectors of a system's Hamiltonian coalesce simultaneously at EP. This spontaneous $\mathcal{PT}$-symmetry breaking has catalyzed a plethora of non-intuitive outcomes such as directional invisibility [3, 4], coherent perfect lasing and absorption [5, 6, 7, 8, 9], negative refraction [10], single-particle based sensing [11, 12, 13], distortion-free wireless optical power transfer [14] and a few more [15, 16, 17, 18, 19]. It is, however, worth noting that the incommensurate gain and loss distribution in non-Hermitian

systems imposes the primary limitation on the practical applications due to unpredictable signal-to-noise ratio near EP [20, 21, 22, 23]. In order to circumvent such bottlenecks, a few possibilities have been explored. One such promising route is to create an asymmetric loss in the system (without gain) whose dynamics could be explored using a non-Hermitian Hamiltonian with a uniform background loss [20, 24, 25]. Such configurations would exhibit $\mathcal{PT}$-symmetry which could be broken through scaling up the loss asymmetry. In a different scheme, a pseudo-Hermitian system was explored which allowed strong coupling between a large number of modes via manipulation of the parameters governing the Hamiltonian [24]. This led to the existence of EPs of multiple order and the interaction of eigenvalues around each EP provides a robust control on the propagation dynamics [26, 27, 28]. In spite of the aforementioned developments, a useful and practical proposition would be to devise a configuration hosting a multitude of EPs with the constraint that the electromagnetic *em* energy lost due to the non-Hermitian dynamics is stored in a reservoir. This essentially implies that the dissipative channel associated with a non-Hermitian system drives a separate Hermitian system which could allow reverse flow of *em* energy by virtue of cyclical dynamics. Such systems have been explored in the area of parametric frequency conversion processes where the *em* energy lost in one of the parametric processes (obeying non-Hermitian dynamics) is coherently added to the other parametric process that follows a Hermitian dynamics [29].

A plausible translation of such an idea in the non-absorptive linear systems would be to introduce a *virtual* loss in an intermodal interaction process thereby generating multiple EPs in the parameter space. One of the simplest configurations imitating such a process is a multimodal interaction in an all-dielectric 1D PC with a gradually varying duty cycle (for each unit cell). In such a 1D PC, the forward (source) to backward (sink) mode-coupling dynamics is essentially governed by a pseudo-Hermitian Hamiltonian whose Hermiticity is determined by the change in duty cycle along the propagation direction. In this chapter,

we show the existence of multiple EPs in a CPC and develop an analytical framework for ascertaining the possibility of exciting topologically-protected optical edge modes in such aperiodically stratified configurations.

6.2 Theoretical framework

As we have discussed earlier in Chapter 3 that for a 1D PC comprised of periodic bilayers with refractive indices n_1 and n_2 with thicknesses d_1 and d_2 the equivalent Schrödinger equation derived from the coupled-wave equation is written as

$$i\frac{d}{dz}\begin{pmatrix} \tilde{a}_i \\ \tilde{a}_r \end{pmatrix} = \begin{pmatrix} -\Delta k & -\kappa^* \\ \kappa & \Delta k \end{pmatrix}\begin{pmatrix} \tilde{a}_i \\ \tilde{a}_r \end{pmatrix} \tag{6.1}$$

and

$$\hat{H} = \begin{pmatrix} -\Delta k & -\kappa^* \\ \kappa & \Delta k \end{pmatrix} \tag{6.2}$$

Here, $\kappa^* = -\kappa$ and $\Delta k \ (= \frac{\Delta\beta}{2})$ which remains constant (for a given frequency) across the 1D-PC which has a fixed duty cycle. The autonomous Hamiltonian $\hat{H} = -\vec{\sigma}\cdot\vec{B}$ with $\vec{\sigma} \equiv [\sigma_x, \sigma_y, \sigma_z]$ are the Pauli's spin matrices and $\vec{B} \equiv [0, Im(\kappa), \Delta k]$ represents a pseudo-Hermitian evolution dynamics. In order to appreciate this point, the eigenvalues of $\hat{H}$ are given by

$$\begin{aligned} e_1 &= \sqrt{\Delta k^2 - \tilde{\kappa}^2} \\ e_2 &= -\sqrt{\Delta k^2 - \tilde{\kappa}^2} \end{aligned} \tag{6.3}$$

whereas the corresponding eigenfunctions are given as

$$\begin{aligned} |\psi_1\rangle &= \begin{pmatrix} -i\frac{(\Delta k + \sqrt{\Delta k^2 - \tilde{\kappa}^2})}{\tilde{\kappa}} \\ 1 \end{pmatrix} \\ |\psi_2\rangle &= \begin{pmatrix} +i\frac{(-\Delta k + \sqrt{\Delta k^2 - \tilde{\kappa}^2})}{\tilde{\kappa}} \\ 1 \end{pmatrix} \end{aligned} \tag{6.4}$$

Here, $\tilde{\kappa} = i\kappa$. It is apparent that $\Delta k > \tilde{\kappa}$ (modes in the pass bands) have real eigenvalues and hence, the forward-to-backscattered mode-coupling is cyclic (with respect to

z). On the other hand, $\Delta k < \tilde{\kappa}$ defines a spectrum where the forward-to-backscattered mode-coupling is unidirectional. In other words, the Hamiltonian $\hat{H}$ commutes with the parity-time ($\mathcal{PT}$) operator for $\Delta k > \tilde{\kappa}$, and therefore, it is termed as $\mathcal{PT}$-symmetric with respect to the forward-to-backscattered mode-coupling process. Here, the parity operator is defined as $\mathcal{P} \equiv \begin{pmatrix} 0 & 1 \\ 1 & 0 \end{pmatrix}$ and $\mathcal{T}$ is an anti-linear operator that performs the complex conjugation operation. For $\Delta k < \tilde{\kappa}$, the Hamiltonian $\hat{H}$ does not commute with $\mathcal{PT}$ operator, and consequently, the propagation characteristics pertain to $\mathcal{PT}$-symmetric broken phase. A closer look into the eigenvectors reveals that the equality $\tilde{\kappa} = \pm \Delta k$ manifests as coalescing of eigenvectors accompanied by vanishing eigenvalues. Such points in parameter space where $\tilde{\kappa}$ equals $\pm \Delta k$ are termed as the exceptional points (EPs) and they distinctly demarcate the regions exhibiting Hermitian ($\mathcal{PT}$-symmetric phase) and non-Hermitian ($\mathcal{PT}$-broken phase) dynamical evolution of states. In order to appreciate the idea mentioned
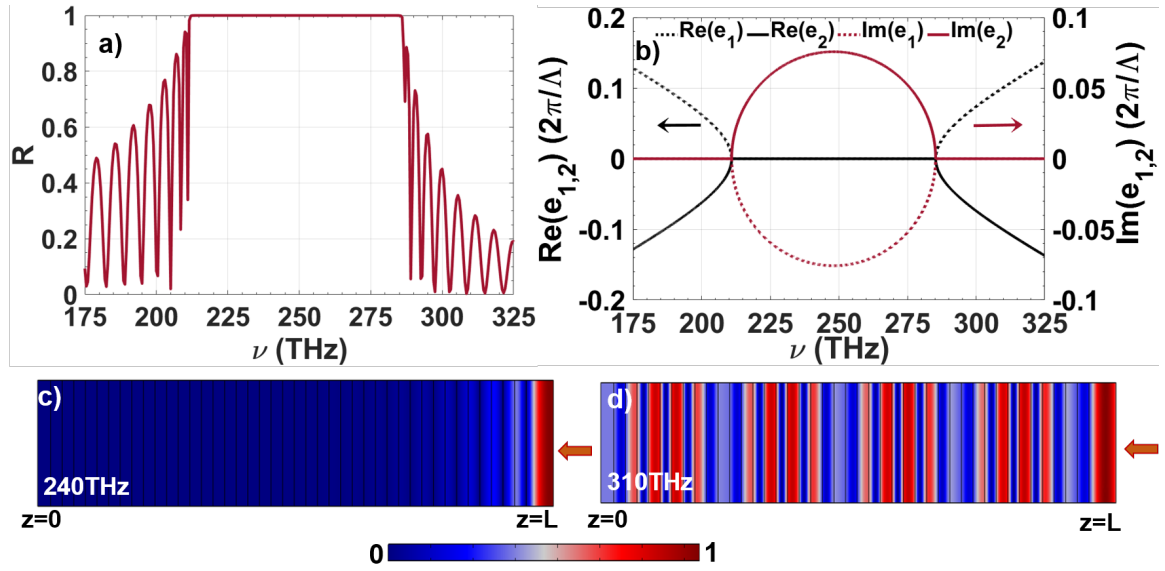
Figure 6.1: a) Shows the reflection spectrum of the normal 1D-PC. b) Shows the real part (black line) and imaginary part (maroon line) of eigenvalues e_1 (dotted lines) and e_2 (solid lines) as a function of frequency. c) and d) Shows the electric field intensity for frequencies lying within the PBG (240 THz) and outside the PBG (310 THz) respectively.

above, we consider a practical 1D PC with $n_1 \equiv TiO_2$ layer and $n_2 \equiv SiO_2$ layer.

The layer thicknesses are $d_1 = d_2 = 150\,nm$. The reflection spectrum for $N = 20$ unit cells is plotted in Fig. 6.1(a) which exhibits a high reflection band (or PBG) spreading over a $75\,THz$ bandwidth. In order to obtain the reflection spectrum, finite element method (FEM) based simulations were carried out using the commercially available computational tool (COMSOL Multiphysics). In the simulations, the periodic boundary condition is imposed along the transverse direction, and a mesh size of $5\,nm$ is considered. We ignore the material dispersion for the simulations and assume $n_1 = 2.5\,(\equiv TiO_2)$ and $n_2 = 1.5$ $(\equiv SiO_2)$ across the entire spectrum. For this 1D PC, we also plotted the eigenvalues e_1 and e_2 (see Fig. 6.1(b)) as a function of the frequency of the incident electromagnetic wave. It is apparent that the eigenvalues vanish at $\nu_1 \approx 210\,THz$ and $\nu_2 \approx 285\,THz$. These two frequencies (ν_1 and ν_2) define the EPs ($\kappa = +\Delta k$ and $\kappa = -\Delta k$) for the periodic 1D PC. A closer look would also reveal that the eigenvalues are purely imaginary within the PBG and the band edges (Fig. 6.1 (a)) coincide with ν_1 and ν_2. The mode fields for frequencies lying inside the PBG ($240\,THz$) and outside the PBG ($310\,THz$) are presented in Figs. 6.1(c) and (d) respectively. Figure 6.1(c) represents strong reflection from unit cells close to the entry face ($z = 0$) of the unit cell whereas Fig. 6.1(d) represents high delocalization of mode-field in the 1D-PC. In order to provide an analytical insight, we note that the extent of decay of mode-field for frequencies (ν) within the PBG is governed by the Bloch-wavevector (K) [30]. The couple-mode formalism connects to the Bloch wavevector through the relation $K = \frac{2\pi}{\Lambda} + e_{1,2}$ which is complex within the PBG and purely real in the transmission bands [30, 31]. In other words, Δk is much smaller than κ within the PBG, and for $\nu = 240\,THz$, $\Delta k \approx 0$. Therefore, solely κ determines the value of $e_{1,2}$ and in that case, the imaginary component of K maximizes. This essentially manifests through a rapid decay of mode-field for $\nu = 240\,THz$ along z (propagation direction).

It is worth noting that the investigations on systems exhibiting $\mathcal{PT}$-symmetry (or $\mathcal{PT}$-broken symmetry) led dynamics in photonics essentially involve optimally balanced gain-

91

loss architectures such as segmented waveguides and photonic crystals. In such systems, a complex relative permittivity in different sections depicting *actual* gain or loss for the propagating light beam gives rise to the $\mathcal{PT}$-symmetry (or $\mathcal{PT}$-broken symmetry). The present configuration involving 1D PC does not include an *actual* dissipative component for achieving the $\mathcal{PT}$-symmetric to $\mathcal{PT}$-symmetry broken phase transition. Alternatively, the coupling of optical power to the reflected mode $|r\rangle$ is analogous to a *virtual* loss for a forward propagating or incident $|i\rangle$ mode. When this coupling is relatively weak *i.e.* $\Delta k > \tilde{\kappa}$, $|i\rangle$ and $|r\rangle$ exhibits cyclic exchange of optical power (as a function of z) which is a primitive outcome for a $\mathcal{PT}$-symmetric dynamics. On the other hand, a strong coupling regime where $\Delta k < \tilde{\kappa}$ manifests through a monotonic growth of reflected mode ($|r\rangle$) that is a signature of $\mathcal{PT}$-symmetry broken phase. It is worthwhile to reiterate the point that the two regimes depicted by the inequality of Δk and $\tilde{\kappa}$ (in the parameter space) could be mapped onto the PBG and passband (s) in the reflected spectrum. Subsequently, each PBG is necessarily bounded by two EPs in this framework. Additionally, these two EPs are fixed and could not be tailored for a given 1D PC with a fixed duty cycle and fixed period. Also, the conventional 1D PC geometry excludes the possibility of realizing higher-order exceptional points [28]. Taking a clue from this critical viewpoint, we note that a gradual change in dielectric filling fraction ($\zeta = \frac{d_{1M}}{\Lambda}$) of each unit cell of the 1D PC would allow us to realize discretely spaced (multiple) EPs at different optical frequencies (or wavelengths). In order to elucidate this point, we recall that Δk, as well as $\tilde{\kappa}$, is a function of ζ. An optimum spatial variation in ζ could essentially give rise to the possibility of EPs at different physical locations (along z) in a 1D-PC. As an example, we show below that an optimally chirped photonic crystal (CPC) that satisfies the adiabatic constraints enables us to observe EPs at discreetly separated points along z.

6.3 Exceptional points in 1D-chirped photonic crystal

We consider a CPC configuration as described in *section3.4.1* that exhibits varying dielectric filling fraction (ζ) in each unit cell. This CPC could be visualized through a longitudinal variation in Δk as well as $\tilde{\kappa}$ by virtue of a monotonic change in average refractive index ($\bar{n}$) for an *unit cell*. This variation in Δk and $\tilde{\kappa}$ in a CPC geometry leads to an adiabatic evolution of the Stokes vector along the propagation direction and manifests through a broader PBG ($\approx 140\ THz$) in comparison with a conventional (periodic) 1D PC [31]. This is presented in Fig. 6.2(a) which shows a broader reflection spectrum for the CPC in comparison with the conventional 1D PC (Fig.6.1(a)). In addition, a flat transmission band and the absence of sharp transmission resonances are distinct features of CPC. The mode-propagation characteristics for the frequencies within the PBG (of CPC) are explored by drawing a comparison with the mode-field distributions for the equivalent modes within the PBG of a conventional 1D PC. Figures 6.2(b) and (c) show the mode-field distribution for two frequencies $\nu_a = 250\ THz$ and $\nu_b = 300\ THz$ which are within the PBG of CPC. In comparison with the mode-field distribution shown in Fig. 6.1(c), it could be observed that different modes are reflected from spatially separated z values. The smaller frequency ($\nu_a = 250\ THz$) is reflected from the regions which are closer to $z = 0$ edge of the CPC in comparison to that for $\nu_b = 300\ THz$. From an analytical viewpoint, it is worthwhile to recall that the Bloch-wavevector is expressed as $K = \frac{2\pi}{\Lambda} + e_{1,2}$. It is complex when $\Delta k < \kappa$ happens for all the frequencies within the PBG for a conventional 1D-PC. The imaginary component of K maximizes when $\Delta k = 0$ and accordingly, the mode-field decays sharply within one or two unit cells which could be seen in Fig. 6.1(c). Since, $\Delta k \equiv \Delta k(z)$ for 1D-APC, Δk vanishes in different unit cells (d_{1M}) for different frequencies (ν). Therefore, in the case of 1D-APC, the mode-field at different frequencies (within the PBG) strongly decays in different unit cells which is apparent in Fig. 6.2(b) and (c) This variation is indica-
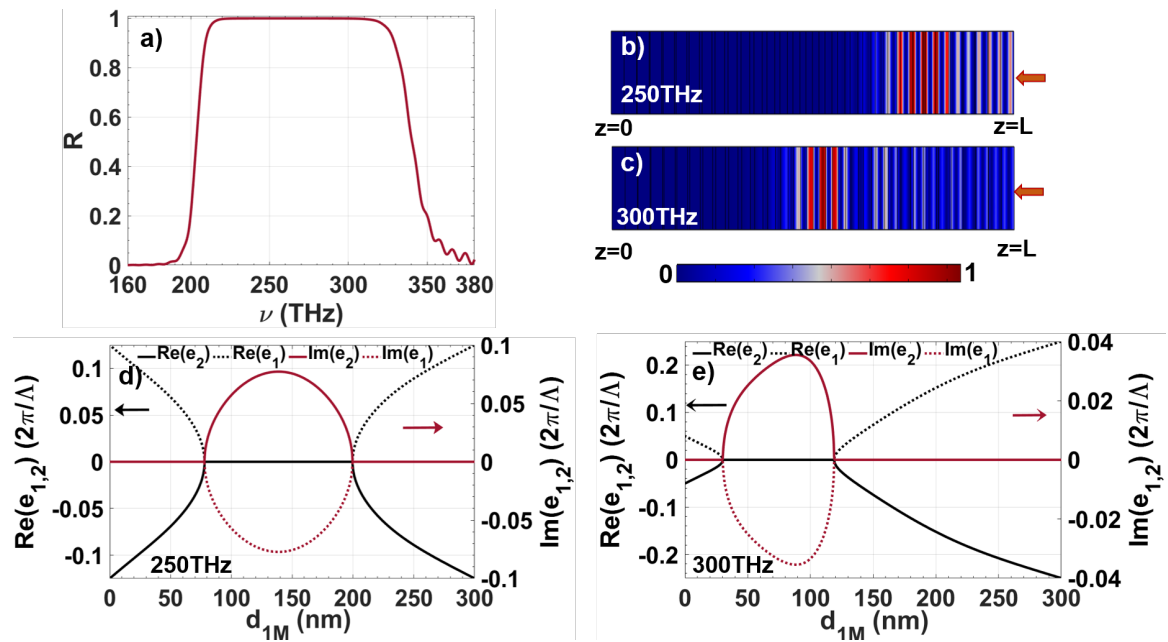
Figure 6.2: a) Shows the reflection spectrum for CPC ($\Lambda = 300nm$). b) and c) Shows the electric field intensity for two different frequencies lying within the PBG. d) and e) Shows the real part (black line) and imaginary part (maroon line) of eigenvalues e_1 (dotted lines) and e_2 (solid lines) as a function of d_{1M} for frequencies lying inside the PBG *i.e.* 250 THz and 300 THz respectively.

tive of the fact that the field is localized and exhibits instantaneous localization in different CPC sections.

From a different perspective, it is apparent that the variation in dielectric filling fraction (ζ) would result in different eigenvalues (and corresponding eigenvectors) for each unit cell. Accordingly, we plot the eigenvalues e_1 and e_2 as a function of d_{1M} for two frequencies $\nu_a = 250\ THz$ (Fig. 6.2(d)) and $\nu_b = 300\ THz$ (Fig. 6.2(e)) which are within the PBG of CPC. Each one of the figures shows that the eigenvalues (e_1 and e_2) vanish at two different values of d_{1M} *i.e.* at the location of two different unit cells. Therefore, the CPC geometry hosts two EPs for every d_{1M}. Consequently, for a multitude of ζ, there would be multiple EPs in the CPC for a forward-propagating mode to a backscattered mode-coupling process. As discussed before, the regions where $\Re e_1$ and $\Re e_2$ are non-zero in Figs. 6.2(d) and 6.2(e) exhibit a $\mathcal{PT}$-symmetric coupling dynamics between the forward-propagating and backscattered modes. On the other hand, in the regions where e_1 and e_2 are purely imaginary, the mode-coupling process exhibits $\mathcal{PT}$-symmetry broken manifolds. The illustrations presented in Figs. 6.2(d) and 6.2(e) show that for each frequency within the PBG, the CPC hosts two EPs at two different d_{1M}. Therefore, for each unit cell of the CPC, there exists one or more EPs, and consequently, CPC hosts multiple EPs. All such EPs are characterized by coalescing eigenvalues at different operating frequencies within the PBG of CPCs.

6.4   Conclusions

We show that an all-dielectric lossless 1D-photonic crystal exhibit a non-Hermitian dynamics and hosts at least two EPs in its eigenvalue spectrum. This method of realizing an interaction process obeying non-Hermitian dynamics is very different with respect to conventional methods such as the balanced loss-gain architectures which are essentially

a consequence of relative complex permittivity in different sections of the geometry. The present configuration *i.e.* all-dielectric 1D-photonic crystal does not include any dissipative component for achieving the $\mathcal{PT}$-symmetry to $\mathcal{PT}$-symmetry broken phase transition. This provides a basis for developing systems which involve virtual loss induced $\mathcal{PT}$-symmetric phase-transitions and therefore, carry out a wide-variety of optical manipulations without inducing a *real* loss or dissipation in the system.

References

[1] M.V. Berry. Physics of nonhermitian degeneracies. *Czechoslovak Journal of Physics*, 54:1039–1047, 01 2004.

[2] W D Heiss. The physics of exceptional points. *Journal of Physics A: Mathematical and Theoretical*, 45(44):444016, oct 2012.

[3] Xue-Feng Zhu, Yu-Gui Peng, and De-Gang Zhao. Anisotropic reflection oscillation in periodic multilayer structures of parity-time symmetry. *Opt. Express*, 22(15):18401–18411, Jul 2014.

[4] Zin Lin, Hamidreza Ramezani, Toni Eichelkraut, Tsampikos Kottos, Hui Cao, and Demetrios N. Christodoulides. Unidirectional invisibility induced by $\mathcal{PT}$-symmetric periodic structures. *Phys. Rev. Lett.*, 106:213901, May 2011.

[5] Wenjie Wan, Yidong Chong, Li Ge, Heeso Noh, A.Douglas Stone, and Hui Cao. Time-reversed lasing and interferometric control of absorption. *Science (New York, N.Y.)*, 331:889–92, 02 2011.

[6] Y. D. Chong, Li Ge, Hui Cao, and A. D. Stone. Coherent perfect absorbers: Time-reversed lasers. *Phys. Rev. Lett.*, 105:053901, Jul 2010.

[7] Stefano Longhi. $\mathcal{PT}$-symmetric laser absorber. *Phys. Rev. A*, 82:031801, Sep 2010.

[8] Y. D. Chong, Li Ge, and A. Douglas Stone. $\mathcal{PT}$-symmetry breaking and laser-absorber modes in optical scattering systems. *Phys. Rev. Lett.*, 106:093902, Mar 2011.

[9] Yong Sun, Wei Tan, Hong-qiang Li, Jensen Li, and Hong Chen. Experimental demonstration of a coherent perfect absorber with pt phase transition. *Phys. Rev. Lett.*, 112:143903, Apr 2014.

[10] Romain Fleury, Dimitrios L. Sounas, and Andrea Alù. Negative refraction and planar focusing based on parity-time symmetric metasurfaces. *Phys. Rev. Lett.*, 113:023903, Jul 2014.

[11] Jan Wiersig. Sensors operating at exceptional points: General theory. *Phys. Rev. A*, 93:033809, Mar 2016.

[12] Weijian Chen, Sahin Ozdemir, Guangming Zhao, Jan Wiersig, and Lan Yang. Exceptional points enhance sensing in an optical microcavity. *Nature*, 548:192–196, 08 2017.

[13] Jan Wiersig. Enhancing the sensitivity of frequency and energy splitting detection by using exceptional points: Application to microcavity sensors for single-particle detection. *Phys. Rev. Lett.*, 112:203901, May 2014.

[14] H. Xu, David Mason, Luyao Jiang, and Jack Harris. Topological energy transfer in an optomechanical system with exceptional points. *Nature*, 537, 02 2016.

[15] Li Ge, Y. D. Chong, and A. D. Stone. Conservation relations and anisotropic transmission resonances in one-dimensional $\mathcal{PT}$-symmetric photonic heterostructures. *Phys. Rev. A*, 85:023802, Feb 2012.

[16] Jörg Doppler, Alexei Mailybaev, Julian Böhm, Ulrich Kuhl, Adrian Girschik, Florian Libisch, Thomas Milburn, Peter Rabl, Nimrod Moiseyev, and Stefan Rotter. Dynamically encircling exceptional points in a waveguide: asymmetric mode switching from the breakdown of adiabaticity. *Nature*, 537, 02 2016.

[17] Yasutomo Ota, Ryota Katsumi, Katsuyuki Watanabe, Satoshi Iwamoto, and Yasuhiko Arakawa. Topological photonic crystal nanocavity laser. *Communications Physics*, 1, 11 2018.

[18] Li Ge and A. Douglas Stone. Parity-time symmetry breaking beyond one dimension: The role of degeneracy. *Phys. Rev. X*, 4:031011, Jul 2014.

[19] Xuefeng Zhu, Hamidreza Ramezani, Chengzhi Shi, Jie Zhu, and Xiang Zhang. $\mathcal{PT}$-symmetric acoustics. *Phys. Rev. X*, 4:031042, Sep 2014.

[20] Kun Ding, Z. Q. Zhang, and C. T. Chan. Coalescence of exceptional points and phase diagrams for one-dimensional $\mathcal{PT}$-symmetric photonic crystals. *Phys. Rev. B*, 92:235310, Dec 2015.

[21] Tamar Goldzak, Alexei A. Mailybaev, and Nimrod Moiseyev. Light stops at exceptional points. *Phys. Rev. Lett.*, 120:013901, Jan 2018.

[22] Jia-Rui Li, Lian-Lian Zhang, Wei-Bin Cui, and Wei-Jiang Gong. Topological properties in non-hermitian tetratomic su-schrieffer-heeger lattices. *Phys. Rev. Research*, 4:023009, Apr 2022.

[23] Fatemeh Mostafavi, Cem Yuce, Omar S. Maganã Loaiza, Henning Schomerus, and Hamidreza Ramezani. Robust localized zero-energy modes from locally embedded $\mathcal{PT}$-symmetric defects. *Phys. Rev. Research*, 2:032057, Sep 2020.

[24] A. Guo, G. J. Salamo, D. Duchesne, R. Morandotti, M. Volatier-Ravat, V. Aimez, G. A. Siviloglou, and D. N. Christodoulides. Observation of $\mathcal{PT}$-symmetry breaking in complex optical potentials. *Phys. Rev. Lett.*, 103:093902, Aug 2009.

[25] B Peng, SK Özdemir, S Rotter, H Yilmaz, M Liertzer, F Monifi, CM Bender, F Nori, and L Yang. Loss-induced suppression and revival of lasing. *Science (New York, N.Y.)*, 346(6207):328—332, October 2014.

[26] C. Dembowski, H.-D. Gräf, H. L. Harney, A. Heine, W. D. Heiss, H. Rehfeld, and A. Richter. Experimental observation of the topological structure of exceptional points. *Phys. Rev. Lett.*, 86:787–790, Jan 2001.

[27] Soo-Young Lee, Jung-Wan Ryu, Sang Wook Kim, and Yunchul Chung. Geometric phase around multiple exceptional points. *Phys. Rev. A*, 85:064103, Jun 2012.

[28] Arnab Laha, Dinesh Beniwal, Sibnath Dey, Abhijit Biswas, and Somnath Ghosh. Third-order exceptional point and successive switching among three states in an optical microcavity. *Phys. Rev. A*, 101:063829, Jun 2020.

[29] Noah Flemens and Jeffrey Moses. Hermitian nonlinear wave mixing controlled by a pt-symmetric phase transition. *Phys. Rev. Lett.*, 129:153901, Oct 2022.

[30] Amnon Yariv and Pochi Yeh. *Optical Waves in Crystals Propagation and Control of Laser Radiation*. New York Wiley, 1984.

[31] Shailja Sharma, Abhishek Mondal, and Ritwick Das. Infrared rainbow trapping via optical Tamm modes in an one-dimensional dielectric chirped photonic crystals. *Opt. Lett.*, 46(18):4566–4569, Sep 2021.

Chapter 7

Conclusion and future plans

7.1 Conclusions

We present an approach to understanding the propagation characteristics of electromagnetic waves or modes in a one-dimensional photonic crystal (1D-PC) using widely-known techniques adopted in a wide variety of systems that exhibit $SU(2)$ dynamical symmetry. We have drawn an analogy of population transfer dynamics of an atomic two-level system interacting with light to that for light propagation in classical "one-dimensional photonic crystal". We show that there exists a one-to-one correspondence between the coupled-wave equations of a 1D-PC with the time-dependent Schrodinger equation describing the evolution of an atomic $two-level$ system of spin-$\frac{1}{2}$ particles in a conventional source-driven magnetic field. The coupled-mode equations describing the forward and backward propagating modes in a 1D-PC are represented in the form of a single *optical Bloch equation* where the evolution of the state-vector depicts the dynamical evolution of incident and backscattered waves. This provides a platform to draw an analogy with a two-level atomic system and adopted a formalism for the adiabatic evolution of electromagnetic waves in the photonic crystal. In order to practically satisfy the conditions imposed by adiabatic constraints, a chirped photonic crystal (CPC) configuration has been investigated. The CPC exhibits a linearly varying duty cycle for each unit cell with identical periodicity for each unit cell. The CPC configuration exhibits substantial enhancement of PBG along with the varying degree of suppression of sharp transmission resonances in the reflection spectrum. The impact of alteration in the physical parameters of the PC is explored in detail. Interestingly, the CPC configuration involves a discernible longitudinal variation in the mode-coupling

coefficient in addition to the sweep in phase-mismatch that is described using the 'Allen-Eberly' scheme of adiabatic population transfer in two-level atomic systems. The CPC configuration could be employed for trapping a broad spectrum of light. When a plasmon-active metal is placed adjacent to the terminating layer of CPC, the backscattered phase undergoes multiple π phase jumps, which enables the excitation of multiple optical Tamm (OT)-like resonances. All the OT resonances are spatially separated in the CPC and their strong confinement manifests into group velocities as low as 0.17 times the velocity of light. These OT mode resonances provide a favorable platform for low-loss trapping of light with a lifetime of up to $\approx 3\,ps$. The light transmitted through a periodically-stratified medium or 1D-PC results in acquiring a 'quantized' geometric phase (0 or π) which is also known as the *Zak phase* or *topological phase*. This gives rise to the possibility of structuring optical beams over a broad spectral bandwidth via suitably designing the 1D-PC structure. We have explored a simple and flexible route to generate *Hermite-Gaussian* (HG_{01} or HG_{10}) beams by utilizing the light transmitted from conventional 1D PCs and provide a theoretical insight using finite-difference-time-domain (FDTD) based simulations. Lastly, we have also investigated that the Hamiltonian describing the counter-propagating modes in a PC is pseudo-Hermitian and dynamical evolution is characterized by the presence of exceptional points. We have explored the exceptional points present in the 1D photonic crystal system due to virtual loss and gain mechanisms. This knowledge was employed to ascertain with the origin of optical Tamm plasmon modes and the localization of field in the position of exceptional points.

7.2 Future plans

Novel PC designs extending into two-dimensions could further be explored which satisfy the adiabatic constraints. An interesting extension of this proposal would be to investigate

the evolution of the geometric phase in such PC configurations and the possibility to control the backscattered (reflection) phase through suitable PC designs. This promises to provide a unique and flexible platform for tailoring the spatial features of an optical beam using adiabatic PC configurations. Nevertheless, a natural extension of this proposal would be to explore the viability of this formalism in two- and three-dimensional photonic crystals with a focus on applications such as sensing and enhanced nonlinear optical interactions.